

UNIVERSITY OF SÃO PAULO
SÃO CARLOS SCHOOL OF ENGINEERING

MATHEUS VILAR MOTA SANTOS

**Analysis of delamination of composite laminates through the XFEM based
on the Layerwise displacement theory**

SÃO CARLOS
2018

MATHEUS VILAR MOTA SANTOS

**Análise de delaminação em compósitos laminados pelo método XFEM
baseado no campo de deslocamento da teoria Layerwise**

Versão original

Dissertação apresentada à Escola de Engenharia de São Carlos da Universidade de São Paulo, como requisito parcial para a obtenção do título de Mestre em Engenharia Mecânica

Área de concentração: Aeronaves

Orientador: Prof. Dr. Marcelo Leite Ribeiro

**SÃO CARLOS
2018**

AUTORIZO A REPRODUÇÃO TOTAL OU PARCIAL DESTA TRABALHO,
POR QUALQUER MEIO CONVENCIONAL OU ELETRÔNICO, PARA FINS
DE ESTUDO E PESQUISA, DESDE QUE CITADA A FONTE.

Ficha catalográfica elaborada pela Biblioteca Prof. Dr. Sérgio Rodrigues Fontes da
EESC/USP com os dados inseridos pelo(a) autor(a).

V697a Vilar, Matheus
Analysis of delamination of composite laminates
through the XFEM based on layer-wise displacement
theory / Matheus Vilar; orientador Marcelo Leite
Ribeiro. São Carlos, 2018.

Dissertação (Mestrado) - Programa de Pós-Graduação
em Engenharia Mecânica e Área de Concentração em
Aeronaves -- Escola de Engenharia de São Carlos da
Universidade de São Paulo, 2018.

1. XLFEM. 2. XFEM. 3. Exetended Finite Element
Method. 4. layer-wise. 5. composite laminate. 6.
composite structure. 7. progressive failure. 8.
delamination. I. Título.

Eduardo Graziosi Silva - CRB - 8/8907

SÃO CARLOS
2018

Ata de defesa pública de Dissertação do(a) Senhor(a) Matheus Vilar Mota Santos no Programa: Engenharia Mecânica, do(a) Escola de Engenharia de São Carlos da Universidade de São Paulo.

Aos 18 dias do mês de junho de 2018, no(a) Dependências do SEM realizou-se a Defesa da Dissertação do(a) Senhor(a) Matheus Vilar Mota Santos, apresentada para a obtenção do título de Mestre intitulada:

"Análise de delaminação em compósitos laminados pelo método XFEM baseado no campo de deslocamento da teoria Layer-wise"

Após declarada aberta a sessão, o(a) Sr(a) Presidente passa a palavra ao candidato para exposição e a seguir aos examinadores para as devidas arguições que se desenvolvem nos termos regimentais. Em seguida, a Comissão Julgadora proclama o resultado:

Nome dos Participantes da Banca	Função	Sigla da CPG	Resultado
Marcelo Leite Ribeiro	Presidente	EESC - USP	<u>Aprovado</u>
Sergio Persival Baroncini Proenca	Titular	EESC - USP	<u>Aprovado</u>
Mariano André Arbelo	Titular	ITA - Externo	<u>Aprovado</u>

Resultado Final: Aprovado

Parecer da Comissão Julgadora *

Eu, Ana Paula Bueno , lavrei a presente ata, que assino juntamente com os(as) Senhores(as). São Carlos, aos 18 dias do mês de junho de 2018.

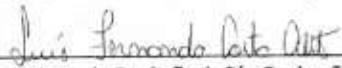

Sergio Persival Baroncini Proenca


Mariano André Arbelo


Marcelo Leite Ribeiro
Presidente da Comissão Julgadora

* Obs: Se o candidato for reprovado por algum dos membros, o preenchimento do parecer é obrigatório.

A defesa foi homologada pela Comissão de Pós-Graduação em 21.06.2018 e, portanto, o(a) aluno(a) faz jus ao título de Mestre em Ciências obtido no Programa Engenharia Mecânica - Área de concentração: Aeronaves.


Presidente da Comissão de Pós-Graduação

Prof. Titular Luis Fernando Costa Alberto
Presidente da CPG-EESC-USP

Confere com o original
SVPOSGR - EESC / USP

04.07.2018



ACKNOWLEDGMENT

Santos MVM. Xfem analysis for laminated composite plates with layerwise displacement theory [dissertation]. São Carlos: University of São Paulo, Department of Mechanical Engineering of São Carlos School of Engineering.

Composite laminates are being more employed as fundamental structures due to its low weight and high stiffness. An example of this innovation is the primary structures of modern aircraft, which are lighter than the material formerly used. To predict the material response as load gradually increases can be quite demanding due to composite's complex failure mechanism. Hence superior computational models should be further investigated to precisely predict the mechanical behavior of composite media. This dissertation addresses an extended finite element procedure based on the layerwise displacement theory to simulate purely mode I delamination failure in composite laminates. The present model has the potential to perform structural analyzes in a pre-delaminated structure and also considering progressive failure. The type of element to be employed at the discretion of the model is the rectangular 4-node iso-parametric homogeneous element whose displacement field is approximated based in the layerwise theory. There are four types of degrees of freedom, one displacement in each direction, and one degree of freedom associated to the strong discontinuity. Numerical examples already solved in the bibliography are suggested in this dissertation, which demonstrate the potential of the model developed to accurately simulate pure mode I delamination in case of the investigation here is further elaborated. In addition, one possibility of future development of this dissertation is the modeling of fracture mode I without the need to discretize the cohesive planes as realized in traditional Cohesive Zone Methods.

Keywords: XLFEM. XFEM. Extended finite element method. Layerwise. Composite laminate. Composite structure. Progressive failure, delamination.

Santos MVM. XFEM analysis for laminated composite plates with layerwise displacement theory [dissertação]. São Carlos: Universidade de São Paulo, Departamento de Engenharia Mecânica da Escola de Engenharia de São Carlos.

Compósitos laminados estão sendo mais empregados como estruturas fundamentais devido ao seu baixo peso e alta rigidez. Um exemplo dessa inovação são as estruturas primárias das aeronaves modernas, que são mais leves do que as os materiais empregados antigamente. Prever a resposta do material à medida que a carga aumenta gradualmente pode ser difícil devido ao complexo mecanismo de falha dos compósitos. Portanto, modelos computacionais mais refinados devem ser investigados a fim de se prever um comportamento mecânico mais preciso. Esta dissertação aborda um procedimento de elementos finitos estendido baseado na teoria de deslocamento layerwise para simular falhas de delaminação modo I em laminados compósitos. O modelo abordado tem potencial para realizar análises em uma estrutura pré-delaminada além de falha progressiva. O tipo de elemento a ser empregado na discretização do modelo é o isoparamétrico, homogêneo de 4 nós, retangular, e o campo de deslocamento é baseado na teoria layerwise. Existem quatro tipos de graus de liberdade, um deslocamento em cada direção, e um grau de liberdade associado à rotação. Sugere-se nesse trabalho, exemplos, que são comparados com a bibliografia, e que apontam que o modelo desenvolvido nesta dissertação tem o potencial de simular o fenômeno de delaminação em modo I com acurácia, caso o estudo nessa dissertação seja estendido. Além disso, uma possibilidade de desenvolvimento futuro desse trabalho é a modelagem da fratura modo I sem a necessidade de discretizar os planos coesivos entre as lâminas, como realizado em métodos coesivos tradicionais.

Palavras-chave: XLFEM. XFEM. Método dos elementos finitos estendido. Layerwise. Compósito laminado. Estrutura de compósito. Falha progressiva. Delaminação.

LIST OF FIGURES

Figure 1 - Phases of a composite material in micro scale	25
Figure 2 - Major monolithic CFRP and thermoplastic applications on Airbus 380's structure	26
Figure 3 - Sandwich laminate applications on A380's structure	27
Figure 4 - Possible modes of fracture: a) Mode I: tensile opening; b) mode II: in-plane shear; c) mode III: out-of-plane shear.....	28
Figure 5 - Conventional local system of coordinates in lamina level	32
Figure 6 - Typical longitudinal strain and stress in the thickness of a general composite laminate	34
Figure 7 - Out-of-plane shear stress according to Reissner-Mindlin theory and the Theory of Elasticity.....	36
Figure 8 - Cylindrical bending case solved by Pagano (1969).....	37
Figure 9 - Comparison of u from shear deformation theories for a $[0/90/0]$ laminate.....	38
Figure 10 - Comparison of τ_{xz} from shear deformation theories for a $[0/90/0]$ laminate	39
Figure 11 - Equilibrium of out-of-plane stresses between two adjacent layers.....	40
Figure 12 - Comparison of the interlaminar stress τ_{xz} according to CPT, Elasticity solution, and layerwise theory of Kam and Jam (1995).....	44
Figure 13 - Comparison of displacement distribution through the thickness of ESL theory and layerwise theory.....	45
Figure 14 - Linear layerwise functions and nodal displacements through the thickness in a three-layered composite plate.....	46
Figure 15 - Example of a layerwise quadratic interpolation through the thickness within a layer based in the Legendre polynomials	48
Figure 16 - Illustrative case of a two-layer 1D element with linear layerwise interpolation through the thickness.....	49
Figure 17 - Global linear system of the problem of Figure 16.....	50
Figure 18 - Categories of discontinuities on XFEM.....	52
Figure 19 - Techniques to model cracks in Finite Elements numerical solution: a) smeared crack; b) inter-element crack; c) XFEM enrichments.....	53
Figure 20 - Enriched nodes selected to enrich on a FEM mesh	55
Figure 21 - Heaviside function multiplied by the standard shape function of a two-node 1D element	56
Figure 22 - Shape functions with shifted effect.....	58
Figure 23 - a) Functions to model weak discontinuities; b) functions to model weak discontinuities times the standard shape function	59
Figure 24 - Interaction forces in function of the distance between the fracture surfaces.....	62
Figure 25 - Examples of triangular, exponential and trapezoidal traction-separation laws	63

LIST OF FIGURES

Figure 26 - Domain Ω crossed by a discontinuity at the boundary Γ_d	65
Figure 27 - Hyperbolic tangent function used to model strong discontinuity	67
Figure 28 - Differentiation of the hyperbolic tangent function, with zoom near $x=0$	68
Figure 29 - Orientation of the discontinuity	74
Figure 30 - Illustration of enriched elements in the formulation proposed	75
Figure 31 - The two methods proposed by Moës et al. (1999) to overcome the numerical integration spurious via Gauss quadrature on enriched elements	80
Figure 32 - Illustrative case of a two-layer beam under mode I via the formulation proposed	81
Figure 33 - Global linear system of the problem of Figure 32	82
Figure 34 - Boundary conditions and geometry of the first numerical example (dimensions in millimeters)	84
Figure 35 - Mesh discretization of the composite thin laminate numerical example with the seeds created in the thickness direction.....	85
Figure 36 - The deformed shape of $[0]_4$ laminate of the first numerical example: a) LW1 analysis; b) Solid analysis.	86
Figure 37 - The deformed shape of $[0/90]_2$ of the first numerical example of LW1 and SOLID analyses respectively	86
Figure 38 - Chosen path to compare stress distribution	88
Figure 39 - Distribution of stresses in XX direction of the first numerical example of $[0]_4$	89
Figure 40 - Distribution of stresses in YY direction of the first numerical example of $[0]_4$	89
Figure 41 - Distribution of stress in ZZ direction of the first numerical example of $[0]_4$	90
Figure 42 - Distribution of stresses in XX direction of the first numerical example of $[0/90]_2$	91
Figure 43 - Distribution of stresses in YY direction of the first numerical example of $[0/90]_2$	92
Figure 44 - Distribution of stress in ZZ direction of the first numerical example of $[0/90]_2$...	93
Figure 45 - Schematics of the deep beam numerical example	94
Figure 46 - Discretization of the cross-section of each LW analysis	95
Figure 47 - (a) Isometric view of the general geometry of the beam modeled in ABAQUS TM , with boundary conditions; (b) front view of the homogeneous model; (c) front view of the heterogeneous model.....	97
Figure 48 - a) normal strain in XX direction; b) normal stress in XX direction	98
Figure 49 - a) normal strain in YY direction; b) normal stress in YY direction	99
Figure 50 - a) normal strain in ZZ direction; b) normal stress in ZZ direction	100
Figure 51 - a) shear strain in xz direction; b) shear stress in xx direction.....	100
Figure 52 - Schematics of the composite sandwich numerical example.....	101

LIST OF FIGURES

Figure 53 - Path taken to compare stresses of the sandwich composite case.....	102
Figure 54 - Mesh discretization of the composite sandwich numerical example with the seeds created in the thickness direction	103
Figure 55 - Normal stress distribution in the XX direction of the sandwich composite case	104
Figure 56 - Absolute value of the relative residual of the layerwise analyses in relation to the solid-like analysis carried out in ABAQUS™ in XX direction	105
Figure 57 - Normal stress distribution in the YY direction of the sandwich composite case	106
Figure 58 - Absolute value of the relative residual of the layerwise analyses in relation to the solid-like analysis carried out in ABAQUS™ in YY direction	107
Figure 59 - Normal stress distribution in the ZZ direction of the sandwich composite case .	108
Figure 60 - Absolute value of the relative residual of the layerwise analyses in relation to the solid-like analysis carried out in ABAQUS™ in ZZ direction	109
Figure 61 - Convergence analysis based on the solution error in XX direction.....	110
Figure 62 - Convergence analysis based on the solution error in YY direction.....	111
Figure 63 - Convergence analysis based on the solution error in ZZ direction.....	112
Figure 64 - Boundary conditions and geometry of the fourth numerical example.....	113
Figure 65 - Traction separation law of the cohesive zone of the second numerical example	114
Figure 66 - Deformed shape with the gradient of displacement on longitudinal direction of [0/90/0/90] _s laminate: a) bibliography; b) method proposed.....	115
Figure 67 - Deformed shape with the gradient of displacement on thickness direction of [0/90/0/90] _s laminate: a) bibliography; b) method proposed.....	116
Figure 68 - Influence of the numerical parameter α in the displacement field	118

LIST OF ABBREVIATIONS

ABQ Het	Finite Element analysis based in 20-node hybrid solid elements (C3D20H)
ABQ Hom	Finite Element analysis based in 20-node solid element (C3D20)
C3D20	Finite element of ABAQUS TM (20-node brick element)
C3D20H	Finite element of ABAQUS TM (20-node brick hybrid element)
CFRP	Carbon Fibre Reinforced Plastic
CLT	Classical Laminate Theory
CZM	Cohesive Zone Method
ESL	Equivalent Single Layer
FEM	Finite Element Method
FSDT	First Order Shear Deformation Theory
HSDT	Higher-order Shear Deformation Theory
LW	Layerwise theory
LW1	Finite element analysis based on a linear layerwise interpolation
LW2	Finite element analysis based on a quadratic layerwise interpolation
LW3	Finite element analysis based on a cubic layerwise interpolation
LW4	Finite element analysis based on a fourth-order layerwise interpolation
SIF	Stress Intensity Factor
SOLID	Finite Element analysis based in 20-node solid element (C3D20)
XFEM	Extended Finite Element Method
14-layer LW1	Linear layerwise finite element analysis with 14 layers discretized
21-layer LW1	Linear layerwise finite element analysis with 21 layers discretized
28-layer LW1	Linear layerwise finite element analysis with 28 layers discretized

LIST OF SYMBOLS

a_j	Vector of nodal parameters of the j -th node
α	Numerical parameter of the hyperbolic tangent function
$b_h^{l_1}, b_h^{l_2}$	Degree of freedom of the XFEM related to each side of the crack tip
B_{pm}^{jk}	Matrix which relates nodal strain to nodal parameters (B matrix)
β	Numerical parameter of <i>The Power Law</i> criterion for delamination
C_{ij}	Constitutive Hooke's law for orthotropic materials (global system)
\bar{C}_{ij}	Constitutive Hooke's law for orthotropic materials (local system)
$\cos(x)$	Cosine function
γ_{ij}	Shear deformation in the ij direction
Γ	Physical boundary of the domain Ω
Γ_d	Internal boundary of the discontinuity (separates domain Ω in two parts)
Γ_u	Domain of the prescribed displacement \bar{u}
Γ_t	Domain of the prescribed external load \bar{t}
D_d	Damage parameters of the traction-separation law
dA	Differential of area
dz	Differential of the variable of z coordinate
$d\Omega$	Differentiation of the domain Ω
$d\Gamma_d$	Differentiation of the domain Γ_d
δ_{ij}	Kronecker delta
δ_n^0	Mode I critical displacement of the cohesive element

LIST OF SYMBOLS

δ_d	Relative displacement of the faces of the cohesive element
$\delta_{s_2}, \delta_{s_3}$	Mode II and III separation of the cohesive element
δ_n^Γ	Maximum separation of the cohesive element
$\delta\varepsilon_{ij}$	Virtual strain in ij direction
δu_i	Virtual displacement in i direction
$\delta\hat{u}$	Virtual displacement of the continuous displacement field
δu	Virtual displacement of the discontinuous displacement field
E	Set of nodes with general enrichments
E_{jj}	Young's modulus in the jj direction
ε_{ij}	Strain in ij direction
F_j	j -th component of the global force vector
$f_k(x)$	General function of k index
f_{Γ_d}	Enrich function associated to strong discontinuity on the boundary Γ_d
$F_l^{(1)}, F_l^{(2)}$	Enrichment functions corresponding to both sides of the discontinuity
$F_l^1(x), F_l^2(x)$	Enrichment function related to crack-tip enrichments
ζ	Through the thickness iso-parametric coordinate
G_{ij}	Shear modulus in the ij direction
G_I	Strain energy release rate associated to mode I
G_{IC}	Critical strain energy release rate associated to mode I

LIST OF SYMBOLS

G_{II}	Strain energy release rate associated to mode II
G_{IIC}	Critical strain energy release rate associated to mode II
$\nabla \hat{u}$	Gradient of the continuous displacement field
∇u	Gradient of the discontinuous displacement field
$H(x)$	Heaviside function in function
η	In plane iso-coordinate
$K_{ij}^{(k)(e)}$	i and j indexes of the Stiffness matrix of the k -th lamina of the element e
\tilde{K}_n^0	Stiffness of the cohesive element before degradation is triggered
\tilde{K}_F	Stiffness of the cohesive element at the tip of beam
\tilde{K}_i	Stiffness of the i -th cohesive element
ℓ	Length
L	Number of layerwise functions within a layer
L^*	Number of laminas of the laminate
λ_k	Extra degree of freedom associated with strong enrichment
M_i	Number of terms in expansion of the i -th component
μ_k	Additional degrees of freedom related to weak enrichment
N_j	In-plane finite element shape function of the j -th node
N_k^*	In-plane extended finite element shape function of the k -th enriched node
n_d	Unitarian vector normal to the boundary Γ_d
n_{S_2}, n_{S_3}	Unitarian vector in the plane of the boundary Γ_d

LIST OF SYMBOLS

n_t	Unitarian vector normal to the boundary Γ_t
N_N	Number of nodes in the element
ν_{ij}	Poisson's ratio in ij direction
∇	Nabla operator
ξ	In plane iso-coordinate
P	External load
$p(n)$	Fourier series
$P_s(\zeta_k)$	Legendre polynomial of order s
$q(x)$	Load in function of x
q_0	Constant load
ρ_k	General extra degree of freedom of the Extended Finite Element Method
S	Number of nodes with strong enrichments
$\text{Sech}(x)$	Hyperbolic secant function
$\sin(x)$	Sine function
σ_{ij}	Stress in ij direction
σ	Cauchy stress tensor
t	Time
t_d	Mode I traction force acting in the cohesive element
(T_1, T_2)	Set of nodes with crack tip enrichments
T_F	Number of crack tips

LIST OF SYMBOLS

\bar{t}	Prescribed traction
t_{s_2}, t_{s_3}	Mode II and III traction force acting in the cohesive element
$\text{Tanh}(x)$	Hyperbolic tangent function
τ_{ij}	Shear stress in the ij direction
$u_i(x, y, z)$	Displacement field in the i direction
u_i^{jk}	Standard FEM nodal displacement
\hat{u}_i^j	Function of the position in i -th direction
u, v, w	The three components of displacement of a point in the reference plane
U, V, W	Coordinate functions which vanish on the reference plane
u	Continuous displacement field
u	Discontinuous displacement field
\bar{u}	Prescribed displacement
\hat{U}_j	Nodal parameter in the global reference
$\phi_s(z)$	Layerwise function of s index in function of the thickness coordinate
$\Phi_j(z)$	Layerwise in-plane functions which vanish on the reference plane
$\chi(x)$	Enrichment function related to weak discontinuities
$\psi(x)$	Enrichment functions of the XFEM
$\Psi_j(z)$	Layerwise out-of-plane functions which vanish on the reference plane
W_E	Number of nodes with weak enrichments
z	Through the thickness coordinate in the Cartesian coordinate system

LIST OF SYMBOLS

Z_{bot}, Z_{top}	Bottom and top coordinates in the thickness direction of a specific lamina
Ω	Whole domain subject to the boundary conditions
Ω^+	Positive part of a given domain crossed by a discontinuity
Ω^-	Negative part of a given domain crossed by a discontinuity

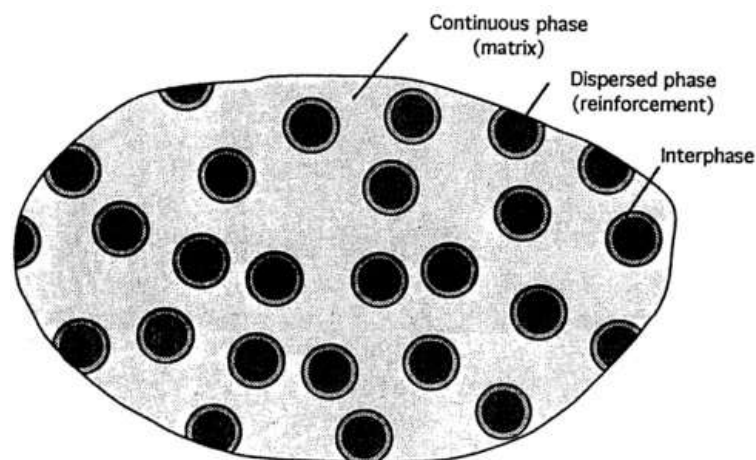
SUMMARY

1	INTRODUCTION, JUSTIFICATION, AND OBJECTIVES.....	25
1.1	Justification	30
1.2	Objectives.....	31
2	BIBLIOGRAPHIC REVIEW	32
2.1	Fiber reinforced laminate	32
2.2	Review of displacement theories.....	33
2.2.1	Equivalent Single Layer Theories	33
2.2.2	Layerwise Displacement Theory.....	39
2.3	Extended Finite Element Method.....	50
2.4	Cohesive Zone Model	61
3	GOVERNING EQUATION	65
3.1	Kinematic relation	65
3.2	Equilibrium equations	69
3.3	Constitutive relations.....	71
3.3.1	Constitutive law for orthotropic materials.....	71
3.3.2	The constitutive law of the cohesive zone.....	73
4	EXTENDED LAYERWISE FINITE ELEMENT FORMULATION	75
4.1	Discrete displacement field	76
4.2	Discrete strain field	77
5	NUMERICAL RESULTS.....	83
6	CONCLUSIONS AND FUTURE WORKS	119
7	REFERENCES.....	122

1 INTRODUCTION, JUSTIFICATION, AND OBJECTIVES

A composite structure is a heterogeneous material constituted of two or more phases whose performance is designed to be superior to those of the constituents acting separately. The stiffer phase, known as *reinforcement* or *fiber*, is discontinuous, while the soft phase is called *matrix* (also resin). In addition, chemical interactions cause a composite structure to have unique properties in the region between the reinforcement and the matrix; therefore, this zone is considered to be another phase named as *interphase*. The role of each constituent depends upon the type of application of the composite material. For low to medium performance, the fibers provide stiffening but only local strengthening, while the matrix is responsible for bearing loading. Conversely, high-performance composite structures behave differently; the matrix offers protection and support for the fibers while the reinforcement bears the load. The type of structure studied in this dissertation is the composite laminate, which is an assembly of multiple layers of fibrous composite materials forming a specific stacking sequence; each layer may have a different fiber orientation (Daniel; Ishai, 1994). Figure 1 is a representation of composite material on a micro scale.

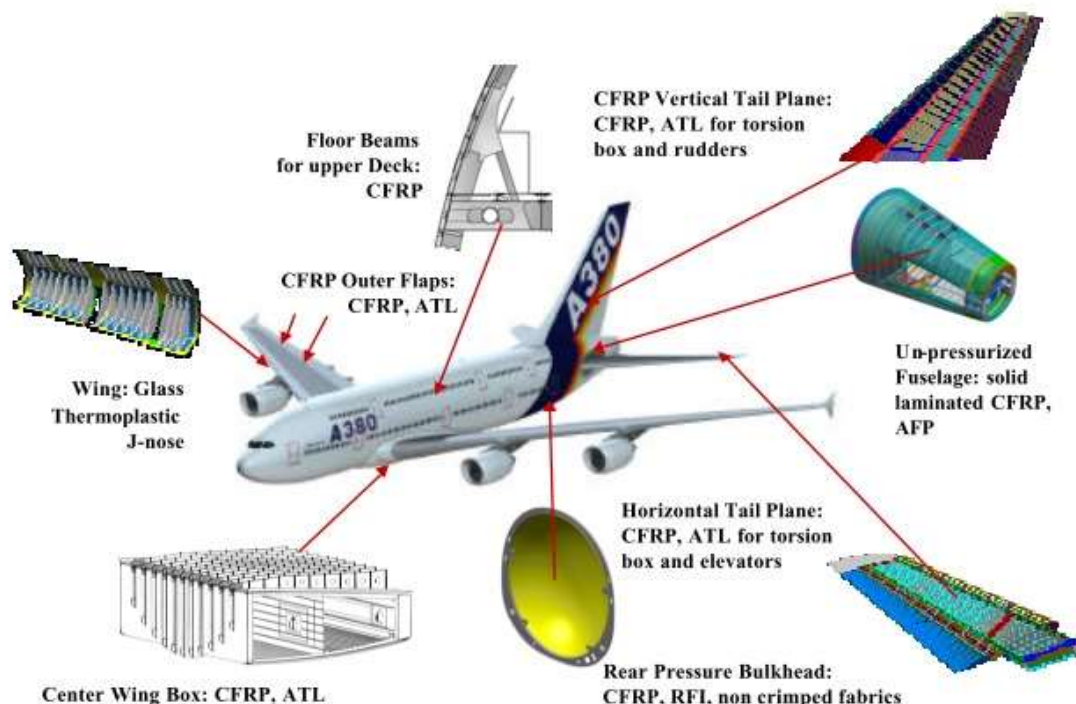
Figure 1 - Phases of a composite material in micro scale



Source: Daniel and Ishai (1994).

Fibrous composite materials are used since ancient times to fabricate multiple products, but it was only potentially explored by engineers since 1960s (Herakovich, 1967). Nowadays, composite laminates are employed as structures in submarines, sports equipment, medical tools, buildings, aerospace and astronavigation industry, automobiles, and several further applications (Zhang; Yang, 2009). A recent innovation was the employment of composite laminates as primary and secondary structures of the Airbus 380 and 350, and the Boeing 787. It is estimated that 40% of the Airbus 380's structure is made of composite materials., which resulted in a considerable reduction of the airplane weight and its maintainability (Pora, 2001). It is important to point out that such weight saving is always desirable to aircraft designing. Figure 2 represents some carbon fiber reinforced plastic (CFRP) and thermoplastic applications on Airbus 380's structure.

Figure 2 - Major monolithic CFRP and thermoplastic applications on Airbus 380's structure

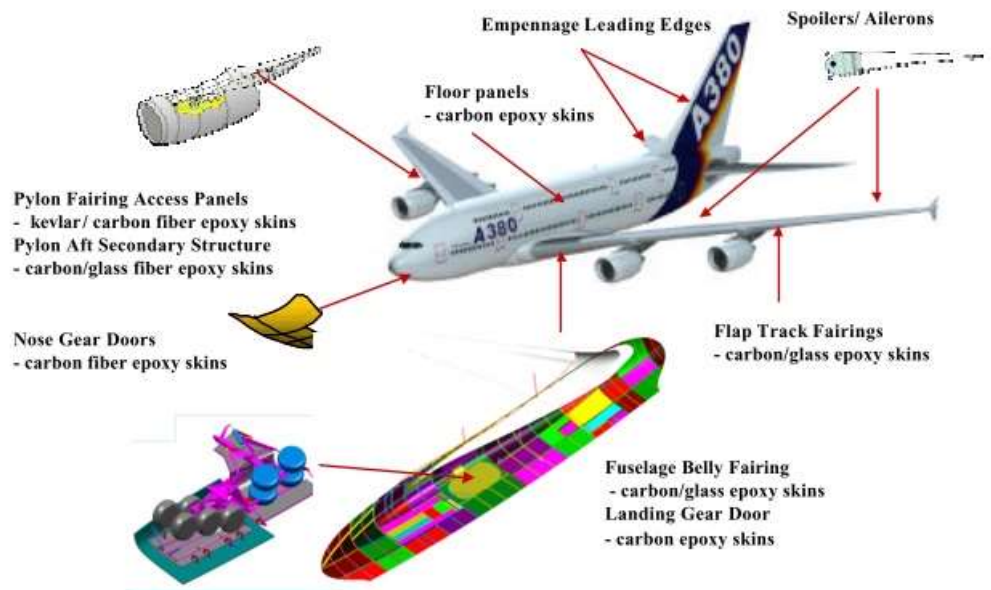


Source: Pora (2001).

In addition to CFRP and thermoplastic, sandwich laminates are also employed in the Airbus 380's structure. This type of composite structure consists of a light honeycomb or

corrugated metal core shrouded by two outer skins (Megson, 1999). Some applications of sandwich laminates in the Airbus 380's composition are displayed in Figure 3.

Figure 3 - Sandwich laminate applications on A380's structure



Source: Pora (2001).

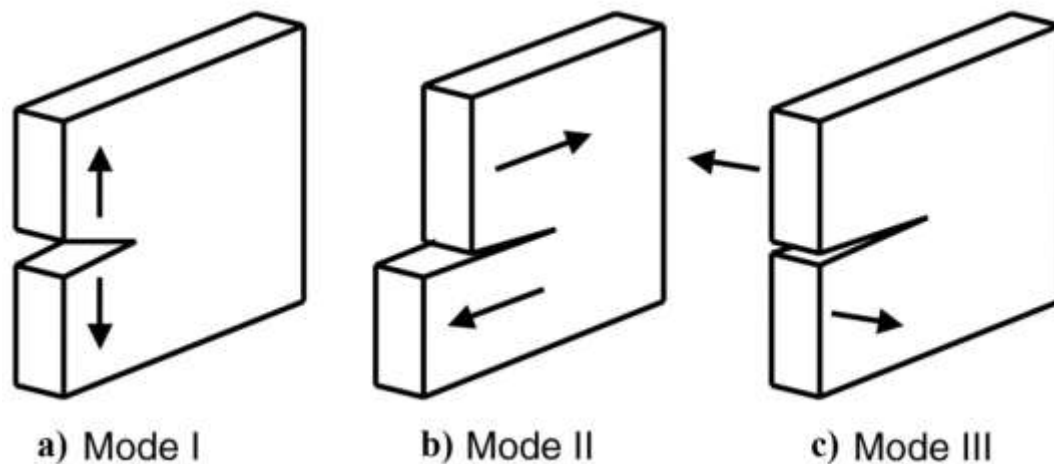
Although composite laminates have significant advantages, its use is still limited due to difficulty of predicting their service life. The failure mechanisms are complicated and hard to predict. Hence the safety factor considered to design composite structures is superior when compared to usual materials such as the aluminum alloy 2024 (Zhu, 1992). Furthermore, Zhu (1992) mentions that the safety factor applied to composite structures will only decrease when the failure mechanisms are more comprehended. Therefore, it is essential to study further the failures phenomena involved in composite laminates as well as developing more accurate models to account the complex mechanisms in composite media.

The failure in composite structures can be intra-ply or inter-ply. Intra-ply failures occur within a single ply; it can be a fiber rupture or compressive kinking, fiber/matrix debond, matrix cracks, and others flaws. The inter-ply failures, also known as delamination, are the detachment of two bonded plies (Traversa, 2006). Some damage evolution theories

such as Ribeiro et al. (2012) remark that, as load increases, intra-ply failures occur first and it gradually evolves to delamination.

Linear Elastic Fracture Mechanics (LEFM) classifies the fracture in three distinct groups: Tensile opening (mode I); in-plane shear or sliding (mode II); Out of plane shear or tearing (mode III). Figure 4 illustrates the types of fracture in solid media. The energy associated to these three kinds of fracture is named strain energy release rate and it is different to each mode. Thus, the energy necessary to open a crack in pure mode I is not the same of the energy of sliding or tearing. Generally, all modes are involved in a real structure.

Figure 4 - Possible modes of fracture: a) Mode I: tensile opening; b) mode II: in-plane shear; c) mode III: out-of-plane shear



Source: Author.

At the present time, there are basically four approaches to model delamination in composite media (Pascoe et al. 2013): Stresses/strain based methods; fracture mechanics; Cohesive Zone Method (CZM); and the Extended Finite Element Method (XFEM). The first two approaches relate the state of stress/strain and the energy release rate respectively, and the others are applied with the finite element procedure. Additionally to these four techniques, Barbero and Reddy (1990) proposed to model delamination via the layerwise theory (LW) developed by Reddy (1987).

CZMs are finite-element based models, where the interfaces between two adjacent laminas are discretized with unique elastic properties. In the CZM, a traction-separation law is

employed to prescribe the behavior of the constitutive relation of the cohesive zone, in which the stiffness suffers softening penalty as delamination progresses. The main advantages of the CZM approach are that it dismisses re-meshing along a pre-defined crack path (Belytschko; Black, 1999), and it can incorporate a pre-delaminated zone in the model (Muñoz et al. 2006). Conversely, some parameters need to be specified to define the cohesive zone properties, and the majority of them are chosen based on numerical considerations only (Pascoe et al., 2013). For instance, the initial stiffness in respect to delamination is not possible to measure, and it is chosen for plainly numerical reasons (Pascoe et al., 2013).

The XFEM is the newest approach to model discontinuity. The basic idea is to enrich the approximation of the displacement field of elements with discontinuities. The XFEM was first proposed by Belytschko and Black (1999) based on the conception of the partition of unity formulated by Babuška et al. (1997). Recent developments on composite media through XFEM have been discussed in Huynh et al. (2009). To improve convergence of XFEM, it is possible to include a cohesive law to govern the traction-separation behavior of the delamination (Moës; Belytschko, 2002). A drawback of all of XFEM formulations is the fact that they are usually based on the First Order Shear Deformation Theory (FSDT), which is not able to precisely determine the out of plane stresses between adjacent laminas of a laminate (Robbins; Reddy, 1993). Since inter-laminar stresses have an essential role in delamination, it is more reasonable to exploit more accurate displacement formulations to combine with XFEM. The layerwise displacement theory proposed by Reddy (1987) achieves better results than the FSDT for out of plane stresses. Furthermore, formulations based on layerwise displacement fields are free of shear and membrane locking and has superior computational effort when compared to a similar 3D elements in finite element analyzes (Reddy, 2004). Li et al. (2015) and Li (2016) developed formulations that employ XFEM and layerwise in beams and shell elements respectively.

This dissertation proposes a numerical approach potential able to model pure mode I delamination in composite laminates through the XFEM, based in a layerwise displacement field (XLFEM). To describe the behavior of the delaminated zone, a traction separation law is imposed. The main advantages of the present formulation are:

- a) the XFEM is flexible and efficient. It is an extension of the standard finite element procedures which can be easily adapted to delamination analyses;
- b) CZM is used only to model the stiffness of the delaminated zone. There is no need for discretizing any planes;
- c) the layerwise theory provides more realist displacements and stresses fields, which is more appropriate to identify potential failures.

There is no research that combines XFEM, CZM, and layerwise theory. It is introduced in this master's thesis a unique formulation, capable of accurately analyze delamination in composite laminates.

1.1 Justification

The majority of the delamination models available in the literature are based on Equivalent Single Layer Theories, which fail to describe local effects on composite laminates. Delamination problems require the accurate calculation of the 3D stress field throughout lamina interfaces. Hence, it is essential to approach such non-linearity with more refined formulations. The layerwise theory (LW) provides exceptional accuracy when dealing with composite laminates; its assumptions are closer to reality.

The investigations of Li et al. (2015) and Li (2016) approached delamination utilizing both XFEM and layerwise theory; their formulation are capable of modeling discontinuity in the displacement and strain fields in pre-delaminated composites, plus determining the stress intensity factor (SIF) near the tip of the pre-delaminated zone. Conversely, Li et al. (2015) and Li (2016) do not account progressive failure analyzes, and their models utilize considerable computational resources due to employing the XFEM to simulate delamination and to enforce the discontinuity over the strain field on every interface between laminas.

This master's thesis approaches delamination problems exploiting all benefits of the XFEM and layerwise theory, and it can possibly be extended to progressive failure analysis to further investigations. Additionally, the method suggested here demands less computational

resources due to the fact of using the layerwise theory and that the XFEM is only used to simulate delamination

This master's thesis includes the CZM to improve the numerical convergence. Cohesive Zone Models are widely employed to carry out delamination problems in progressive failure analyses. To approach delamination through the CZM, it is necessary to discretize each cohesive zone surfaces within the laminates. This procedure is dispensable here because CZM is automatically applied to any failed location throughout the domain, which can be useful to analyze multiple-layered laminates.

The motivation of this master's thesis is to develop a new model to perform progressive failure analyses accounting delamination based on the LW theory. Furthermore, the model should demand less computational resources when compared to similar formulations.

1.2 Objectives

The primary purpose of this research is to develop a numerical model potentially capable of simulating the delamination failure in composite laminates through the XFEM based in the layerwise displacement theory. The delamination is pure mode I and is modeled as strong discontinuity via XFEM, which is a leap in the displacement field. The Cohesive Zone Method is implemented to describe the behavior of the delaminated zone. Therefore, the primary objective is achieved by completing the following partial goals:

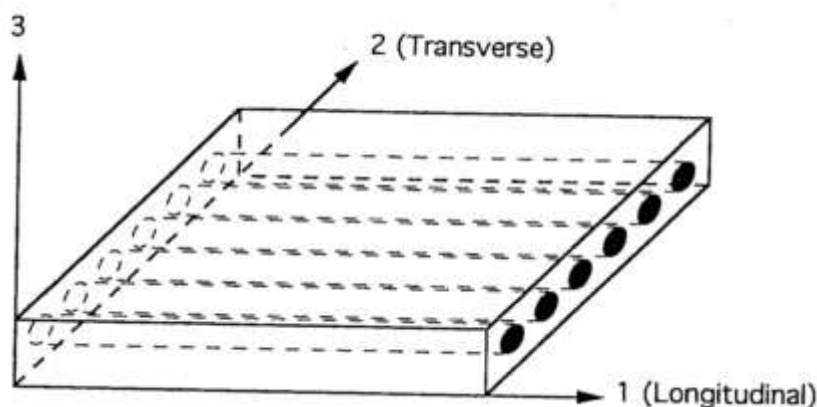
- a) study state of the art regarding XFEM, CZM, and the layerwise theory;
- b) implement the layerwise theory and numerically validate;
- c) employ the Extended Finite Element Method to model delamination for subsequent investigations;
- d) study alternative parameters to approach strong discontinuities, such as distinct functions to model discontinuity;
- e) investigate the Cohesive Zone Method to idealize the behavior of the delaminated area.

2 BIBLIOGRAPHIC REVIEW

2.1 Fiber reinforced laminate

A lamina is a plane, or curved layer, of reinforcements whose elastic properties are orthotropic. This means that the elastic properties differ along three mutually-orthogonal twofold axes of rotational symmetry. As a convention, the lamina axes are denominated as 1, 2, and 3. The first axis is parallel to the fibers; the second one is perpendicular to axis 1 and is projected on the lamina plane; the last axis is normal to the plane of the lamina (Daniel; Ishai, 1994). Figure 5 is an illustration of the conventional lamina axes.

Figure 5 - Conventional local system of coordinates in lamina level



Source: Daniel and Ishai (1994).

The laminate is the assembling of two or more laminas, stacked in a particular manner and bonded together. Each ply may have a specific thickness and a different fiber orientation. Therefore, it is convenient to analyze laminates using a conventional fixed system of coordinates (usually the Cartesian system) and to establish the elastic properties of each lamina on the laminate system named global system (Daniel; Ishai, 1994).

2.2 Review of displacement theories

There are three different significant assumptions of the displacement field (Reddy, 1989):

- a) Equivalent Single Layer 2D theories;
- b) layerwise 2D theories;
- c) continuum based 3D and 2D theories.

This section reviews the basics of both Equivalent Single Layer (ESL) and the layerwise theory. The continuum-based models are also commented and compared to LW theory.

2.2.1 Equivalent Single Layer Theories

ESL theories or the Kirchhoff based kinematic approach, have been the first of all formulations to model composite laminates. As its name suggests, this category of theories represents a composite laminate as an equivalent single layer. The displacement field of ESL theories is a linear combination of thickness coordinates and functions of positions of a reference surface, as demonstrated in equation (1). Usually, the reference is the mid-plane of the laminate (Reddy, 1989).

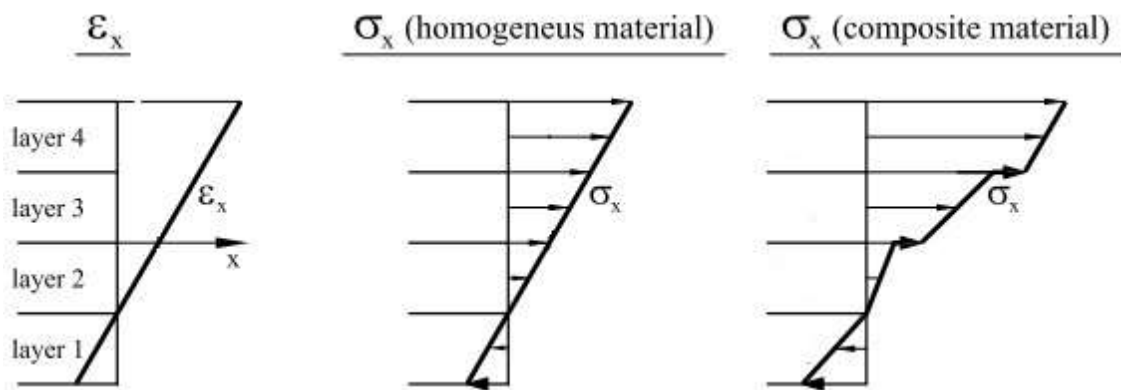
$$u_i(x, y, z) = \sum_{j=0}^{M_i} \hat{u}_i^j z^j \quad ; \quad i = (1, 2, 3) \quad (1)$$

where M_i is the number of terms in expansion of the i -th component of the displacement vector and \hat{u}_i^j are the functions of positions, and Z is the coordinate in thickness direction. For example, if it is desired a cubic interpolation of the displacement field on x and y directions,

then ($M_1 = M_2 = 3$). Hence, a displacement field based on equation (1) will have ($M_1 + M_2 + M_3 + 3$) unknowns per node (Reddy, 1989).

In all ESL theories, the displacement field and its derivatives (the strain field) are continuous through the laminate thickness. Due the fact of each lamina has its own constitutive law, the stress field may be discontinuous on interfaces between laminas, as shown in Figure 6 (Reddy, 1989).

Figure 6 - Typical longitudinal strain and stress in the thickness of a general composite laminate



Modified: Oñate (2009).

The first ESL theory is the Classical Laminate Theory (CLT), which is based on Kirchhoff's plate formulation applied to composite laminates. The principal assumptions of the CLT are:

- a) a state of plane stress is considered over the whole domain;
- b) transverse shear deformations are negligible;
- c) the transverse normal strain is neglected.

The assumption of plane stress is only valid for thin plates. Neglecting the transverse shear deformation implies that vertical lines remain straight and normal to the mid after loading, which may not be adequate for thick plates (Daniel; Ishai, 1994). It is possible to formulate the CLT theory by letting $M_1 = M_2 = 1$ and $M_3 = 0$ in equation (1). The result is stated equation (2).

$$\begin{aligned}
 u_1 &= \hat{u}_1^0 + z\hat{u}_1^1 \\
 u_2 &= \hat{u}_2^0 + z\hat{u}_2^1 \\
 u_3 &= \hat{u}_3^0
 \end{aligned} \tag{2}$$

where the functions \hat{u}_i^0 ; $i = 1, 2, 3$ are the displacements along the three coordinate directions of a system of reference surface (usually the reference is the mid plane), and $(\hat{u}_1^1, \hat{u}_2^1)$ are the rotational angles of y and x axes respectively. It is important to mention the independence of the transverse displacement u_3 in respect to the thickness coordinate, which is expected due to Kirchhoff assumptions (Reddy, 1989). Generally, reasonable results of displacements and in-plane stresses are achieved by applying CLT theory to composite laminates; Liu and Li, (1996) suggest that the thickness should not be twenty times greater than the in-plane dimensions for better results using Equivalent Single Layer theories. The CLT theory does not account out-of-plane stresses, and since some failure mechanisms include interlaminar stresses, the CLT approach may not be adequate for designing primary structures (structures which compromise a whole structural system when failing). Furthermore, due to no transverse shear deformation assumption, the CLT underestimates the transverse deflection (Cho; Parmerter, 1992).

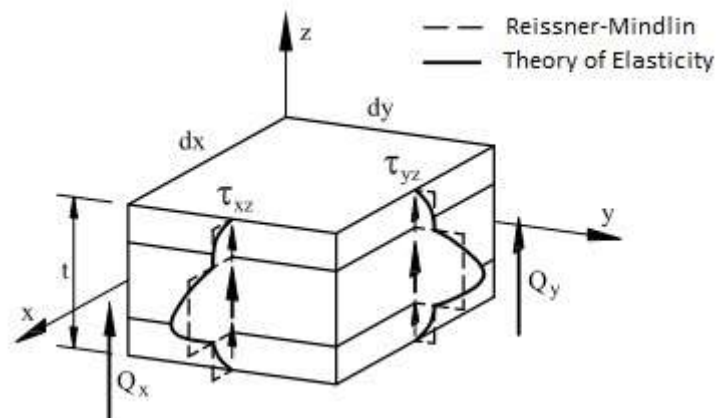
To improve the CLT drawbacks, more sophisticated Equivalent Single Layers theories were developed, such as the First-Order Shear Deformation theories, Higher-Order Shear Deformation theories (HSST) and Zig-zag theories. The First-Order Shear Deformation theory was developed by Reissner (1945) and Mindlin (1951). Their method assumes the same displacement field of Kirchhoff's approach, but it does not ignore the shear deformation, which results in straight lines not perpendicular to midplane after loading (Cho; Parmerter, 1992).

Some advantages to implement finite element solution based in Reissner-Mindlin's kinematics instead of Kirchhoff theories are: The Kirchhoff theory requires that the first derivative of shape functions should be continuous, and the results of the Reissner-Mindlin plate theory are more accurate for thicker beams. In ESL theories, the structural analyzes of

thin laminates can induce to a numerical counterfeit called shear locking, but there are a variety of artifices to bypass this undesired effect such as reduced integration, constrained substitute shear strains fields, or incompatible modes and other techniques (Oñate et al. 1992). The reduced integration is one of the most used approaches, and it is easier to employ, although it can introduce spurious mechanisms which can lead to inaccurate results (Oñate, 2013).

The shear stress acting on a generic cross section assumed on the Reissner-Mindlin's theory is constant, which is a contradiction to the quadratic distribution according to the theory of elasticity as demonstrated in Figure 7. To overcome this circumstance, it is necessary to impose a shear correction factor to match the specific internal energy of the Principle of Virtual Work (Timoshenko, 1930). Conversely, the layerwise theory does not require a shear correction factor, as it will be discussed later.

Figure 7 - Out-of-plane shear stress according to Reissner-Mindlin theory and the Theory of Elasticity

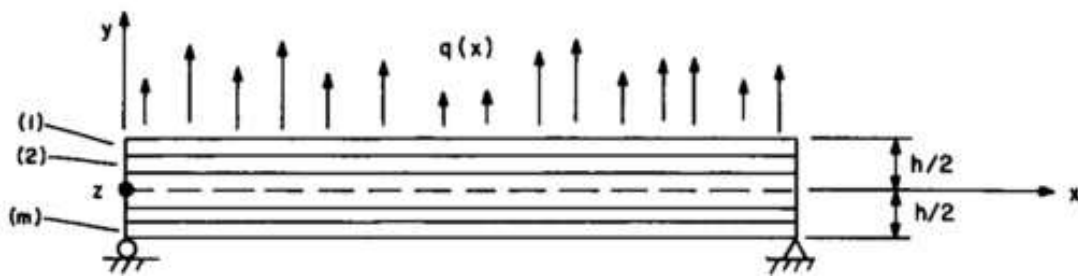


Source: Oñate (2013).

Several higher-order plate theories have been proposed in order to improve ESL theories. Typical examples are the formulations of Lo et al. (1977), which assumed a third order expansion on in-plane displacements and a second order to deflection; the third-order theory of Reddy (1984) that imposes null shear stress on the top and bottom of the laminate; the method developed by Shu and Liangxin (1994), which enforces the shear stress continuity over each layer interface; and others relevant researchers.

Liu and Li (1996) compared several HSDT theories to the elastic solution suggested by Pagano (1969) to cylindrical bending in composite laminates. In their research, they examined the normalized in-plane displacement \bar{u} of a [0/90/0] laminate, whose aspect ratio is equal to 4. The boundary conditions of the example solved by Pagano (1969) is demonstrated in Figure 8

Figure 8 - Cylindrical bending case solved by Pagano (1969)



Source: Pagano (1969).

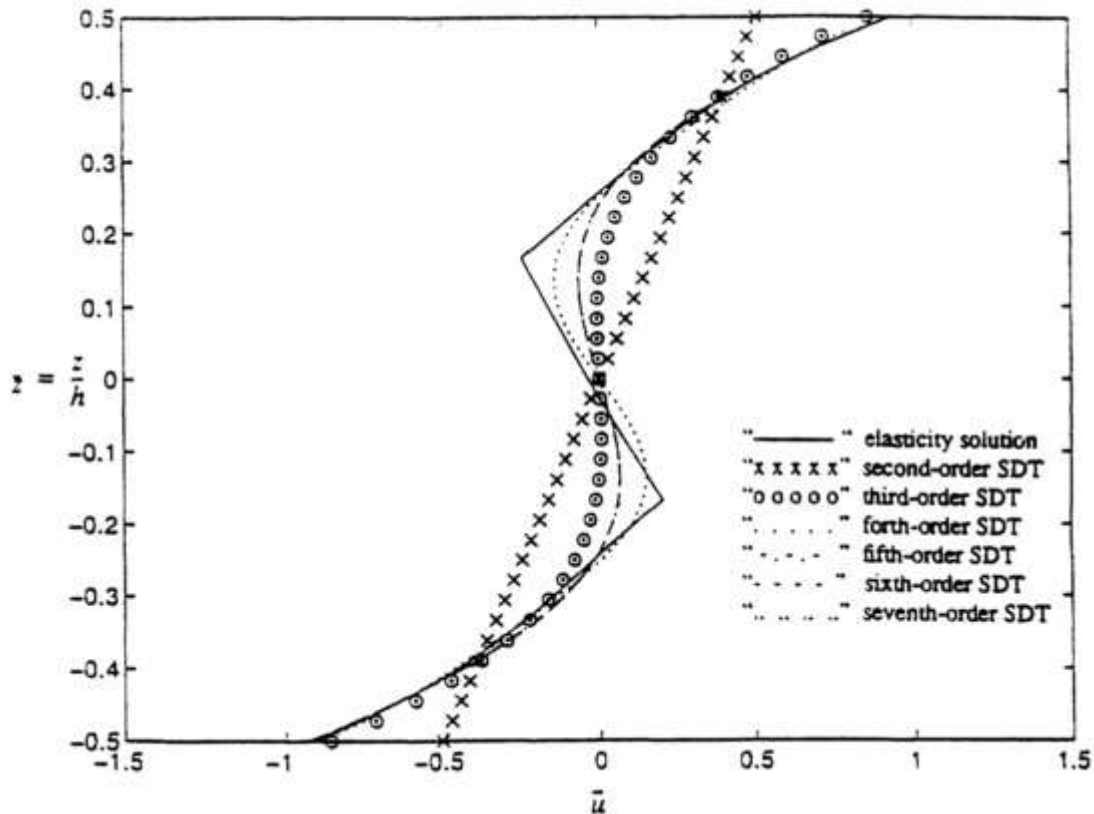
The external load is expressed in form of a Fourier series of equation (3)

$$q(x) = q_0 \sin(p(n)x) ; \quad (3)$$

$$p(n) = \frac{n\pi}{l}$$

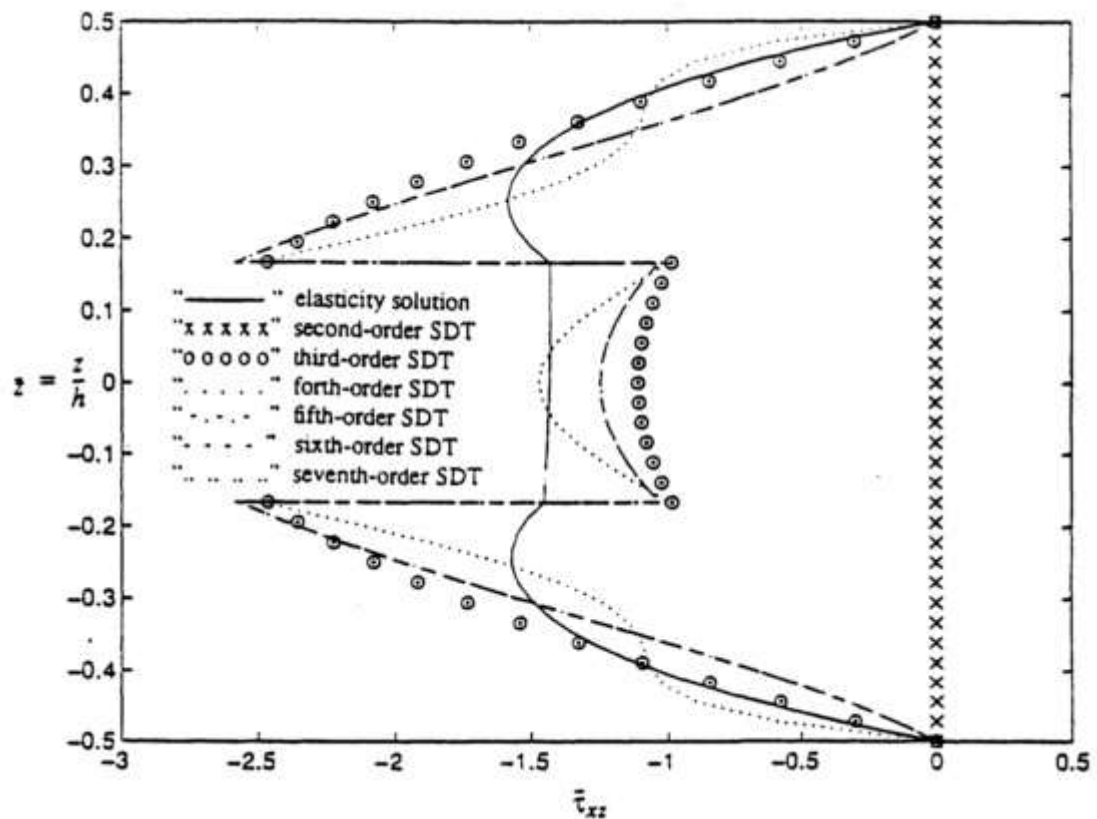
where $q(x)$ is the load in function of x coordinate, q_0 is a constant load, $p(n)$ is the Fourier series, π and l is the length of total length of the laminate.

Liu and Li (1996) pointed out that the results of third and fourth order are identical, and the same applies for the outcome of the fifth and sixth order. These facts can be verified in Figure 9.

Figure 9 - Comparison of \bar{u} from shear deformation theories for a [0/90/0] laminate

Source: Liu and Li (1996).

Liu and Li (1996) proved that the solution to displacement through the thickness in SDT has an excellent agreement to the theory of elasticity. In turn, Reddy (1989) agrees that SDT theories are adequate to represent the global behavior of thin composites, but they are inadequate to represent local effects such as interlaminar stress distributions and delamination. Liu and Li (1996) also investigated the distribution of out-of-plane shear stress along the thickness and proved that the solution indeed disagrees with analytical's. This divergence can be explained due to ESL assumptions of the displacement field; since the strain field is continuous at interfaces between laminae, it is evident that the stress field is discontinuous if the orientation of the adjacent laminae are in different directions. Figure 10 illustrates this divergence. No matter the order of the polynomial approximation, all Shear Deformation Theories show discontinuity of interlaminar shear stresses on interfaces of laminae, which disagrees with the theory of elasticity.

Figure 10 - Comparison of $\bar{\tau}_{xz}$ from shear deformation theories for a [0/90/0] laminate

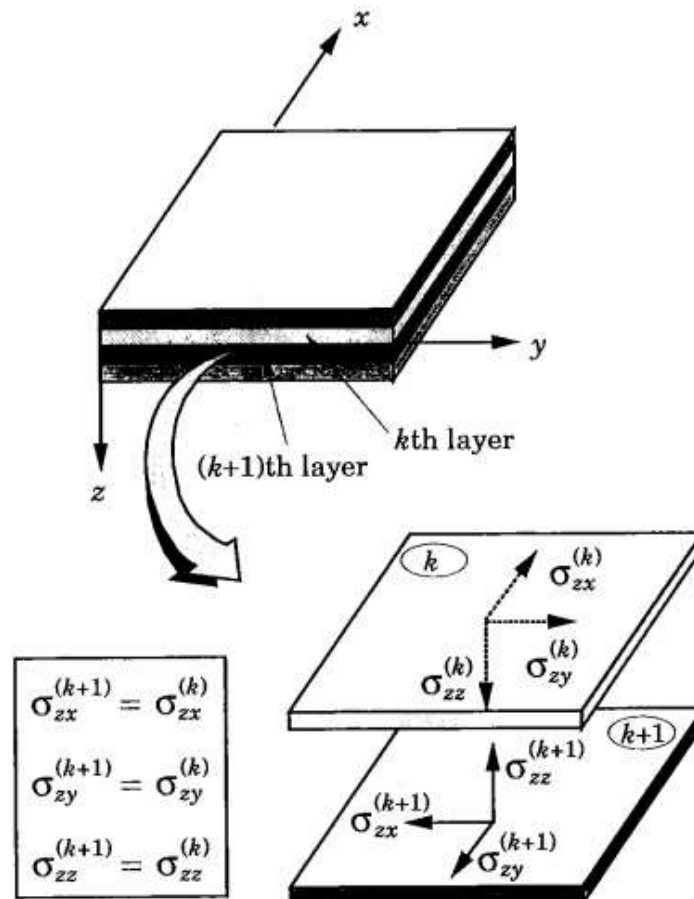
Source: Liu and Li (1996).

2.2.2 Layerwise Displacement Theory

It is crucial to identify the zones of potential damage initiation to design structures adequately. Regarding composite materials, the damage begins at the ply level. Hence it is critical to accurately determine the state of stress and strain at the lamina level. As it was discussed, ESL theories are often incapable of determining all components of the stress field, especially for thicker laminates. Therefore, ESL theories may not be an appropriate formulation to design primary structures. Conversely, formulations based on the 3D elasticity the layerwise are more appropriate. According to Reddy (2004), formulations based on the layerwise are equivalent to continuum based 3D theories, but it demands less computational resources. Hence they could be a viable option to perform structural analyses on primary structures.

To satisfy the equilibrium of interlaminar forces, the out of plane stresses acting on two adjacent plies must be in balance, as demonstrated in Figure 11.

Figure 11 - Equilibrium of out-of-plane stresses between two adjacent layers



Source: Reddy (2004).

To satisfy the continuity of the out-of-plane stresses at interfaces between laminas, Demasi (2009 b) proposes the integration over the thickness of the indefinite equilibrium equations of equation (4); note that it is necessary to compute the out-of-plane shear stresses (σ_{13}, σ_{23}) before the out-of-plane normal stress (σ_{33}).

$$\sigma_{i3,3} = -(\sigma_{i1,1} + \sigma_{i2,2}) \quad (4)$$

The interlaminar strains field of two adjacent plies, however, may be different due the fact of each lamina has its own constitutive law. In ESL theories, the opposite occurs; the continuity is enforced to the interlaminar strains field, not to the interlaminar stress field. This fact contradicts the interlaminar equilibrium equations represented in Figure 11. This shortcoming is often negligible for thin laminate. However it can result in unsatisfactory results to thicker laminates (Reddy, 2004).

The layerwise theory developed by Reddy (1987) is capable of providing the correct zigzag in-plane displacements along the thickness direction, same behavior noted in the analytic solution of Figure 9. The displacement field is given in equation (5).

$$\begin{aligned} u_1(x, y, z) &= u(x, y) + U(x, y, z) \\ u_2(x, y, z) &= v(x, y) + V(x, y, z) \\ u_3(x, y, z) &= w(x, y) + W(x, y, z) \end{aligned} \quad (5)$$

where (u, v, w) are the displacements of a point on the reference plane (usually the mid-plane), and (U, V, W) are coordinate functions which vanish on the reference plane (Reddy, 1987).

The infinitesimal strains associated to the displacement field of equation (5) are given in equation (6).

$$\begin{aligned}
\varepsilon_{xx} &= u_{,x} + U_{,x} \\
\varepsilon_{yy} &= v_{,y} + V_{,y} \\
\varepsilon_{zz} &= W_{,z} \\
\varepsilon_{xy} &= \frac{1}{2} \left[(u_{,y} + v_{,x}) + (U_{,y} + V_{,x}) \right] \\
\varepsilon_{xz} &= \frac{1}{2} \left[U_{,z} + w_{,x} + W_{,x} \right] \\
\varepsilon_{yz} &= \frac{1}{2} \left[V_{,z} + w_{,y} + W_{,y} \right]
\end{aligned} \quad (6)$$

The Principle of Virtual Work of formulated in equation (7) can be invoked to derive a consistent set of differential equations which governs the mechanical response of the laminate in absence of body forces, specified tractions and inertial forces,

$$\int_V \left[\sigma_{xx} \delta \varepsilon_{xx} + \sigma_{yy} \delta \varepsilon_{yy} + \sigma_{zz} \delta \varepsilon_{zz} + 2(\sigma_{xy} \delta \varepsilon_{xy} + \sigma_{xz} \delta \varepsilon_{xz} + \sigma_{yx} \delta \varepsilon_{yx}) \right] dV - \int_{\Omega} q \delta u_3 dA = 0 \quad (7)$$

Substituting the strain field of equation (6) into equation (7) leads to the variational formulation of equation (8)

$$\begin{aligned}
& \int_{-h/2}^{h/2} \int_{\Omega} \left[\sigma_{xx} (\delta u_{,x} + \delta U_{,x}) + \sigma_{yy} (\delta v_{,y} + \delta V_{,y}) + \right. \\
& \left. \sigma_{zz} \delta W_{,z} + \sigma_{xy} (\delta u_{,y} + \delta v_{,x} + \delta U_{,y} + \delta V_{,x}) + \right. \\
& \left. \sigma_{xz} (\delta U_{,z} + \delta w_{,x} + \delta W_{,x}) + \sigma_{yz} (V_{,z} + w_{,y} + W_{,y}) \right] dA dz \\
& = \int_{\Omega} q \delta (w + W) dA
\end{aligned} \quad (8)$$

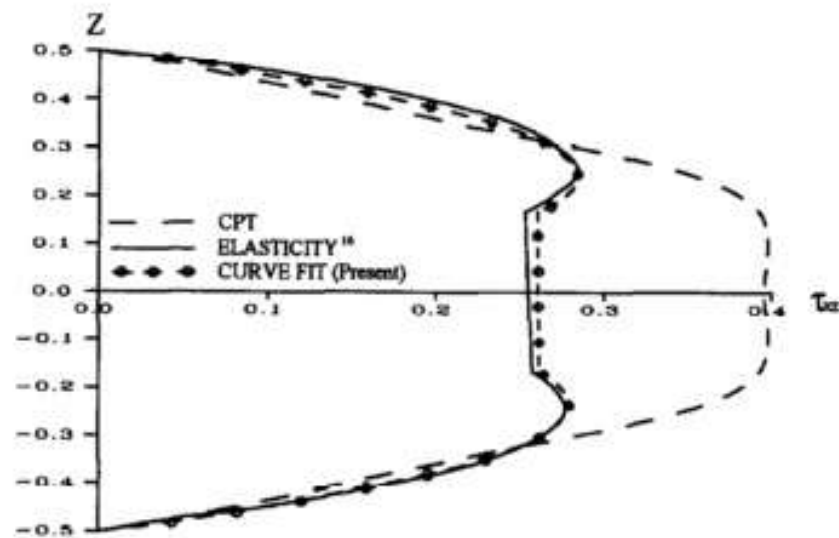
In order to reduce the 3D variational formulation expressed in equation (8) to a two dimensions, it is necessary to approximate the functions (U, V, W) as stated in equation (9).

$$\begin{aligned} U(x, y, z) &= \sum_{j=1}^n U_j(x, y) \Phi_j(z) \\ V(x, y, z) &= \sum_{j=1}^n V_j(x, y) \Phi_j(z) \\ W(x, y, z) &= \sum_{j=1}^m W_j(x, y) \Psi_j(z) \end{aligned} \quad (9)$$

where $U_j(x, y)$, $V_j(x, y)$ and $W_j(x, y)$ are undetermined coefficients and $\Phi_j(z)$ and $\Psi_j(z)$ are the layerwise continuous functions which vanish on the reference plane. Equation (9) can be interpreted as the global semi-discrete finite element approximation (U, V, W) through the thickness. The functions $\Phi_j(z)$ and $\Psi_j(z)$ are the global interpolation functions through the thickness, whereas $U_j(x, y)$, $V_j(x, y)$ and $W_j(x, y)$ are the nodal values of (U, V, W) (and maybe their derivatives) at the nodes on the thickness direction. The variable n and m depends on the order of the expansion through the thickness. According to Reddy (1989), the interlaminar stresses can be accurately predicted at interfaces if at least one layer is discretized per ply. Obviously, the more layers discretized in the cross section of the laminate the more accurate will be the result, but the computational efficiency decreases proportionally. To approach thicker composite laminate structures, one could also consider discretizing less virtual layers, , if possible.

Figure 12 compares the interlaminar stress τ_{xz} between the layerwise theory presented by Kam and Jan (1995) to the elasticity solution and the Classical Plate Theory (CPT); they have concluded in their research that theories based on the layerwise are indeed more accurate than CPT.

Figure 12 - Comparison of the interlaminar stress τ_{xz} according to CPT, Elasticity solution, and layerwise theory of Kam and Jan (1995)

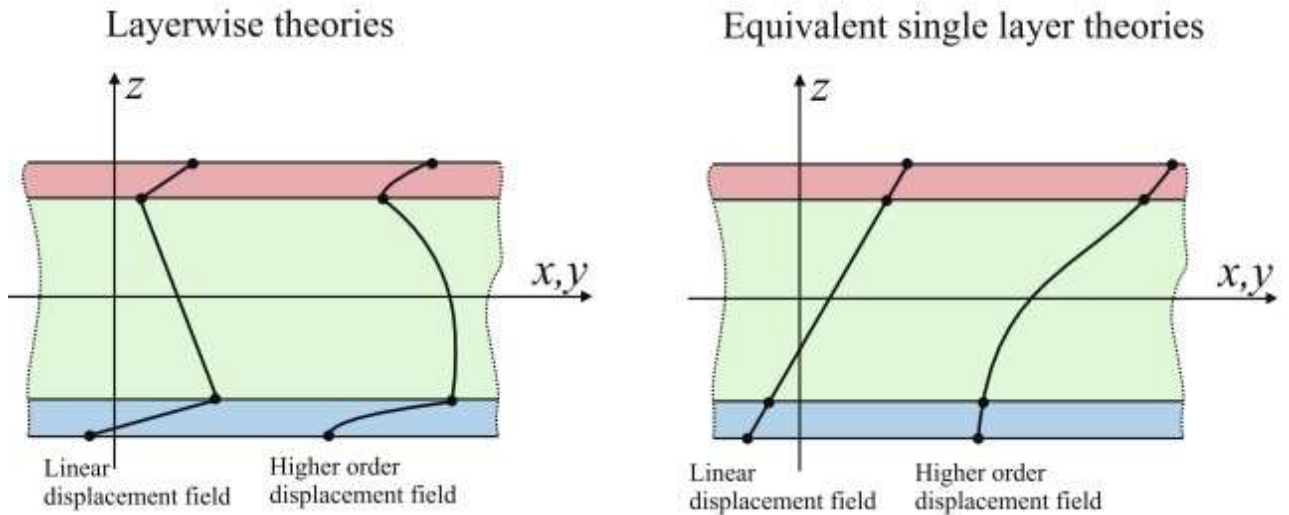


Source: Kam and Jan (1995).

Subsequently, other relevant researches have been carried out regarding the displacement field based on LW theories. Barbero and Reddy (1991) modeled delamination in composite laminates using the layerwise theory; Cho and Parmerter (1992) formulated a refined higher-order layerwise displacement theory; Botello and Oñate. (1999) developed a finite element analysis for plate and shells based on a triangle element with layerwise discretization; the mixed plate theory based on a Generalized Unified Formulation by Demasi (2009); Barouni and Saravanos (2017) developed a semi-analytical method for modeling guided-wave propagation over a composite laminate.

In Figure 13, both linear and higher-order displacement field based on LW theory are illustrated and compared to general ESL theories. Note the abrupt change of the displacement field's derivative of the LW theories at lamina interfaces (represented by a kink). This discontinuity of the strain field occurs due to the balance of stresses between two adjacent laminas explained before. Conversely, ESL theories impose the strain continuity through the thickness, and because of it, the displacement field does not have the zigzag pattern, unless it is implemented additional zigzag functions to the ESL displacement field.

Figure 13 - Comparison of displacement distribution through the thickness of ESL theory and layewise theory

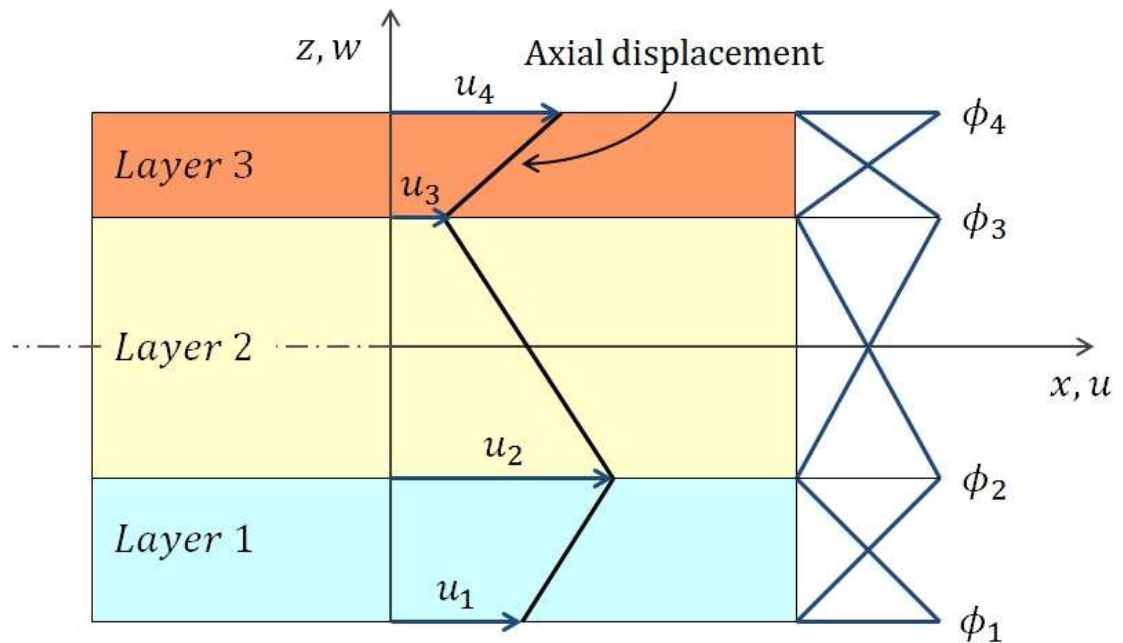


Source: Demasi (2009 b).

Zigzag patterns can be achieved in ESL theories by implementing a special zigzag function to the displacement field, and by enforcing the continuity of the shear stresses through the thickness (Tessler et al., 2009). The Zigzag theory implemented to ESL theories results in displacement fields similar to the linear layerwise shown in Figure 13.

Figure 14 schematically illustrates a linear interpolation through the thickness using Legendre polynomials for a three-layered laminate; note the similarity of the distribution of the linear layerwise functions to the distribution of a two-node bar element. Each layerwise $\Phi_j(z)$ function presented in is the interpolation function associated to the j -th node. Therefore, at interfaces between two laminas, the $\Phi_j(z)$ function should be compatible. This compatibility requirement is fulfilled by choosing a layerwise function that is continuous, piecewise and compatible at interfaces.

Figure 14 - Linear layerwise functions and nodal displacements through the thickness in a three-layered composite plate



Source: Modified (Oñate, 2013).

An example of a compatible set of function that fulfill the layerwise requirements are the Legendre polynomials defined in the interval of $[-1, 1]$. A transformation of variables is needed to convert the global reference system to domain of $[-1, 1]$, as suggested in equation (10) (Demasi, 2009b).

$$\zeta_k = \frac{2}{z^{(k+1)} - z^{(k)}} z - \frac{z^{(k+1)} + z^{(k)}}{z^{(k+1)} - z^{(k)}} \quad (10)$$

The explicit forms of the Legendre polynomials of orders zero to five are demonstrated in equation (11), and for higher-orders the formulation is written in equation (12).

$$\begin{aligned}
 P_0(\zeta_k) &= 1; \\
 P_1(\zeta_k) &= \zeta_k; \\
 P_2(\zeta_k) &= \frac{3(\zeta_k)^2 - 1}{2}; \\
 P_3(\zeta_k) &= \frac{5(\zeta_k)^3 - 3\zeta_k}{2}; \\
 P_4(\zeta_k) &= \frac{35(\zeta_k)^4 - 30(\zeta_k)^2 + 3}{8}; \\
 P_5(\zeta_k) &= \frac{63(\zeta_k)^5 - 70(\zeta_k)^3 + 15\zeta_k}{8};
 \end{aligned} \tag{11}$$

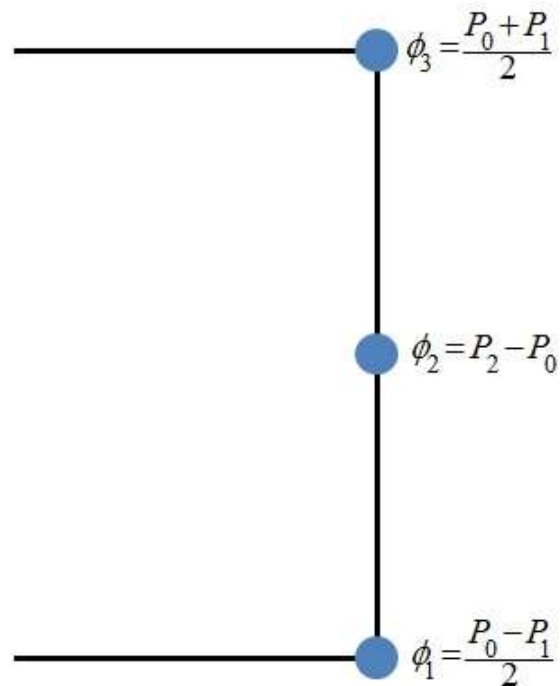
$$P_{s+1}(\zeta_k) = \frac{(2s+1)\zeta_k P_s(\zeta_k) - sP_{s-1}(\zeta_k)}{s+1} \tag{12}$$

Within a layer, the layerwise functions based on the Legendre polynomials are expressed in equation (13):

$$\begin{aligned}
 \phi_1 &= \frac{P_0 - P_1}{2}; \\
 \phi_{L^*} &= \frac{P_0 + P_1}{2}; \\
 \phi_s &= P_s - P_{s-2} \quad | \quad 1 < s < L^*
 \end{aligned} \tag{13}$$

where L^* is the total number of plies and n is the index of the n th layerwise function. If is desired a parabolic interpolation through the thickness using the layerwise theory, for instance, the layerwise functions within a single layer will be as described in figure Figure 15

Figure 15 - Example of a layerwise quadratic interpolation through the thickness within a layer based in the Legendre polynomials

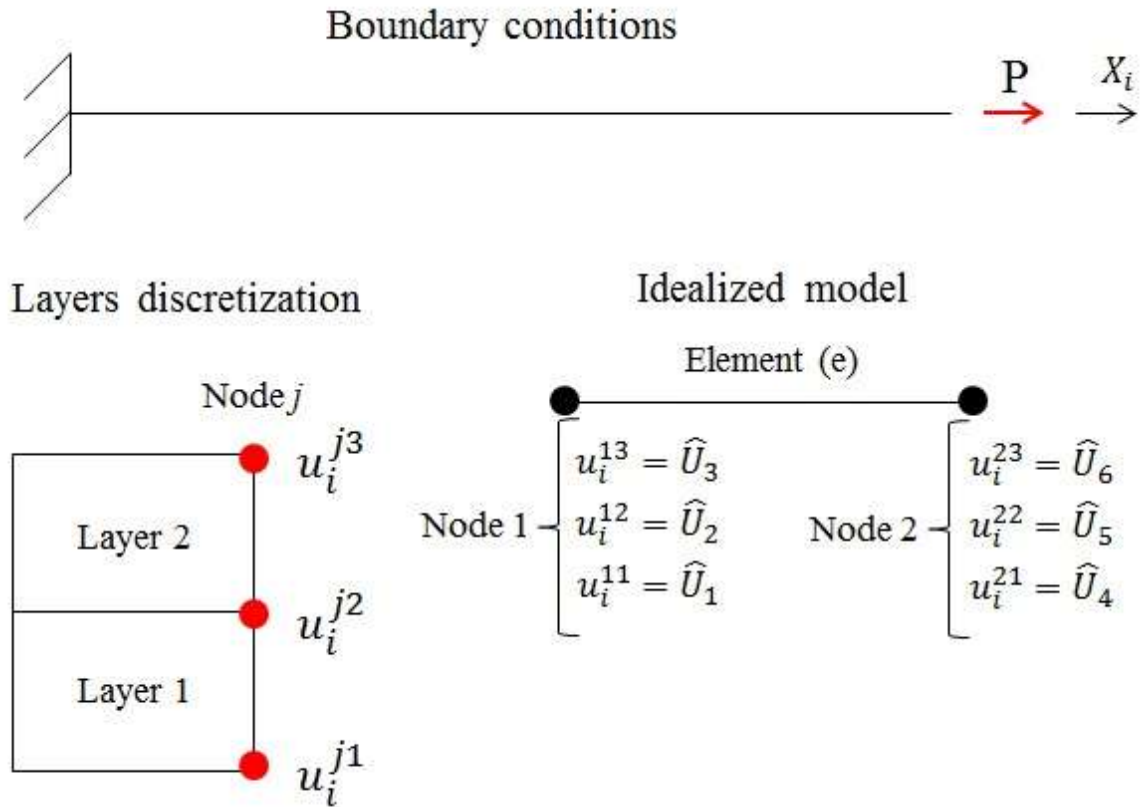


Source: Author.

It is possible to choose other layerwise functions, such as the Hermite cubic polynomials (Reddy, 1987). Another advantage of the layerwise theory is the fact that this formulation avoids shear locking even for linear interpolation in thick composites (Reddy, 1989).

To illustrate the assemble of the linear system and how to apply boundary conditions with the layerwise approach, consider the case of Figure 16, a fixed bar idealized as a single 1D element with two layers with linear interpolation through the thickness. Note that the degrees of freedom in the local system are expressed as u_i^{jk} , where j is the node and k is the layer index. The subscript i indicating the direction is redundant because the case presented has degrees of freedom in only one direction; however this notation is used further in this dissertation, thus it has been opted to introduce it forthwith. The degree of freedom is expressed in the global system as \hat{U}_j (hence this case has six degrees of freedom).

Figure 16 - Illustrative case of a two-layer 1D element with linear layerwise interpolation through the thickness



Modified from: Vilar et al (2018).

The linear system of the problem illustrated in Figure 16 is expressed in Figure 17. Observe that that compatibility of displacements at interfaces are imposed by performing the assemble of two adjacent laminas, as is emphasized in Figure 17. The first superscript of the elemental stiffness matrix K refers to the number of the lamina and the second is the number of the node. If the mesh is refined, than is necessary another index to represent the element number.

To introduce the boundary conditions of the fixed end is necessary to impose $\hat{U}_1 = \hat{U}_2 = \hat{U}_3 = 0$; restraining all the degrees of freedom of the node fixed is sufficient to restrict the rotation of it. If is desired to insert a simple support, only the degrees of freedom related to the bottom plane should be forced to zero, therefore in this case it would have been $\hat{U}_1 = 0$. The nodal force P can be applied to the positions 4th to 6th of the force vector;

$F_4 = P$ means that the nodal force P is being applied to the bottom plane of the laminate, $F_5 = P$ implies that the nodal force is at the interface between the layers and $F_6 = P$ is at the upper plane of the laminate.

Figure 17 - Global linear system of the problem of Figure 16

$$\begin{bmatrix}
 K_{11}^{(1)(1)} & K_{12}^{(1)(1)} & 0 & 0 & 0 & 0 \\
 K_{22}^{(1)(1)} + K_{11}^{(1)(2)} & K_{12}^{(1)(2)} & 0 & 0 & 0 & 0 \\
 K_{12}^{(1)(2)} & K_{22}^{(1)(2)} & 0 & 0 & 0 & 0 \\
 0 & 0 & 0 & K_{11}^{(2)(1)} & K_{12}^{(2)(1)} & 0 \\
 0 & 0 & 0 & K_{12}^{(2)(1)} & K_{22}^{(2)(1)} + K_{11}^{(2)(2)} & 0 \\
 0 & 0 & 0 & 0 & 0 & K_{22}^{(2)(2)}
 \end{bmatrix}
 \begin{Bmatrix}
 \hat{U}_1 \\
 \hat{U}_2 \\
 \hat{U}_3 \\
 \hat{U}_4 \\
 \hat{U}_5 \\
 \hat{U}_6
 \end{Bmatrix}
 =
 \begin{Bmatrix}
 F_1 \\
 F_2 \\
 F_3 \\
 F_4 \\
 F_5 \\
 F_6
 \end{Bmatrix}$$

\downarrow
 SYM
 \downarrow
 Compatibility imposed

Modified from: Vilar et al (2018).

2.3 Extended Finite Element Method

The Finite Element Method (FEM) procedure is widely applied to engineering analyses. Firstly, the FEM was developed to fulfill problems of structural mechanics, but afterward, it was also utilized to solve fluid and heat transfer problems (Bathe, 1996). Recently, researchers introduced the concepts of linear elastic fracture mechanics (LEFM) to FEM. LEFM can now rely on an effective numerical procedure to solve fundamental problems such as crack energy release rate and stress intensity factor, delamination (Mohammadi, 2008).

According to Mohammadi (2008), the essence of XFEM is to employ linear elastic fracture mechanic basic concepts to the classical continuum based techniques through smeared or discrete crack FEM models. Therefore, a crack propagation problem, such as delamination in composite plates, can be approached through the XFEM analysis; the procedure is to discretize out of plane discontinuities at the interface between layers.

Based on the idea of partition of unity of Melenk and Babuška (1996), the XFEM studies initiated by Belytschko and Black (1999). Their model was a minimum remeshing procedure applicable to two-dimensional cases; the stress intensity factors was also possible to calculate with a difference of less than 1% when compared to analytical solutions (Belytschko; Black, 1999). Next, Moës et al. incorporated a discontinuous field across crack faces away from crack tips. As a result, no remeshing was required to propagate the discontinuity, because the shape of the crack is independent to the mesh (Moës et al.1999).

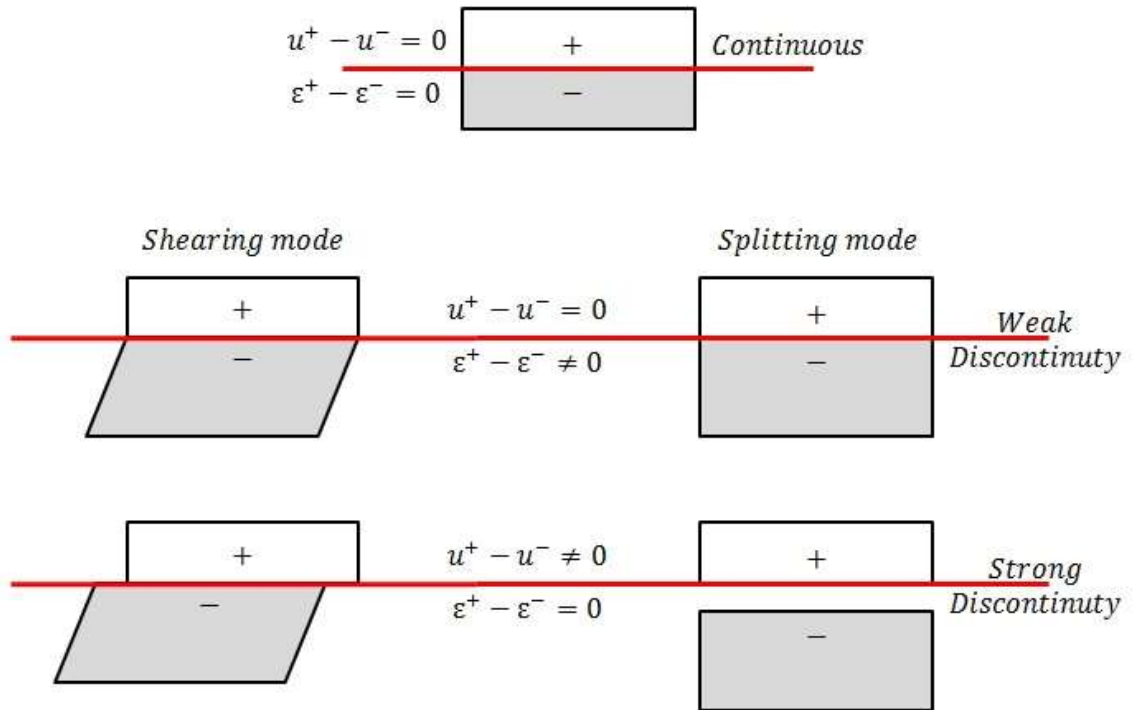
Later, Dolbow et al. (2001) presented an XFEM formulation for Mindlin-Reissner plates using jump and crack tip functions to enrich the displacement field. The crack tip enrichments were able to dismiss the necessity of mapping the crack tip. Subsequently, Moës and Belytschko (2002) implemented a cohesive law on crack surfaces, turning possible to approach the crack propagation by Cohesive Zone Method.

In short, the XFEM was adapted to orthotropic and layered materials. Remmers et al. (2003) presented a formulation for delamination growth to thin composite structures. Afterward, numerous crack tip enrichment functions for orthotropic materials were reported in several papers, such as Asadpoure et al. (2006a), Mohammadi and Asadpoure (2006). Other recent studies extended the XFEM application to composites by modeling laminate behavior using different approaches, such as multiple delaminations of Brouzoulis and Fagerström (2013); random crack initiation investigated by Grogan et al. (2015).

Novel studies have combined both layerwise displacement theory and XFEM procedures. Li et al. (2015a) proposed a composite beam element with multiple delamination and cracks using both XFEM and LW. Next, Li et al. (2015b) extended their previous formulation to shell elements.

XFEM permits discontinuity of the displacement and strain fields. A discontinuity in the displacement field is designated as strong discontinuity, whereas weak discontinuity modify the strain fields, as demonstrated in Figure 18 (Mohammadi, 2008). Weak discontinuities are also applied to determine the stress intensity faction near the crack tips.

Figure 18 - Categories of discontinuities on XFEM



Source: Mohammadi (2008).

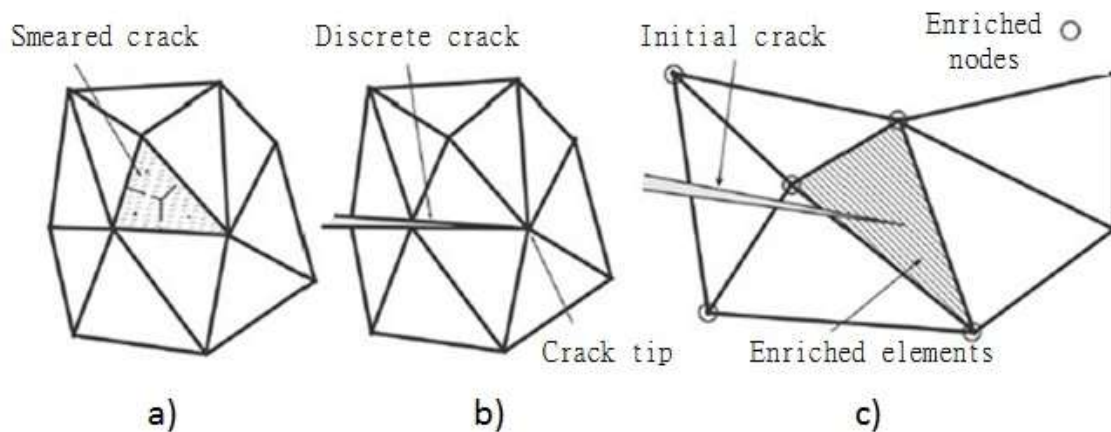
There are several approaches to model crack problems through finite elements. One example is the smeared crack, represented in Figure 19 – a). This technique considers the element as continuous, but it penalizes stiffness and/or strength to elements located on the crack domain. On the post-processing of each interaction, the smeared crack approach checks the failure criteria on defined coordinates within each element, usually on Gauss points. Therefore, this approach is mesh-dependent, because the size of elements interferes in the number of checked points and the geometry of the discontinuity (Mohammadi, 2008).

Another possibility to model the crack is the discrete inter-element crack. In this approach, classical FEM is used. The mesh contours the crack geometry, leaving blank spaces to represent the shape of the discontinuity, as is illustrated in Figure 19 – b). This method cannot account for the singularity around the crack tip unless particular singular

finite elements are used. Another drawback is that one has to remesh as the crack grows (Mohammadi, 2008).

The XFEM approach consists of enriching the displacement field of the group of elements within the crack's domain. A set of enrichment functions will be added to the classical displacement field of the FEM approximation. This technique avoids remeshing and permits the designer more flexibility to model the crack initiation and its propagation (Moës et al., 1999). Figure 19 – c) schematically represents the XFEM approach.

Figure 19 - Techniques to model cracks in Finite Elements numerical solution: a) smeared crack; b) inter-element crack; c) XFEM enrichments.



Source: Mohammadi (2008).

The base of XFEM is the partition of unity proposed by Melenk and Babuška (1996). A partition of unity consists of a set of m functions such that its sum is always equal to one within a determined domain, as defined in equation (14).

$$\sum_{k=1}^m f_k(x) = 1 \quad (14)$$

The distribution of shape functions within an element is an example of the partition of unity itself, as expressed in equation (15). Although this formulation seems ordinary, it provides an essential role in the development of an enriched solution (Mohammadi, 2008).

$$\sum_{j=1}^{NN} N_j(x) = 1 \quad (15)$$

Enrichments can be regarded as the process of increasing the order of completeness of trial solutions. There are two ways to perform enrichments: intrinsically or extrinsically. The intrinsic enrichment employs special shape functions near the vicinity of the discontinuity, so it is possible to simulate more complex displacement fields. The primary advantage of intrinsic enrichment is the fact that it does not increase the number of unknowns (Fries; Belytschko, 2006). Conversely, extrinsic enrichments enhance the order of completeness by adding more terms to the classical FEM approximation. Consequently, this procedure increases the number of degrees of freedom and requires special functions to simulate the crack discontinuity influence of stress and displacement fields, as is shown in equation (16) (Moës et al., 1999).

$$u_i(x) = \sum_{j=1}^{NN} N_j(x) u_i^j + \sum_{k=1}^E f_k(x) \rho_k \quad (16)$$

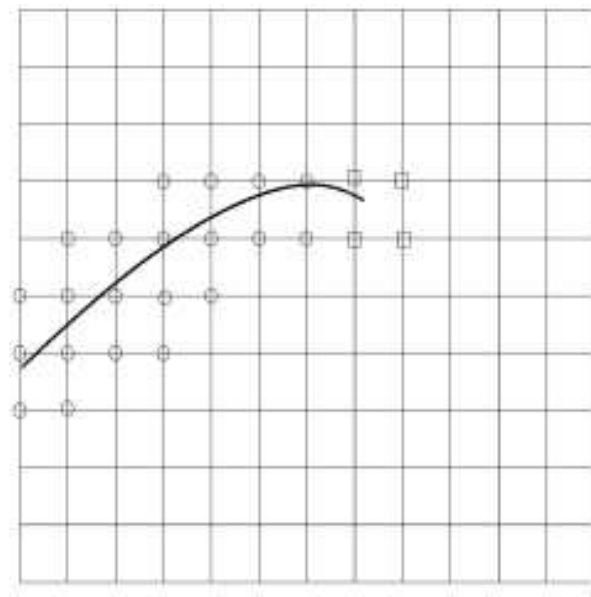
where NN are the number of nodes of the element and E are the set of enriched nodes; and ρ_k are the additional degrees of freedom and $f_k(x)$ is the function associated to the enrichment. In this section, the notation of the standard degree of freedom is u_i^j ; the superscript k is suppressed because the formulation of pure XFEM is not based in a layerwise displacement field. Later the notation of degree of freedom is u_i^{jk} as in the former section.

Initially, XFEM approximations were employed to simulate strong discontinuities in fracture mechanics problems. Later, it was included weak discontinuity and interface

problems to solve more complicated cases, mixing both strong and weak discontinuities. In this method, it is necessary to enrich nodes only in the vicinity of the crack (Mohammadi, 2008). Moreover, the nodes of the element which contains the crack tip may be enriched by different functions to account unique effect around the crack tips such as the stress intensity factor.

In Figure 20, the elements that the crack completely crosses are enriched differently from the element which holds the crack tip (to illustrate the symbol of the nodes of the element containing the crack tip are squares and the other are circles).

Figure 20 - Enriched nodes selected to enrich on a FEM mesh



Source: Moës et al. (1999).

The XFEM's displacement field based on extrinsic enrichments is described by equation (17):

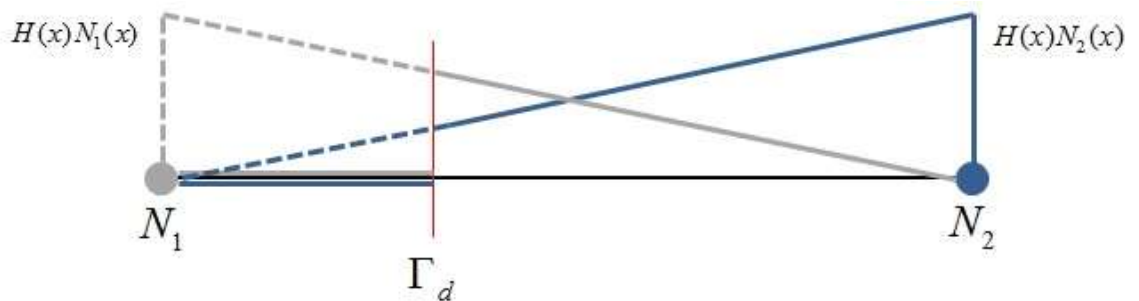
$$u_i(x) = \sum_{j=1}^{NN} N_j(x) u_i^j + \sum_{k=1}^E N_k^*(x) \psi(x) \rho_k \quad (17)$$

where the first term of the right-hand side is the classical FEM approximation and the second is related to the XFEM enrichment, $\psi(x)$ are the set of enrichment functions (Mohammadi, 2008).

If it is desired to simulate more than one discontinuity (both weak and strong discontinuities for instance), it is necessary to break the second term of the right-hand side of equation (17) in additional groups. The $N_k^*(x)$ shape functions are the classical FEM shape functions, and it also is an example of a partition of unity.

To model strong discontinuities, the enrichment function should simulate a leap on the displacement field in the crack's domain. It is demonstrated in Figure 21 an element with a single crack. In this illustration, a strong discontinuity is at Γ_d in the element. The enriched nodes are those in the vicinity of the crack. Therefore, only nodes number 1 and 2 are enriched (Mohammadi, 2008).

Figure 21 - Heaviside function multiplied by the standard shape function of a two-node 1D element



Source: Author.

An ordinary enrichment function to simulate the strong discontinuity is the Heaviside function $H(\xi)$. Equations (18) and (19) express some different designations of the Heaviside. They are also called step and sign functions respectively (Mohammadi, 2008).

$$H(\xi) \begin{cases} 1, & \xi \geq 0 \\ 0, & \xi < 0 \end{cases} \quad (18)$$

$$H(\xi) \begin{cases} 1, & \xi \geq 0 \\ -1, & \xi < 0 \end{cases} \quad (19)$$

A typical approximated displacement field with only strong enrichment is demonstrated in equation (20).

$$u_i(x) = \sum_{j=1}^{NN} N_j(x) u_i^j + \sum_{k=1}^S N_k(x) H(x) \lambda_k \quad (20)$$

where S are the set of strong enriched nodes and λ_k are the degrees of freedom associated to strong discontinuities

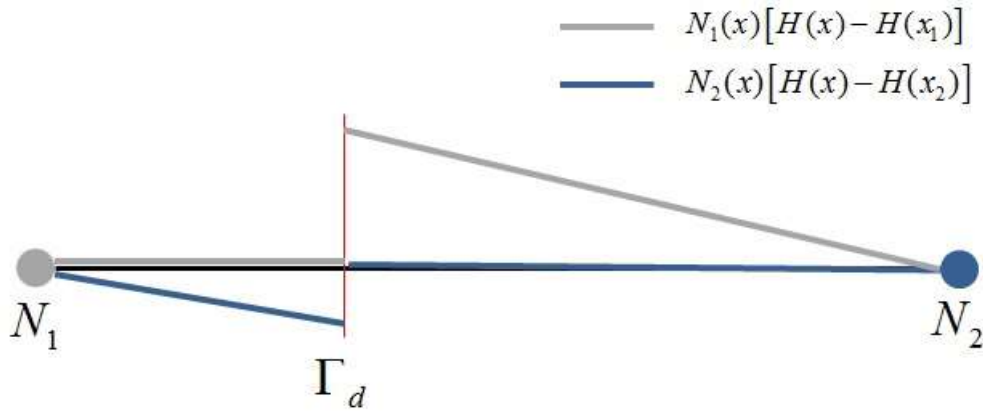
Note that, substituting the coordinates of the j -th node to equation (20) will result in equation (21), which means that the interpolation of equation (20) does not result in the original nodal parameters at the nodes coordinates (it should be $u_i(x_j) = u_i^j$ at the coordinate x_j)

$$u_i(x_j) = u_i^j + H(x_j) \lambda_j \quad (21)$$

Mohammadi (2008) suggests shifting the shape function around the node of interest as described in equation (22). The result of the shifted shape functions represented in Figure 22. Performing this procedure causes $u_i(x_j) = u_i^j$.

$$u_i(x) = \sum_{j=1}^{NN} N_j(x) u_i^j + \sum_{k=1}^S N_k(x) [H(x) - H(x_k)] \lambda_k \quad (22)$$

Figure 22 - Shape functions with shifted effect



Source: Author.

Consider now a weak discontinuity on the same one-dimensional problem. The XFEM approximation can be defined by substituting the enrichment function $\psi(x)$ of equation (17) by an adequate enrichment function demonstrated on equation (23) (Mohammadi, 2008).

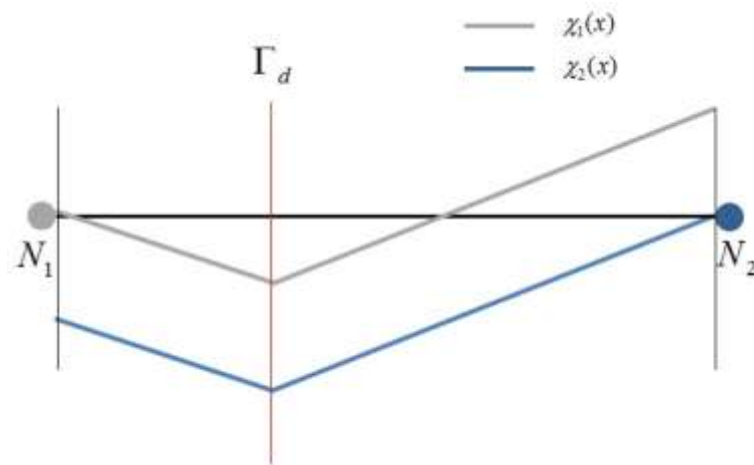
$$u_i(x) = \sum_{j=1}^{NN} N_j(x) u_i^j + \sum_{k=1}^W N_k(x) \chi(x) \mu_k \quad (23)$$

Where W are the set of nodes with weak enrichments; μ_k are the additional degrees of freedom associated with the weak enrichment; and $\chi(x)$ is the weak discontinuous enrichment function in terms of sign distance function, defined in equation (24) (Mohammadi, 2008).

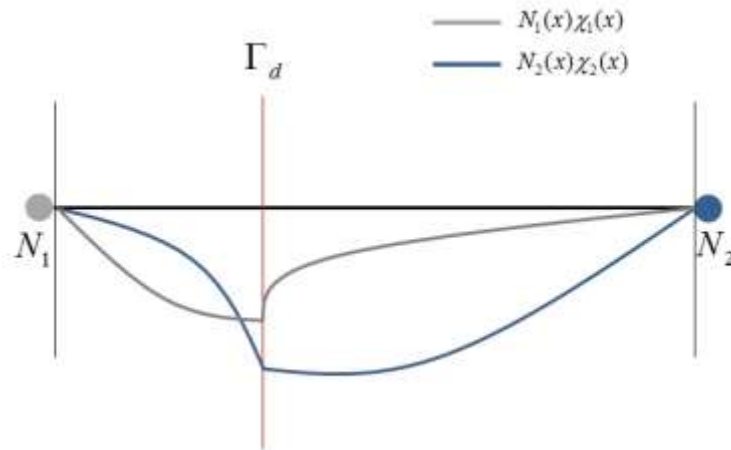
$$\chi(x) = |\xi(x)| - |\xi(x_k)| \quad (24)$$

Figure 23 illustrates both weak enrichment function behavior throughout an element, and how it affects when multiplied by the standard shape functions. Note that the enriched shape functions are continuous all over its domain, but it has a kink at the crack location to simulate discontinuity on the strain field (Mohammadi, 2008).

Figure 23 - a) Functions to model weak discontinuities; b) functions to model weak discontinuities times the standard shape function



a)



b)

Source: Author.

Both weak and strong discontinuities can be inserted into the displacement field. Equation (25) is the displacement field for isotropic elements proposed by Moës et al.(1999).

$$\begin{aligned}
 u_i(x) = & \sum_{j=1}^{NN} N_j(x)u_i^j + \sum_{k=1}^S N_k(x)H(x)\lambda_k + \\
 & \sum_{h=1}^{T_1} N_h(x) \left(\sum_{l=1}^{T_F} F_l^{(1)}(x)b_h^{l1} \right) + \\
 & \sum_{h=1}^{T_2} N_h(x) \left(\sum_{l=1}^{T_F} F_l^{(2)}(x)b_h^{l2} \right)
 \end{aligned} \tag{25}$$

where T_1 and T_2 are the set of nodes enriched with crack tip enrichments (each side of the crack), $F_l^{(1)}$ and $F_l^{(2)}$ represent the T_F crack tip enrichment functions, and b_h^{l1} and b_h^{l2} are additional degrees of freedom related to each crack tip.

Since there is no crack tip enrichments in the formulation proposed here, the crack tip enrichments are not reviewed any further. For additional information regarding how to perform crack tip enrichments and how to evaluate the stress intensity factor, check the investigations of Belytschko and Black (1999), Carloni et al. (2003), Asadpoure et al. (2006b) and Mohammadi (2008)

Analogically to equation (22), the displacement field of equation (25) can be expressed as follows in equation (26) (Mohammadi, 2008). Note that, the extra degrees of freedom b_h^{l1} and b_h^{l2} refer to both crack tips of the discontinuity. In consequence, only if the crack is completely inside the element domain that both values of b_h^{l1} and b_h^{l2} will be different of zero. Assuming that the finite element mesh is sufficient refined, a single element should note have both unknowns b_h^{l1} and b_h^{l2} .

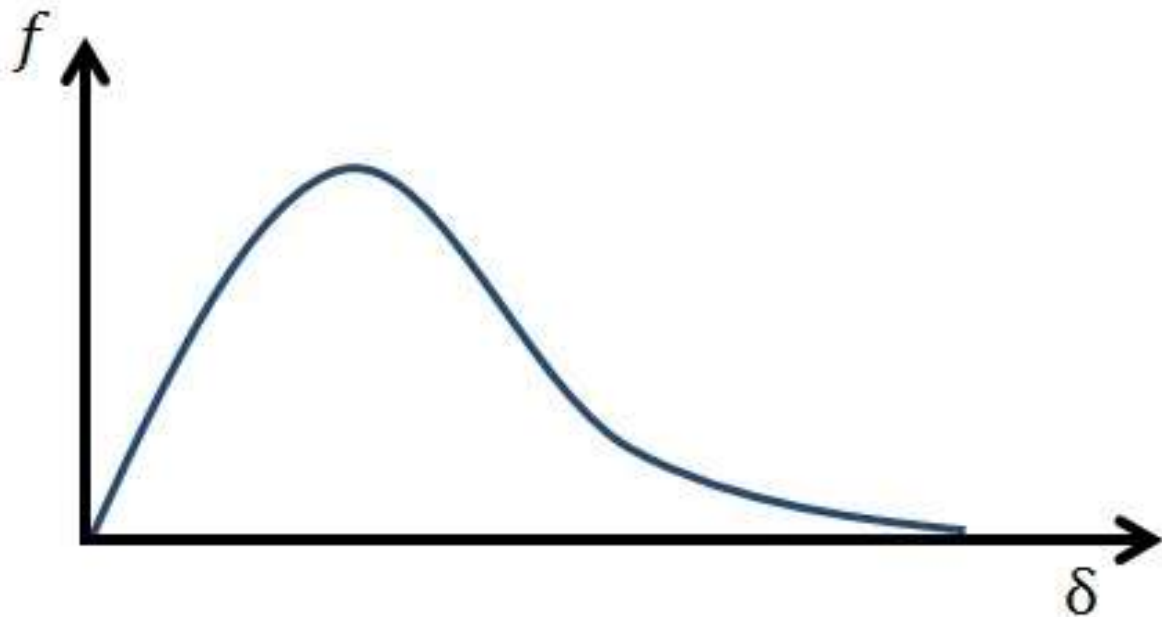
$$\begin{aligned}
u_i(x) = & \sum_{j=1}^{MN} N_j(x) u_i^j + \\
& \sum_{k=1}^S N_k(x) [H(x) - H(x_k)] \lambda_k + \\
& \sum_{h=1}^{T_1} N_h(x) \left(\sum_{l=1}^{T_F} [F_l^{(1)}(x) - F_l^{(1)}(x_l)] b_h^{l1} \right) + \\
& \sum_{h=1}^{T_2} N_h(x) \left(\sum_{l=1}^{T_F} [F_l^{(2)}(x) - F_l^{(2)}(x_l)] b_h^{l2} \right)
\end{aligned} \quad (26)$$

To improve numerical convergence of XFEM analyses, it is possible to employ a cohesive law to govern the traction-separation behavior of the discontinuity (Moës et al. 2002). Next section is a review of traction-separation laws.

2.4 Cohesive Zone Model

Traction-separation laws are widely used to idealize the interaction between two adjacent laminas after delamination. These constitutive laws represent the relationship between stress and the displacement of the adjacent plies. Barenblatt (1959) remarked that, during the crack opening process, substantial interaction forces attract one side of the crack to the other, until it reaches an interatomic distance for which there is no attraction. In addition, at a critical distance, the interaction between each side of the crack reaches a peak value whose magnitude is proportional to the Young's modulus, as is illustrated in Figure 24.

Figure 24 - Interaction forces in function of the distance between the fracture surfaces

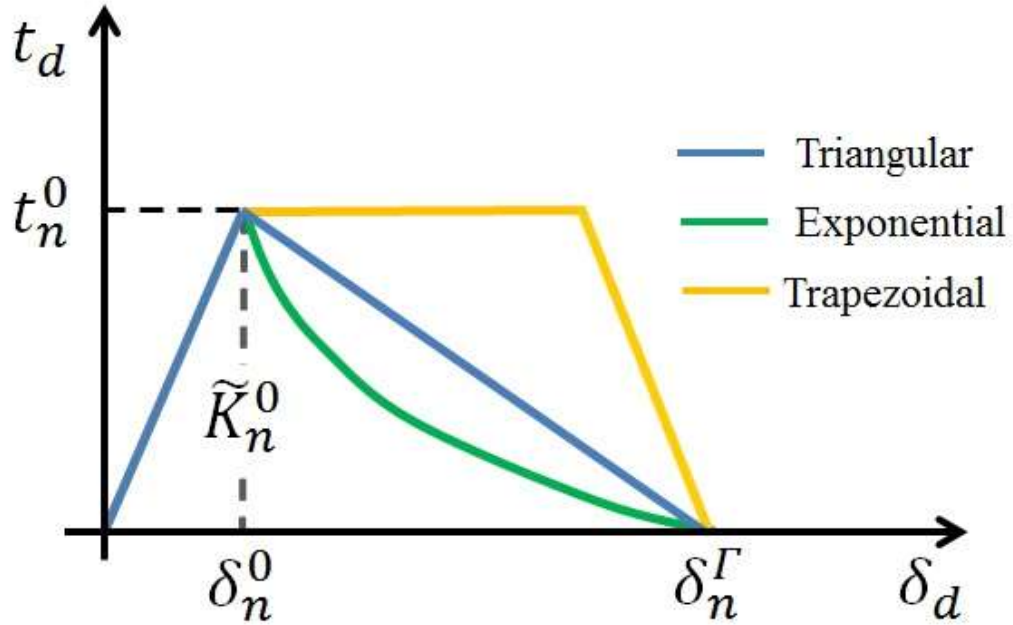


Source: Modified from Barenblatt (1959).

There are many researchers that investigate the relation of Figure 24 through experiments. Usually what is desired is to establish a numerical traction-separation law validated by laboratory procedures. Some ordinary traction-separation laws displayed in Figure 25 are the triangular, exponential and trapezoidal, where δ_n^0 is the critical displacement; \tilde{K}_n^0 is the undamaged interlaminar stiffness (also called cohesive penalty or dummy stiffness); δ_n^Γ is the maximum displacement; t_n^0 is the stress that triggers the delamination failure, also named nominal, max or critical stress.

The Cohesive Zone Model uses the traction separation laws of Figure 25 to numerically simulate delamination via finite elements. Campilho et al. (2013) tested the different shapes of traction-separation laws and concluded that some shapes converge better to specific materials. For instance, the results of the trapezoidal law approximates better the to single-lap joints with ductile adhesive, whereas triangular laws are more accurate for brittle adhesives

Figure 25 - Examples of triangular, exponential and trapezoidal traction-separation laws



Source: Author.

The great advantage of the CZM approach is the fact that it dispenses remeshing as the crack advances, because the interface which delamination is expected to grow are modelled using cohesive elements. These cohesive elements are not linear elastic, but follow a prescribed relation ruled by the traction-separation law (Pascoe et al., 2013). In Figure 25 is notable that the interlaminar stiffness reduces as the separation starts at the critical displacement δ_n^0 . Hence the constitutive behavior of the cohesive element is generally defined as stated in equation .

$$\begin{aligned}
 t_d &= \tilde{K}_n^0 \delta_d \quad \text{if } 0 < \delta_d \leq \delta_n^0 \\
 t_d &= (1 - D_d) \tilde{K}_n^0 \delta_d \quad \text{if } \delta_n^0 < \delta_d \leq \delta_n^\Gamma \quad (27) \\
 t_d &= 0 \quad \text{if } \delta_d > \delta_n^\Gamma
 \end{aligned}$$

where δ_d is the value of relative displacement of the cohesive element, D_d is the damage

parameter, and t_d is the traction. Note that the damage begins at the critical relative displacement of δ_n^0 , already shown in Figure 25.

Based in the formulation developed by Barenblatt (1959), Needleman (1987) and Needleman (1990) investigated decohesion problems using CZM, and later, Hutchinson and Evans (2000) have written a succinct overview of those studies. Roe and Siegmund (2003) proposed a formulation based on irreversible stiffness reduction to model delamination growth. Pascoe et al. (2013) also reviewed the latest CZM formulations.

To propagate the crack using CZM, a crack propagation criterion is required, usually based on a the stress/strain, crack opening displacement, or the strain energy release rate. Wu and Reuter (1965) have proposed a mixed-mode crack propagation criterion for orthotropic materials, known as *The Power Law* expressed in equation (28), which is successfully predicts the progressive failure in thermoplastics PEEK matrix composites for $\beta = 1$.

$$\left(\frac{G_I}{G_{IC}}\right)^\beta + \left(\frac{G_{II}}{G_{IIC}}\right)^\beta = 1 \quad (28)$$

where G_I and G_{II} are the strain energy release rate related to modes I and II respectively, and G_{IC} and G_{IIC} are the critical strain energy release rate respectively, which are critical levels of strain energy dissipated that causes the crack to progress.

Later, Kenane and Benzeggagh (1997) have developed a mixed mode delamination criterion named as *B-K criterion*; their formulation accounts the interaction between mode I and II fracture and a parameter based in different mode ratio obtained by experimental testing. Basically the *The Power Law* and the *B-K criterion* are criteria commonly employed in many CAE softwares.

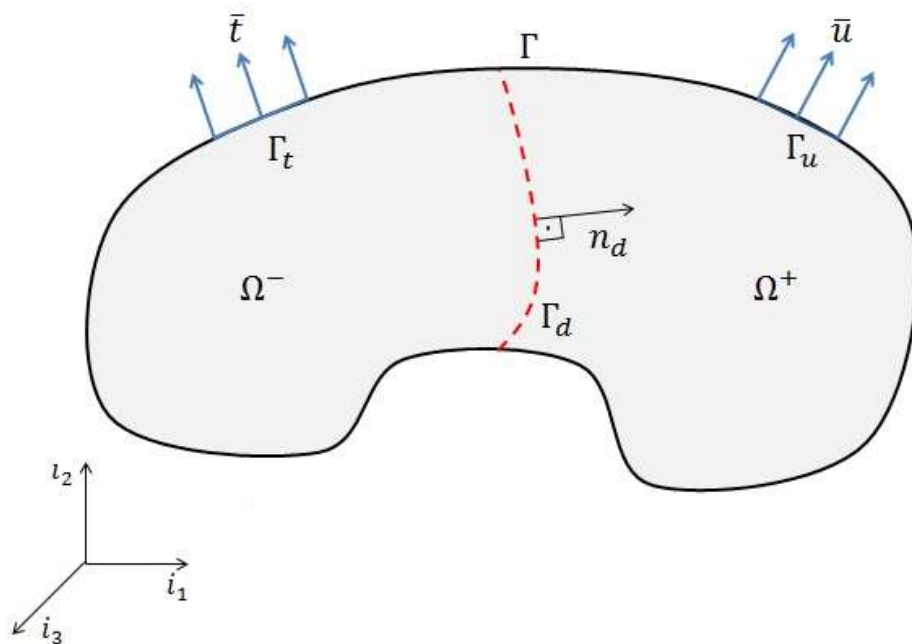
According to Pascoe et al. (2013), the major disadvantage of the CZM is that the formulation is purely numerical and does not satisfy the physical phenomena involved in delamination growth. For instance, the dummy stiffness, is define for numerical reasons only

3 GOVERNING EQUATION

3.1 Kinematic relation

Consider the domain Ω with an external boundary Γ and a discontinuity whose domain is Γ_d , as illustrated in Figure 26. The crack splits the domain into two subdomains: Ω^+ and Ω^- . The external prescribed load and displacement \bar{t} and \bar{u} are imposed in the boundaries Γ_t and Γ_u respectively, and n_d is the unitarian vector normal to the discontinuity

Figure 26 - Domain Ω crossed by a discontinuity at the boundary Γ_d



Source: Author.

The total displacement u is a combination of a regular displacement field \hat{u} and a continuous additional displacement field \tilde{u} (Wells; Sluys, 2001), as demonstrated in equation (29).

$$u(x,t) = \hat{u}(x,t) + f_{\Gamma_d}(x)\tilde{u}(x,t) \quad (29)$$

where x is the position of the material point in the domain Ω expressed in the Cartesian coordinate system, t is time and f_{Γ_d} is the function associated to the strong discontinuities. Supposing linear compatibility, the strain field of equation (30) is derived by differentiating the displacement field.

$$\varepsilon(x,t) = \nabla\hat{u}(x,t) + \nabla\left[f_{\Gamma_d}(x)\tilde{u}(x,t)\right] \quad (30)$$

Remmers in 2006 proposes the Heaviside function to model the strong discontinuity at the crack domain, and states the following “since the jump function is not uniquely defined at the discontinuity, the corresponding strain field is unbounded.” Mathematically, this implies that the function f_{Γ_d} can be considered as constant, thus equation (31) is valid.

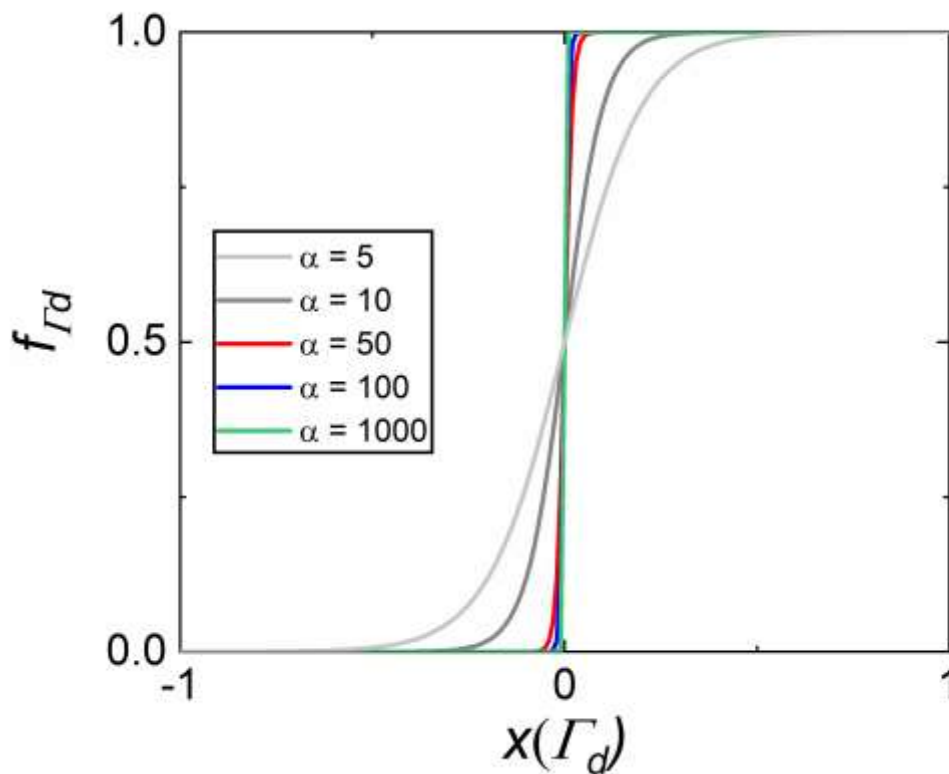
$$\nabla\left[f_{\Gamma_d}(x)\tilde{u}(x,t)\right] = f_{\Gamma_d}(x)\nabla\tilde{u}(x,t) \quad (31)$$

Zhu (2012) has suggested the jump function to have a fixed value at the discontinuity coordinate to eliminate the unbounding strain field, such as $\frac{1}{2}$ for instance. Here the strong discontinuity function is not the Heaviside. Instead, a new hyperbolic function is proposed whose formulation described in equation (32).

$$f_{\Gamma_d}(x) = \frac{\text{Tanh}(\alpha x) + 1}{2} ; \alpha \geq 5 \quad (32)$$

where α is a numeric parameter which adjust the smoothness of the function. The higher the value of α , the more steep the step the function is (note that α must be higher than 5). The effect of different values of α is demonstrated in Figure 27, not that for $\alpha = 100$ and $\alpha = 1000$ the curves are practically overlapped to each other.

Figure 27 - Hyperbolic tangent function used to model strong discontinuity



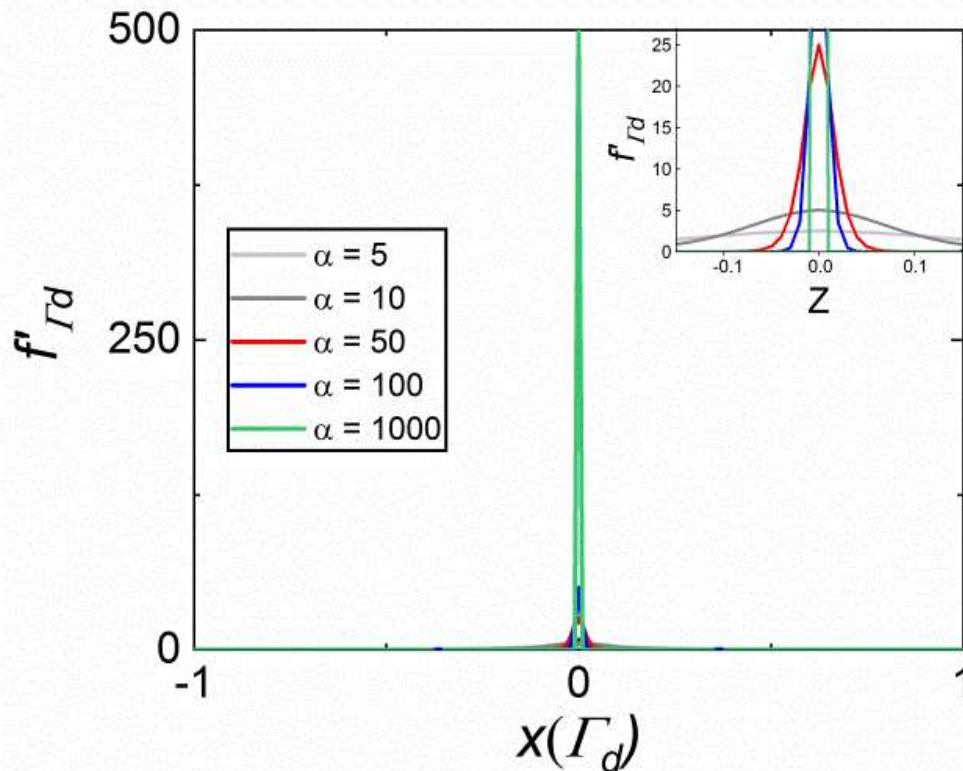
Source: Author.

The derivative of equation (32) is expressed in equation (33) and plotted in Figure 28. Note the similarity to the pulse function, defined as Dirac delta. This time, the numeric parameter α influences the smoothness of the derivative of the hyperbolic tangent function,

and also on the peak value, which is always $\alpha/2$. Note that the proposed function becomes more similar to the Heaviside when α is sufficient large.

$$\frac{\partial f_{\Gamma_d}(x)}{\partial x} = \frac{\alpha}{2} \text{Sech}^2(\alpha x) \quad (33)$$

Figure 28 - Differentiation of the hyperbolic tangent function, with zoom near $x=0$



Source: Author.

At the crack coordinate the Dirac delta function equals infinite, which is actually a drawback when is needed to perform numerical integration. Conversely, the hyperbolic tangent function presented here, and its derivative, are continuous; therefore, they are defined in the whole domain of the discontinuity.

Since the function that models the strong discontinuity is now defined at the crack coordinate, equation (31) is not mathematically correct anymore. It is required to apply the product rule as demonstrated in equation (34).

$$\begin{aligned} \nabla \left[f_{\Gamma_d}(x) \tilde{u}(x,t) \right] &= \nabla f_{\Gamma_d}(x) \tilde{u}(x,t) + \\ f_{\Gamma_d}(x) \nabla \tilde{u}(x,t) \end{aligned} \quad (34)$$

3.2 Equilibrium equations

The equilibrium of the body in the absence of body forces, as well as the equilibrium at boundary conditions, can be expressed as equation (35).

$$\begin{aligned} \nabla \cdot \sigma &= 0 \quad ; \quad x \in \Omega \\ n_t \cdot \sigma &= \bar{t} \quad ; \quad x \in \Gamma_t \\ u &= \bar{u} \quad ; \quad x \in \Gamma_u \end{aligned} \quad (35)$$

where σ is the Cauchy stress, \bar{t} is the prescribed traction at the external boundary condition Γ_t with outward normal vector n_t , and \bar{u} are the prescribed displacement at the external boundary condition Γ_u .

At the internal boundary condition Γ_d , the following equilibrium equation (36) can be inserted.

$$n_d \cdot \sigma = t_d \quad ; \quad x \in \Gamma_d \quad (36)$$

where t_d is the tractions at the internal boundary Γ_d whose normal vector n_d points to Ω^+ . The equilibrium equation can be expressed in weak form by evoking the variational displacement field, as demonstrated in equation (37).

$$\int_{\Omega} \delta u (\nabla \cdot \sigma) d\Omega = 0 \quad \forall \delta u \quad (37)$$

The variational displacement field can also be expressed in terms of a combination of a regular displacement theory and an additional field as stated in equation (38).

$$\delta u(x, t) = \delta \hat{u}(x, t) + \delta(f_{\Gamma_d}(x) \tilde{u}(x, t)) \quad (38)$$

Substituting equation (38) in (37) results in the following equation (39).

$$\int_{\Omega} \delta \hat{u} (\nabla \cdot \sigma) d\Omega + \int_{\Omega} \delta(f_{\Gamma_d} \tilde{u}) (\nabla \cdot \sigma) d\Omega = 0 \quad (39)$$

Finally, the weak form of the problem proposed in equation (40) is derived by applying the Divergence theorem, plus using the symmetry of the Cauchy stress tensor, and introducing both internal and external boundary conditions to equation (39).

$$\begin{aligned} & \int_{\Omega} \nabla \delta \hat{u} : \sigma d\Omega + \int_{\Omega} \nabla (f_{\Gamma_d} \delta \tilde{u}) : \sigma d\Omega + \int_{\Gamma_d} f_{\Gamma_d} \delta \tilde{u} \cdot t d\Gamma_d \\ & = \int_{\Gamma_t} \delta \hat{u} \cdot \bar{t} d\Gamma_t + \int_{\Gamma_t} f_{\Gamma_d} \delta \tilde{u} \cdot \bar{t} d\Gamma_t \end{aligned} \quad (40)$$

where the first term of the left-hand side of equation (40) refers to the internal energy of the body due to regular displacement field, whereas the second term is the energy associated to the additional displacement field. The third term is the energy related to the cohesive zone (internal boundary Γ_d). The right hand side of equation (40) are the energy of the prescribed load on the external boundary condition Γ_t .

3.3 Constitutive relations

3.3.1 Constitutive law for orthotropic materials

The relation between stresses and strains of the lamina follows the classical form of Hooke's law to orthotropic materials, which is demonstrated in equations (41) to (43).

$$\begin{Bmatrix} \sigma_{xx} \\ \sigma_{yy} \\ \tau_{xy} \\ \tau_{xz} \\ \tau_{yz} \\ \sigma_{zz} \end{Bmatrix}^{(k)} = \begin{bmatrix} \tilde{C}_{11} & \tilde{C}_{12} & \tilde{C}_{16} & 0 & 0 & \tilde{C}_{13} \\ \tilde{C}_{12} & \tilde{C}_{22} & \tilde{C}_{26} & 0 & 0 & \tilde{C}_{23} \\ \tilde{C}_{16} & \tilde{C}_{26} & \tilde{C}_{66} & 0 & 0 & \tilde{C}_{36} \\ 0 & 0 & 0 & \tilde{C}_{55} & \tilde{C}_{45} & 0 \\ 0 & 0 & 0 & \tilde{C}_{45} & \tilde{C}_{44} & 0 \\ \tilde{C}_{13} & \tilde{C}_{23} & \tilde{C}_{36} & 0 & 0 & \tilde{C}_{33} \end{bmatrix}^{(k)} \begin{Bmatrix} \varepsilon_{xx} \\ \varepsilon_{yy} \\ \gamma_{xy} \\ \gamma_{xz} \\ \gamma_{yz} \\ \varepsilon_{zz} \end{Bmatrix}^{(k)} \quad (41)$$

Note that the constitutive relation of equation (41) refers to the global system. To correlate the local lamina system to the global laminate system, equations (42) and (43) should be applied.

$$\begin{aligned}
\tilde{C}_{11} &= C^4 \bar{C}_{11} + 2S^2 C^2 \bar{C}_{12} + S^4 \bar{C}_{22} + 4S^2 C^2 \bar{C}_{66} ; \\
\tilde{C}_{12} &= S^2 C^2 \bar{C}_{11} + (S^4 + C^4) \bar{C}_{12} + S^2 C^2 \bar{C}_{22} - 4S^2 C^2 \bar{C}_{66} ; \\
\tilde{C}_{16} &= SC^3 \bar{C}_{11} + (S^3 C - SC^3) \bar{C}_{12} - S^3 C \bar{C}_{22} + 2(S^3 C - SC^3) \bar{C}_{66} ; \\
\tilde{C}_{13} &= C^2 \bar{C}_{13} + S^2 \bar{C}_{23} ; \\
\tilde{C}_{22} &= S^4 \bar{C}_{11} + 2S^2 C^2 \bar{C}_{12} + C^4 \bar{C}_{22} + 4S^2 C^2 \bar{C}_{66} ; \\
\tilde{C}_{26} &= S^3 C \bar{C}_{11} + (SC^3 - S^3 C) \bar{C}_{12} - SC^3 \bar{C}_{22} + 2(SC^3 - S^3 C) \bar{C}_{66} ; \\
\tilde{C}_{23} &= S^2 \bar{C}_{13} + C^2 \bar{C}_{23} ; \\
\tilde{C}_{66} &= S^2 C^2 \bar{C}_{11} - S^2 C^2 \bar{C}_{12} + S^2 C^2 \bar{C}_{22} + (C^4 + S^4 + 2C^2 S^2) \bar{C}_{66} ; \quad (42) \\
\tilde{C}_{36} &= SC \bar{C}_{13} - SC \bar{C}_{23} ; \\
\tilde{C}_{55} &= C^2 \bar{C}_{55} + S^2 \bar{C}_{44} ; \\
\tilde{C}_{45} &= SC \bar{C}_{55} - SC \bar{C}_{44} ; \\
\tilde{C}_{44} &= S^2 \bar{C}_{55} + C^2 \bar{C}_{44} ; \\
\tilde{C}_{33} &= \bar{C}_{33} ;
\end{aligned}$$

$$C = \cos(\theta) ;$$

$$S = \sin(\theta)$$

where the angle θ refers to the orientation of the fibers of the k -th layer.

$$\begin{aligned}
\bar{C}_{11} &= \frac{1 - \nu_{23} \nu_{32}}{\Delta} E_{11} \quad ; \quad \bar{C}_{12} = \frac{\nu_{21} + \nu_{23} \nu_{31}}{\Delta} E_{11} ; \\
\bar{C}_{22} &= \frac{1 - \nu_{13} \nu_{31}}{\Delta} E_{22} \quad ; \quad \bar{C}_{13} = \frac{\nu_{21} \nu_{32} + \nu_{31}}{\Delta} E_{11} ; \\
\bar{C}_{23} &= \frac{\nu_{32} + \nu_{12} \nu_{31}}{\Delta} E_{22} \quad ; \quad \bar{C}_{33} = \frac{1 - \nu_{12} \nu_{21}}{\Delta} E_{33} ; \quad (43) \\
\bar{C}_{44} &= G_{23} \quad ; \quad \bar{C}_{55} = G_{13} \quad ; \quad \bar{C}_{66} = G_{12} ; \\
\Delta &= 1 - (\nu_{23} \nu_{32} + \nu_{12} \nu_{21} + \nu_{13} \nu_{31} - 2\nu_{21} \nu_{32} \nu_{13}) ; \\
E_{ij} \nu_{ji} &= E_{jj} \nu_{ij} \quad \forall \quad i, j = 1, 2, 3
\end{aligned}$$

The internal energy term of the governing equation may be written as in equation (44).

$$\begin{aligned}
\delta \varepsilon_{ij} \sigma_{ij} = & \delta \varepsilon_{xx} \left(\tilde{C}_{11} \varepsilon_{xx} + \tilde{C}_{12} \varepsilon_{yy} + \tilde{C}_{16} \gamma_{xy} + \tilde{C}_{13} \varepsilon_{zz} \right) + \\
& \delta \gamma_{xy} \left(\tilde{C}_{16} \varepsilon_{xx} + \tilde{C}_{26} \varepsilon_{yy} + \tilde{C}_{66} \gamma_{xy} + \tilde{C}_{36} \varepsilon_{zz} \right) + \\
& \delta \gamma_{xz} \left(\tilde{C}_{55} \gamma_{xz} + \tilde{C}_{45} \gamma_{yz} \right) + \\
& \delta \varepsilon_{yy} \left(\tilde{C}_{12} \varepsilon_{xx} + \tilde{C}_{22} \varepsilon_{yy} + \tilde{C}_{16} \gamma_{xy} + \tilde{C}_{23} \varepsilon_{zz} \right) + \\
& \delta \gamma_{yz} \left(\tilde{C}_{45} \gamma_{xz} + \tilde{C}_{44} \gamma_{yz} \right) + \\
& \delta \varepsilon_{zz} \left(\tilde{C}_{13} \varepsilon_{xx} + \tilde{C}_{23} \varepsilon_{yy} + \tilde{C}_{36} \gamma_{xy} + \tilde{C}_{33} \varepsilon_{zz} \right)
\end{aligned} \tag{44}$$

3.3.2 The constitutive law of the cohesive zone

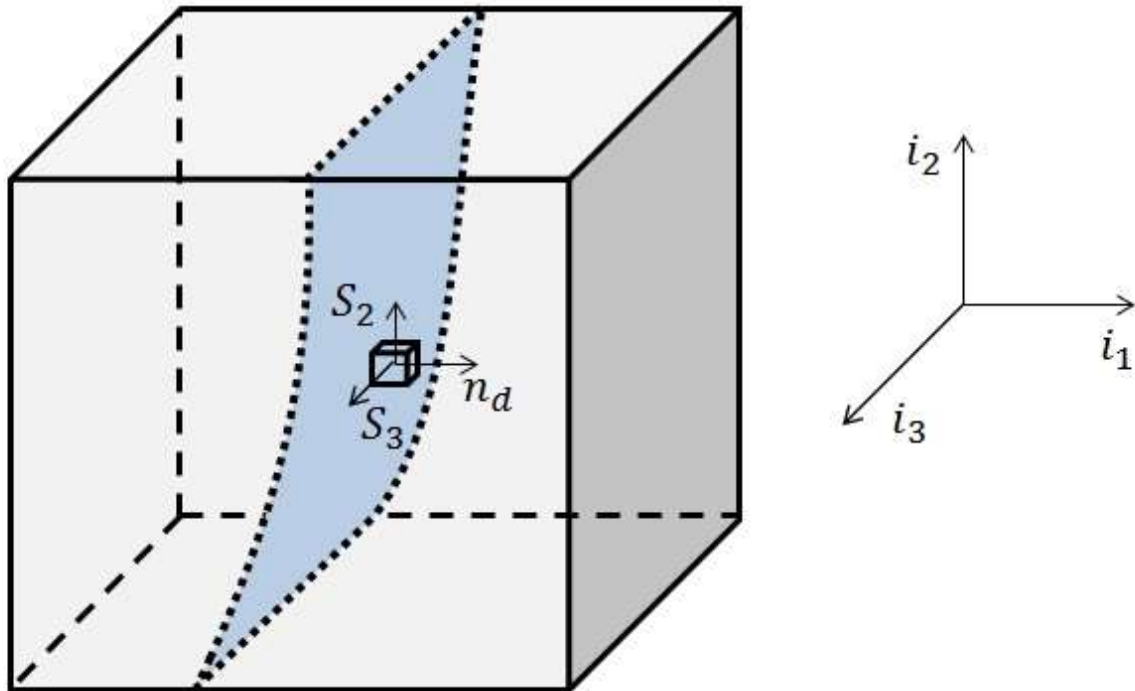
The interaction of the cohesive planes is defined by an independent constitutive relation which characterizes the fracture process of the structure. Rigorously speaking, the Cohesive surface can be interpreted as a discontinuity in the displacement field to the body Remmers (2006). It is required to define the stress/strain relation of this surface element. Usually, this constitutive relation is described in terms of interlaminar stress t_d and the gap between laminas δ_d , already stated in equation (27). The tractions and the displacement can also be decomposed as follows in equation (45).

$$\begin{aligned}
t_d &= t_n n_d + t_{s_2} n_{s_2} + t_{s_3} n_{s_3} \\
\delta_d &= \delta_n n_d + \delta_{s_2} n_{s_2} + \delta_{s_3} n_{s_3}
\end{aligned} \tag{45}$$

where t_n and δ_n are the normal traction and normal separation acting in the cohesive element, and (t_{s_2}, t_{s_3}) and $(\delta_{s_2}, \delta_{s_3})$ are the traction and separation components in respect to

the shear planes whose normal vector are n_{s_2} and n_{s_3} . Figure 29 illustrates the orientation of the discontinuity.

Figure 29 - Orientation of the discontinuity



Source: Author.

This dissertation proposes a formulation to delamination in pure mode I, thus the only component considered of equation (45) is the normal component.

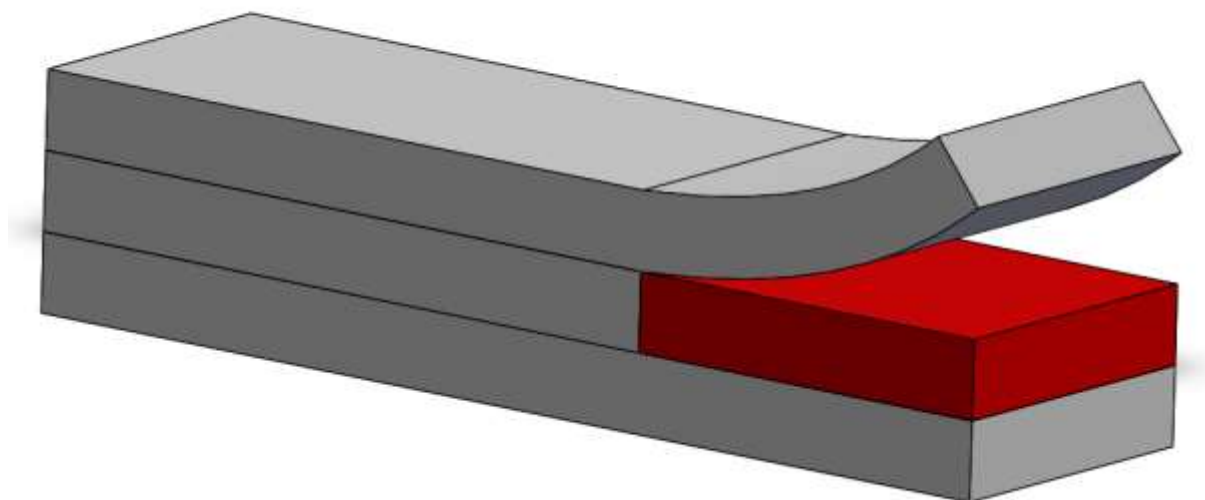
Note that the mathematical problem of equation (40) should be treated as non-linear because of the damage parameter D_d applied to the dummy stiffness (equation (27)) depends on the separation between two adjacent laminas. Hence, it is essential to solve this problem with non-linear techniques, such as Newton-Rhapson method or the Secant method. Next is demonstrated how to solve the governing equation via the mathematical formulation proposed here.

4 EXTENDED LAYERWISE FINITE ELEMENT FORMULATION

The governing equation stated before is solved through the finite elements approach, in which the displacement field is based on the layerwise theory and the delamination is modeled via XFEM strong enrichments.

The advantage of working with XFEM is that the formulation is an extension of the standard finite element procedures. Only the enriched elements are affected; all others elements remain with the same formulation of usual FEM (Mohammadi, 2008). In this dissertation, because of the layerwise theory, the affected displacement field will be those of the lamina whose elements are in the delamination domain. The leap over the displacement field, however, is employed only in one of the two adjacent laminas of the delamination. For instance, take the delamination case presented in Figure 30. The enriched elements are those painted red.

Figure 30 - Illustration of enriched elements in the formulation proposed



Source: Author.

Each node has $4(n + 1)$ degrees of freedom, where n is the number of laminas. The vector of nodal parameters a_j is presented in equation (46).

$$a_j = \left[u_1^1 u_2^1 u_3^1 \lambda^1 \cdots u_1^{k+1} u_2^{k+1} u_3^{k+1} \lambda^{k+1} \right]_j^T \quad (46)$$

where the subscripts 1, 2 and 3 are the displacement on each direction whereas 4 is the extra degree of freedom associated to the strong discontinuity (if any); the superscript k is the number of the lamina.

4.1 Discrete displacement field

According to the layerwise theory, the discretization of the displacement field can be approached in two different ways. One alternative is to describe the displacement field of the element of the lamina, and the other is to define the displacement field of the element of the laminate. The first results in a more compact equation, but, when computing the elementary stiffness matrices, it is necessary to perform an assemble over thickness to determine the stiffness of an element. If the displacement field of the element is already described, one can directly assemble all stiffness matrices of the elements in order to calculate the global stiffness matrix, but the numerical approximation has more indexes. The approach considered here is to describe the displacement field of a single lamina and is demonstrated in the following equation (47).

$$u_i^k(x, y, z) = \sum_{j=1}^{NN} \sum_{k=1}^L N_j(x, y) \phi_k(z) u_i^{jk} + \delta_{3i} \sum_{r=1}^S \sum_{k=1}^L N_r(x, y) Th_k(z) \phi_k(z) \lambda_r^k \quad (47)$$

where $i = 1, 2, 3$; N_j are the in-plane shape function and ϕ_k are the layerwise functions of the k th lamina; $Th(z)$ is the hyperbolic tangent function discussed previously; L is the number of layerwise functions within a lamina; N is the number of nodes in the element; S is the number of strong enriched nodes of the element; and δ_{3i} is the Kronecker delta, that causes the additional displacement field to be accounted only in the thickness direction. Note that the notation of the displacement field has a superscript k indicated the layerwise function.

The continuum displacement field idealized in equation (29) can be associated to the approximated displacement field of equation (47) as demonstrated in equation (48). Note that the degree of freedom associated to the strong enrichment gained the superscript k to indicate the layerwise function of the lamina

$$\begin{aligned} \hat{u}(x, t) &= \sum_{j=1}^{NN} \sum_{k=1}^L N_j(x, y) \phi_k(z) u_i^{jk} \quad ; \\ f_{\Gamma_d} \tilde{u}(x, t) &= \sum_{r=1}^S \sum_{k=1}^L N_r(x, y) Th_k \phi_k(z) \lambda_r^k \end{aligned} \quad (48)$$

4.2 Discrete strain field

The compatibility relation considered here is the linear strain-displacement relation, written in equation (49) (Chen; Saleeb, 1982).

$$\varepsilon_{ij} = \frac{1}{2} (u_{i,j} + u_{j,i}) \quad (49)$$

Applying equation (49) to the discrete displacement field, and the symmetry of the strain tensor stated in equation (50) result in the strain field displacement shown in equation (51) (Chen; Saleeb, 1994).

$$\varepsilon_{ij} = \varepsilon_{ji} \quad (50)$$

$$\begin{aligned} \varepsilon_{ii}^{jk} &= N_{j,i} \sum_{k=1}^L \phi_k u_i^{jk} \quad ; \quad i=1,2; \\ \varepsilon_{33}^{jk} &= N_j \sum_{k=1}^L \phi_{k,3} u_3^{jk} + N_j \sum_{k=1}^L (Th_k \phi_k)_{,3} \lambda_j^k; \\ \gamma_{12}^{jk} &= N_{j,2} \sum_{k=1}^L \phi_k u_1^{jk} + N_{j,1} \sum_{k=1}^L \phi_k u_2^{jk}; \\ \gamma_{i3}^{jk} &= N_j \sum_{k=1}^L \phi_{k,3} u_i^{jk} + N_{j,i} \left(\sum_{k=1}^L \phi_k u_3^{jk} + \sum_{k=1}^L Th_k \phi_k \lambda_j^k \right) \quad ; \quad i=1,2 \end{aligned} \quad (51)$$

The strain-displacement relation can be expressed as shown in equation (52). Note that the superscripts k and j specifies the layer and the node, and the vector of nodal parameters is the same of equation (46), but shortened to the particular degrees of freedom of the k -th layer.

$$\varepsilon_{pq}^{jk} = B_{pm}^{jk} a_m^{jk} \quad (52)$$

Where the term B_{pm}^{jk} in matrix form is shown in equation (53), where the s is the index of the layerwise function within the layer. Note that the first three columns are associated to the regular degrees of freedom of FEM whereas the fourth is related to the strong enrichment. To determine the B matrix of the lamina, one needs to assemble all indexes of the layerwise functions (s index) as is demonstrated in equation (54).

$$[B]^{jks} = \begin{bmatrix} N_{j,1}\phi_s & 0 & 0 & 0 \\ 0 & N_{j,2}\phi_s & 0 & 0 \\ N_{j,2}\phi_s & N_{j,1}\phi_s & 0 & 0 \\ N_j\phi_{s,3} & 0 & N_{j,1}\phi_s & N_{j,1}\phi_s Th_s \\ 0 & N_j\phi_{s,3} & N_{j,2}\phi_s & N_{j,2}\phi_s Th_s \\ 0 & 0 & N_j\phi_{s,3} & N_j(\phi_s Th_s)_{,3} \end{bmatrix}^{jks} \quad (53)$$

$$[B]^{jk} = [B^1 B^2 \dots B^{(L-1)} B^L]^{jk} \quad (54)$$

Analogically, the B matrix of the j -th node of an element is demonstrated in equation (55):

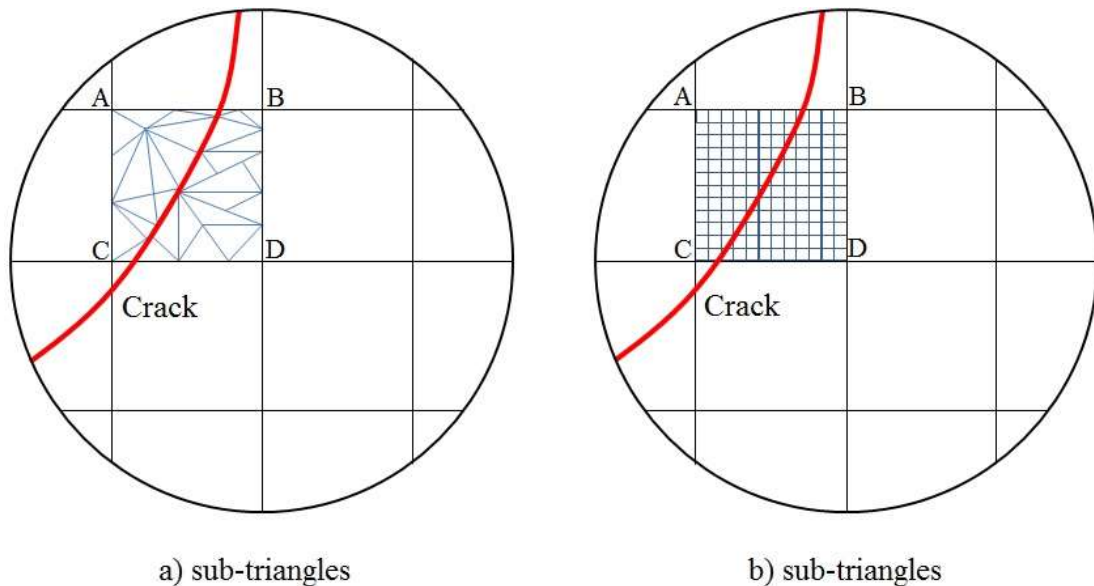
$$B^j = [B^1 B^2 \dots B^{(L^*-1)} B^{L^*}]^j \quad (55)$$

where L^* is the number of laminas of the laminate. The same logic applies to determine the B matrix of the element. The weak form of the problem stated in equation (40) is numerically approximated according to equation (56), Note the B matrix in this formula is related to the k -th lamina, which means that the assemble of equation (54) has already been done

$$\begin{aligned} & \left[\sum_{k=1}^{L^*} \int_{\Omega} \int_{z_{bot}}^{z_{top}} B_{ji}^k \bar{C}_{jm}^k B_{mn}^k dz d\Omega + \int_{\Gamma_d} (N_i Th_m \phi_m) (K_j N_j Th_n \phi_n) d\Gamma_d \right] \hat{U}_n \\ & = \int_{\Gamma_t} (N_i \phi_m) \bar{t} d\Gamma_t + \int_{\Gamma_t} Th_m (N_i \phi_m) \bar{t} d\Gamma_t \end{aligned} \quad (56)$$

where \bar{C}_{jm}^k is the constitutive matrix of the k th layer oriented on the global coordinate system introduced in equation (41). The integrands z_{bot} and z_{top} of equation (56) are the coordinates of the bottom and the top planes of the k -th lamina. Note that the first term of the left side accounts for both energies of the regular and additional displacement field, which is different from equation (40) presented before. Equation (56) can be solved numerically through Gauss quadrature. For polynomial integrands, the Gauss integration is proved to be exact, but it may result in a substantial error for non-polynomials. The introduction of discontinuities results on highly nonlinear fields, thus it is required an efficient approach to proceed non-linear analyses with Gauss Quadrature with enriched elements. Moës et al. (1999) propose two strategies to overcome this inconvenience. The first method is to subdivide the element at both sides of the crack into triangles, and the second is to divide the element into sub-squads. Both ways are based on refinement near the discontinuity, and they are illustrated in Figure 31.

Figure 31 - The two methods proposed by Moës et al. (1999) to overcome the numerical integration spurious via Gauss quadrature on enriched elements



Modified from: (Mohammadi, 2008).

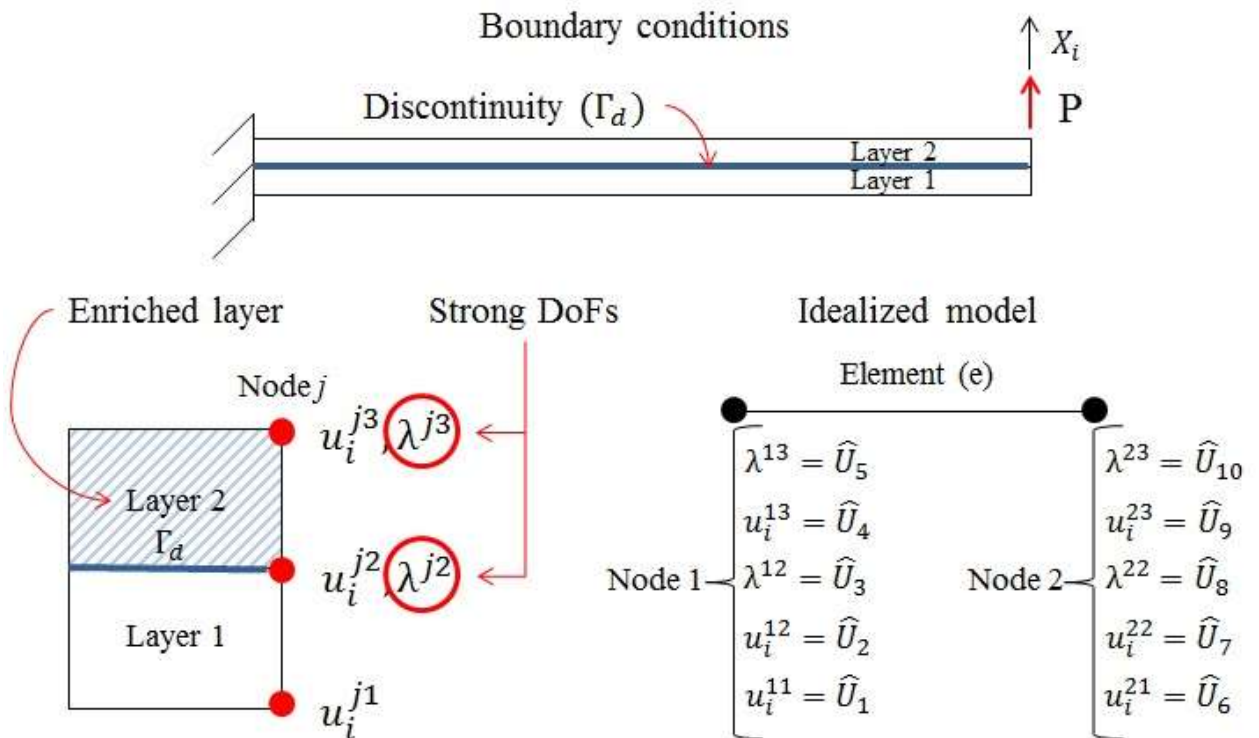
The method used here to deal with the numerical integration spurious is to perform traditional refinement and to increase the number of Gauss points in the thickness direction. The code is programmed in MATLAB[®], which is an easy tool to deal with finite elements.

However, it demands more RAM to run routines when compared to Fortran or C+.

To illustrate how to approach a strong discontinuity with the formulation proposed, considerer the case of Figure 32, a two-layered beam under mode I with a discontinuity between the two layers over the domain Γ_d . This case is similar to the 1D element presented in Figure 16, the only difference is the presence the strong discontinuity and the direction of the external load. This problem introduced is also 1D; the beam has been drawn with two layers in below the boundary conditions only to emphasize the location of the strong discontinuity.

Due the fact that the strong discontinuity in Figure 32 is between the two layers, it could be discretized in one of the both layers. If it is discretized in *Layer 1*, the coordinate of the crack in the iso parametric system would be $\zeta = +1$, and $\zeta = -1$ in case if it is introduced to the *Layer 2*. Observe that the discontinuity has been discretized in the *Layer 2* to this problem, thus the extra DoFs associated to the strong discontinuity are introduced to the second layer (variables λ^{j2} and λ^{j3}).

Figure 32 - Illustrative case of a two-layer beam under mode I via the formulation proposed

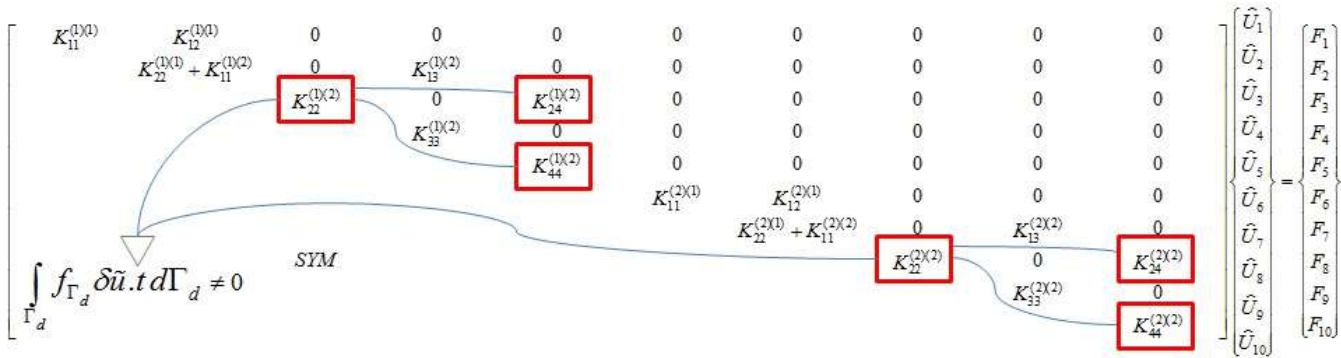


Source: Author.

Observe that the problem presented without discontinuity in Figure 16 had less unknowns (six unknowns) when compared to the case with discontinuity of Figure 32 (ten unknowns). Thus, introducing discontinuities can increase the number of degrees of freedom significantly.

The mesh of the case of Figure 32 has only one element. Although is not possible to approach this problem with a single element, it would be inappropriate to refine the mesh because the linear system would be too large to demonstrate here. The linear system is presented in Figure 33. The highlighted indexes of the global stiffness matrix are the indexes related to the strong discontinuity. Hence, the third term of the weak form presented in equation (40) is different of zero (the energy associated to the cohesive zone).

Figure 33 - Global linear system of the problem of Figure 32



Source: Author.

The boundaries conditions are inserted the same way as in the problem without discontinuity of Figure 16. Thus the degrees of freedom located at the fixed are all set to zero $\hat{U}_1 = \hat{U}_2 = \hat{U}_3 = \hat{U}_4 = \hat{U}_5 = 0$. Regarding the external load, The force P is inserted in the position F_9 and F_{10} . Note that F_{10} is related to the second term of the right hand side of the weak form of the mathematical problem, presented in equation (40).

To solve the linear system of Figure 33 is necessary to define the traction force acting in the cohesive zone. As already explained, imposing a traction separation law to the constitutive relation of the cohesive elements results in a non-linear. Therefore, to solve the problem is necessary a mathematical procedure such as the Newton-Rhapson method or the Secant Method.

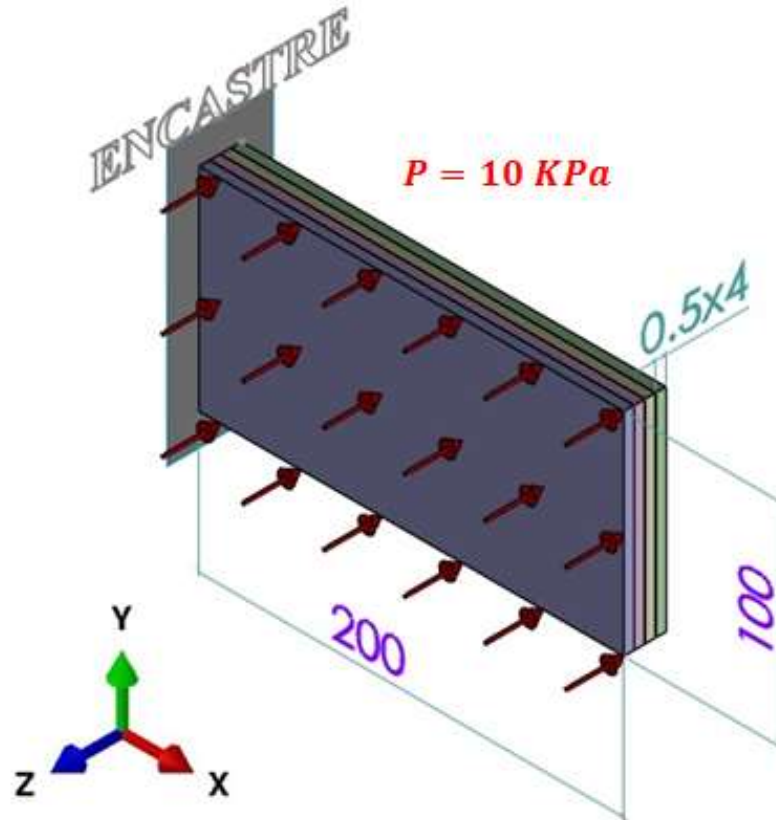
5 NUMERICAL RESULTS

Four numerical examples are presented in this section. The first is a 4-layered undamaged thin composite plate; the second case is a thick beam made of reinforced concrete, also known as deep beam; the third example is a sandwich composite with cubic geometry; the last one is a bending analysis on a pre-delaminated composite beam, solved by Li et al. (2015), in this case the delamination does not progress.

The first numerical example is an undamaged composite plate with one of its smaller edges cantilevered, plus constant load applied to the top surface as is schematically represented in Figure 34 (dimensions in millimeters). Two different stacking sequences are considered in this model: $[0]_4$ and $[0/90]_2$. In addition, the degree of the layerwise interpolation varies from first to third order. To validate this problem, the results are compared to a solid-element analysis done in ABAQUSTM. The primary objective of this first example is to compare the results of several interpolation orders in thickness direction for thin plates.

The elastic properties of the first numerical model are based on Li et al. (2015) written in Table 1. The analyses named LW in Table 1 refer to the layerwise theory, and its following number is the order of the interpolation in the thickness direction (LW1 is linear; LW2 is quadratic, and LW3 is cubic), the element is the rectangular 4-node homogeneous isoparametric element; the SOLID refers to the analysis carried out in ABAQUSTM based in a 20-node solid-element with parabolic interpolation in all directions (terminology of this element in ABAQUSTM software is C3D20).

Figure 34 - Boundary conditions and geometry of the first numerical example (dimensions in millimeters)



Source: Author.

Table 1 – Elastic properties of the lamina of the first numerical model.

E_{11}	E_{22}	E_{33}	G_{12}	G_{13}	G_{23}	ν_{12}	ν_{13}	ν_{23}
(GPa)	(GPa)	(GPa)	(GPa)	(GPa)	(GPa)	(-)	(-)	(-)
181	103	103	7.17	7.17	6.21	0.28	0.02	0.4

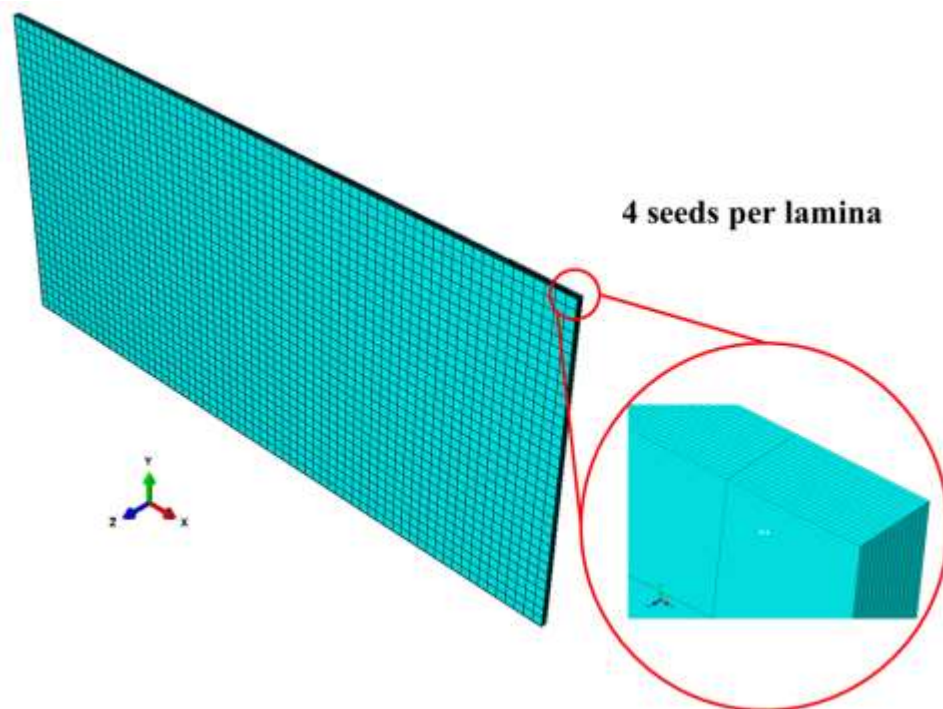
The elements in all analyses have same in-plane dimensions, further information of the mesh are in Table 2.

Table 2 – Information of the mesh of the first numerical model.

Analysis	Elements	Nodes	DoFs	LW order
LW1	5,000	5,151	77,265	1
LW2	5,000	5,151	139,077	2
LW3	5,000	5,151	200,889	3
SOLID	35,334	152,996	458,988	2

The mesh of the LW analyses are composed of quadrilateral elements and one virtual ply to each lamina. The elements of the SOLID analyses are also quadrilateral, and four seeds have been created in the thickness direction to each lamina, as demonstrated in Figure 35.

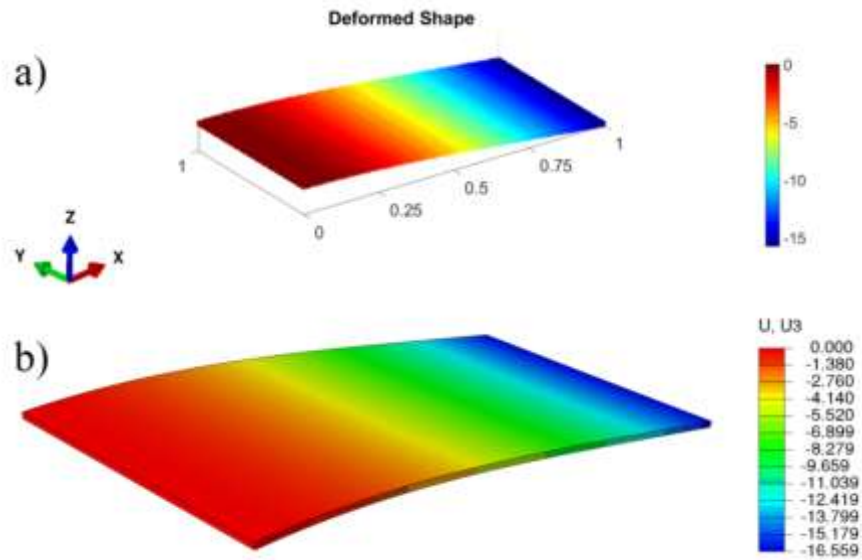
Figure 35 - Mesh discretization of the composite thin laminate numerical example



Source: Author.

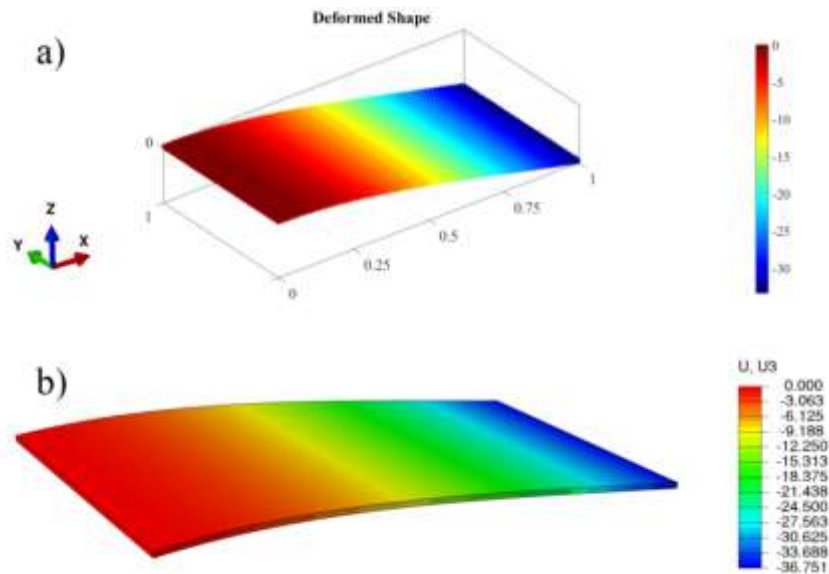
Figure 36 and Figure 37 are the deformed shape of the LW1 and solid analyses .

Figure 36 - The deformed shape of $[0]_4$ laminate of the first numerical example: a) LW1 analysis; b) Solid analysis.



Source: Author.

Figure 37 - The deformed shape of $[0/90]_2$ of the first numerical example of LW1 and SOLID analyses respectively



Source: Author.

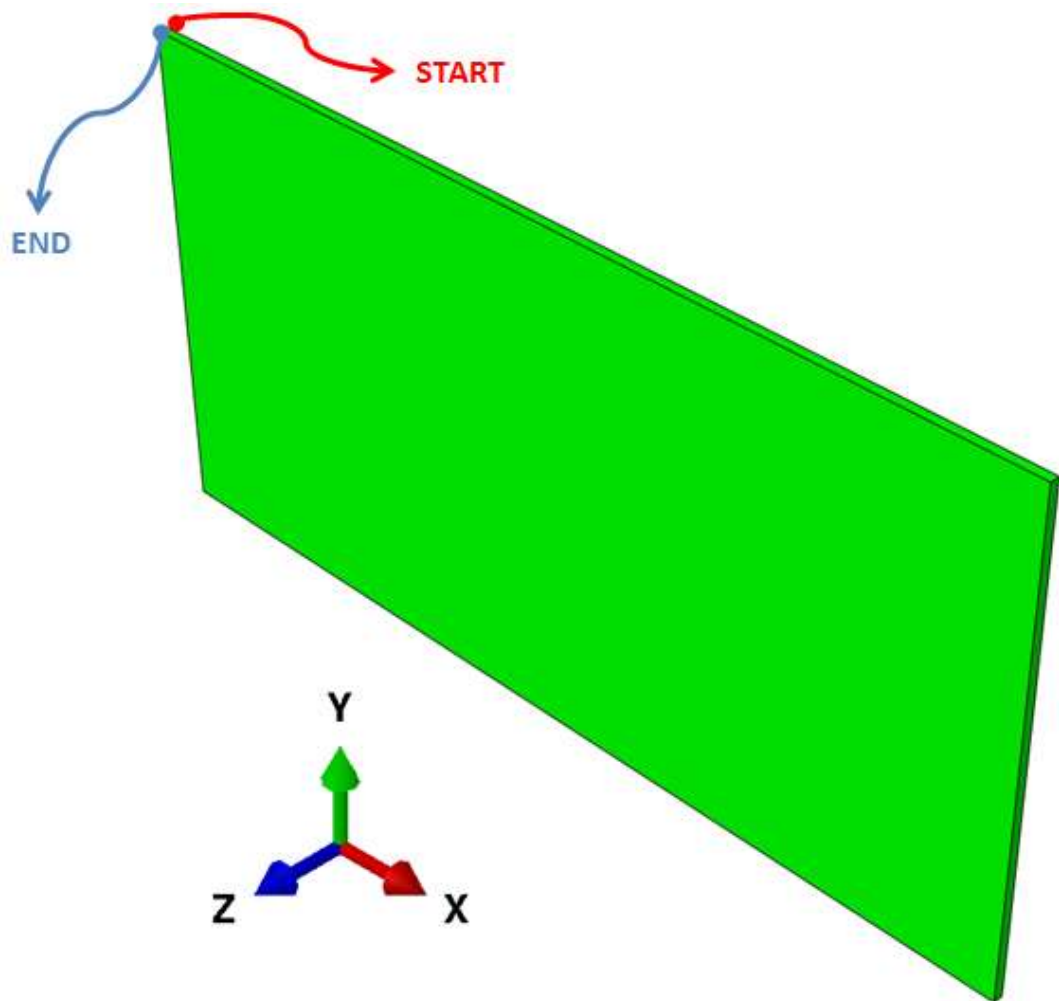
Table 3 shows the maximum displacement on thickness direction of all analyses and its deviation from the SOLID analysis in parenthesis. The order of the interpolation of the layerwise analysis seems to be irrelevant in this case, which can be also explained due to low thickness/length ratio. Therefore, a linear interpolation over the thickness is enough to obtain good results for displacements.

Table 3 - Comparison of results of maximum displacement (in millimeters) of the first numerical example

Orientation	LW1	LW2	LW3	SOLID
[0] ₄	15.771	15.773	15.773	16.559
	(4.76%)	(4.75%)	(4.75%)	(-)
[0/90] ₂	33.343	33.369	33.369	36.751
	(9.27%)	(9.20%)	(9.20%)	(-)

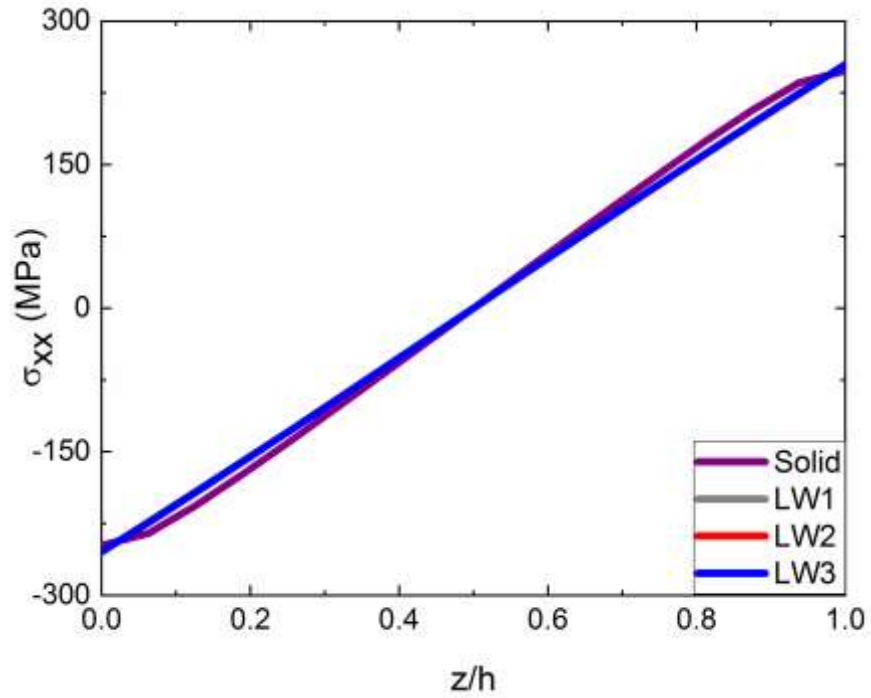
Next, the distribution of normal stresses of the path demonstrated in Figure 38 are presented in Figure 39 to Figure 44.

Figure 38 - Chosen path to compare stress distribution

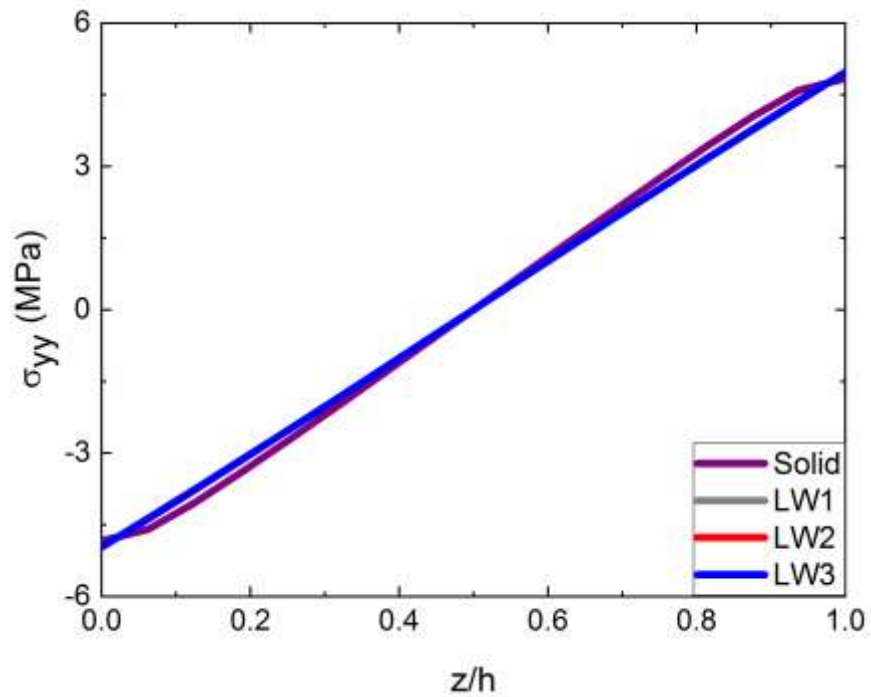


Source: Author.

The distribution of normal stresses in XX and YY directions are shown in Figure 39 and Figure 40 respectively. It is evident the accordance of all analyses. Observe that all layerwise curves overlapped to each other, which means that increasing the polynomial interpolation of the layerwise function has not shown any improvement in the in-plane stress distributions.

Figure 39 - Distribution of stresses in XX direction of the first numerical example of $[0]_4$ 

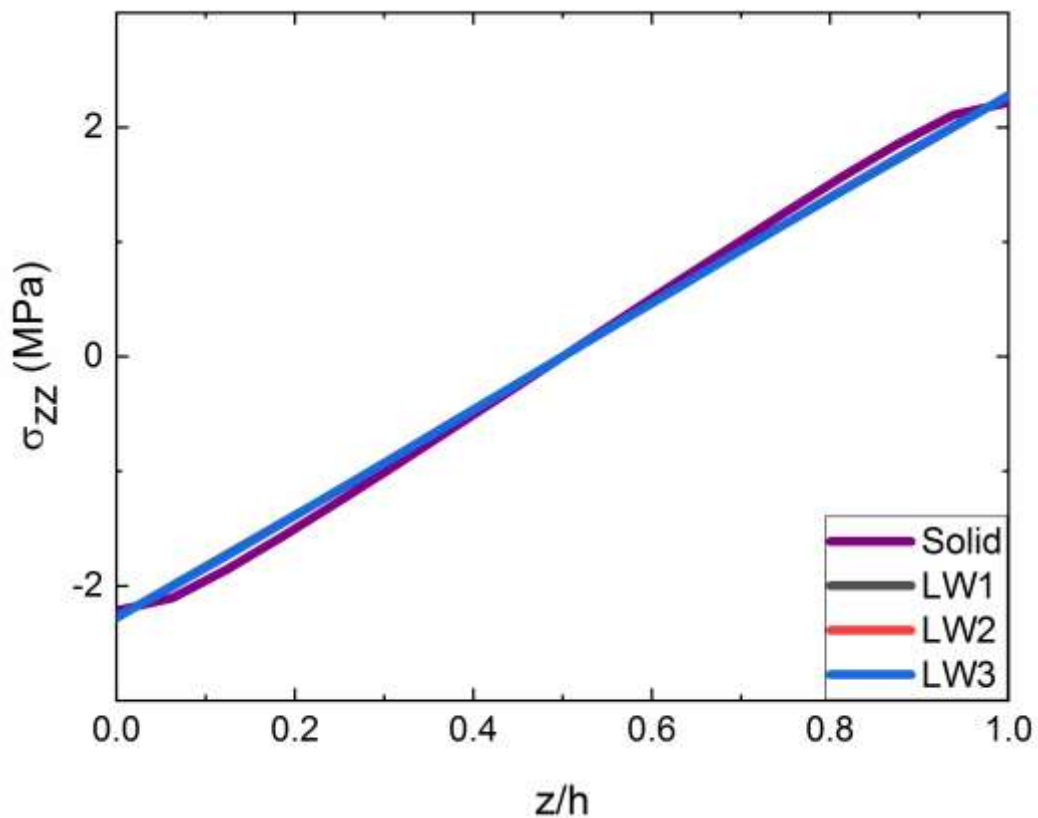
Source: Author.

Figure 40 - Distribution of stresses in YY direction of the first numerical example of $[0]_4$ 

Source: Author.

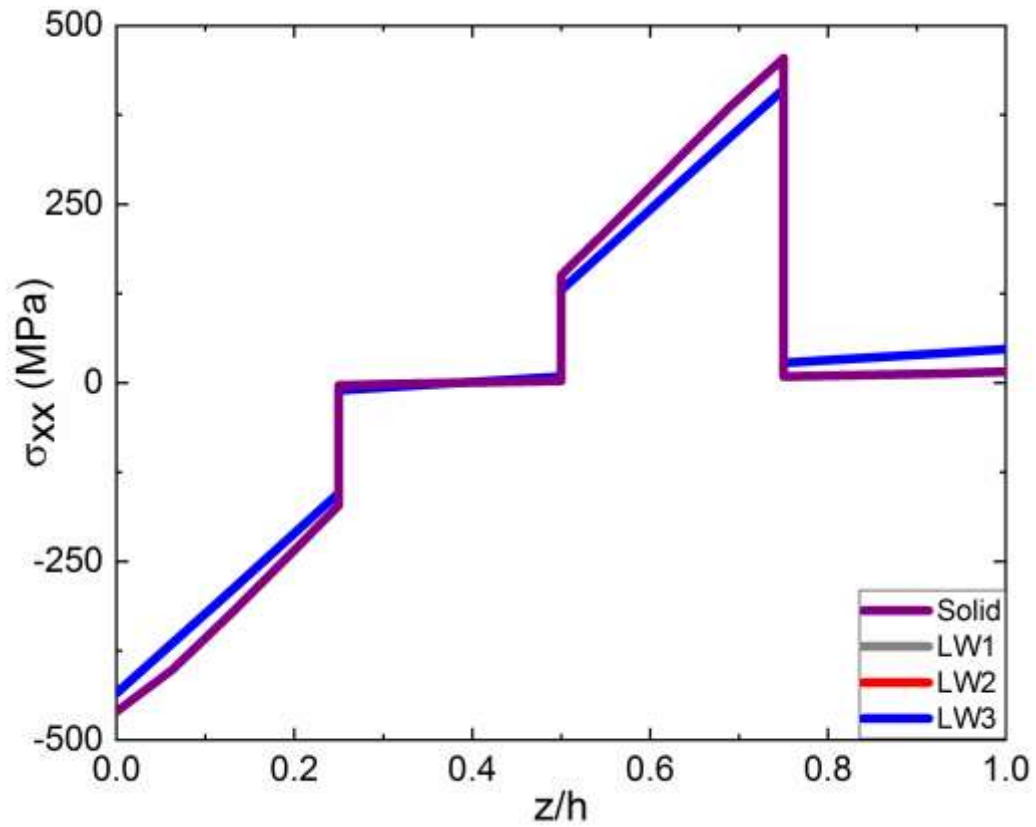
The results of SOLID and layerwise analyses are practically the same on the distribution of stress in ZZ direction (Figure 41). Note that, again, there is no difference between the interpolation degree of the layerwise analyses.

Figure 41 - Distribution of stress in ZZ direction of the first numerical example of $[0]_4$



Source: Author.

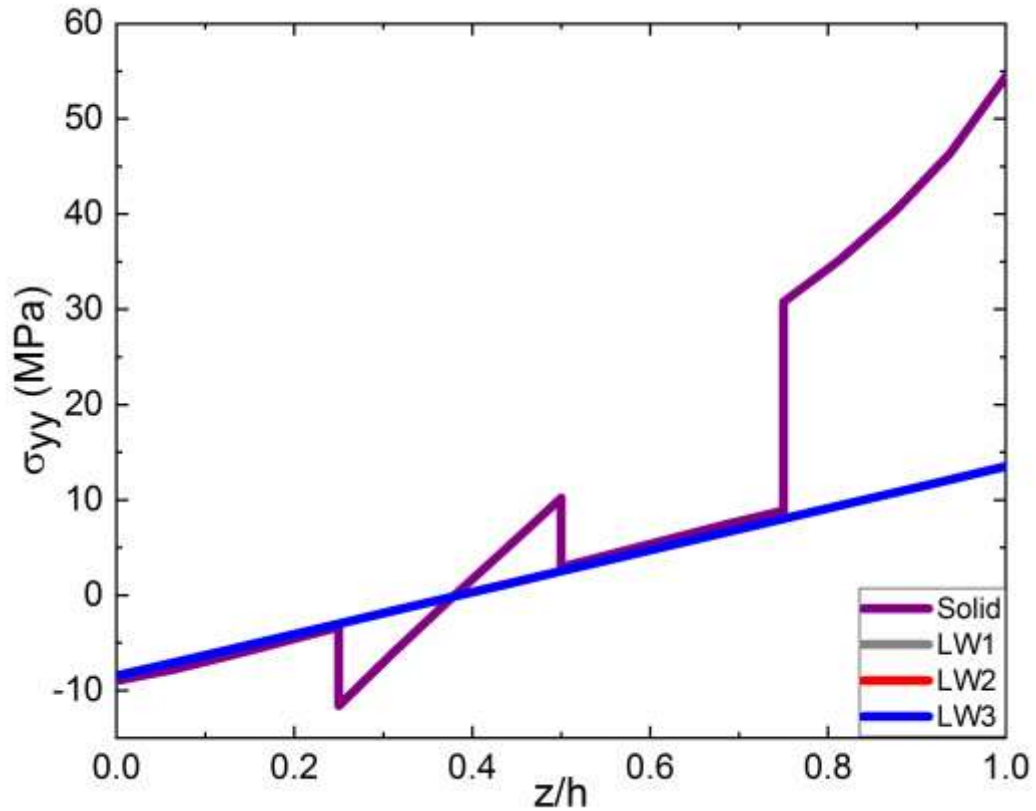
Next, the results of the $[0/90]_2$ laminate. Figure 42 shows the results of the stress distribution in the longitudinal direction (XX in the Cartesian system), which converged in all analyses.

Figure 42 - Distribution of stresses in XX direction of the first numerical example of $[0/90]_2$ 

Source: Author.

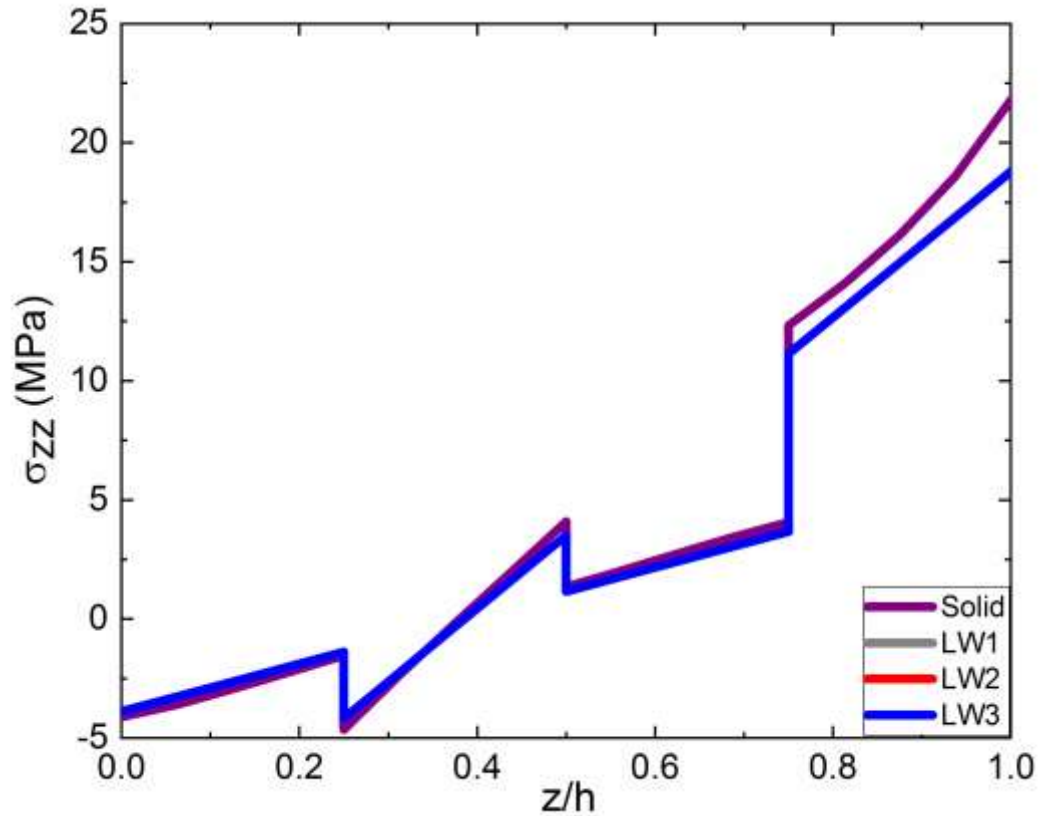
The results of the LW and SOLID analyses diverged in respect to the distribution in YY direction, as illustrated in

Figure 43. The reason for this dissimilarity may be due to the path considered and the difference of the formulations in each analysis. The path is located at the corner of the laminate, plus is in the boundary conditions domain, which can lead to unprecise outcomes.

Figure 43 - Distribution of stresses in YY direction of the first numerical example of $[0/90]_2$ 

Source: Author.

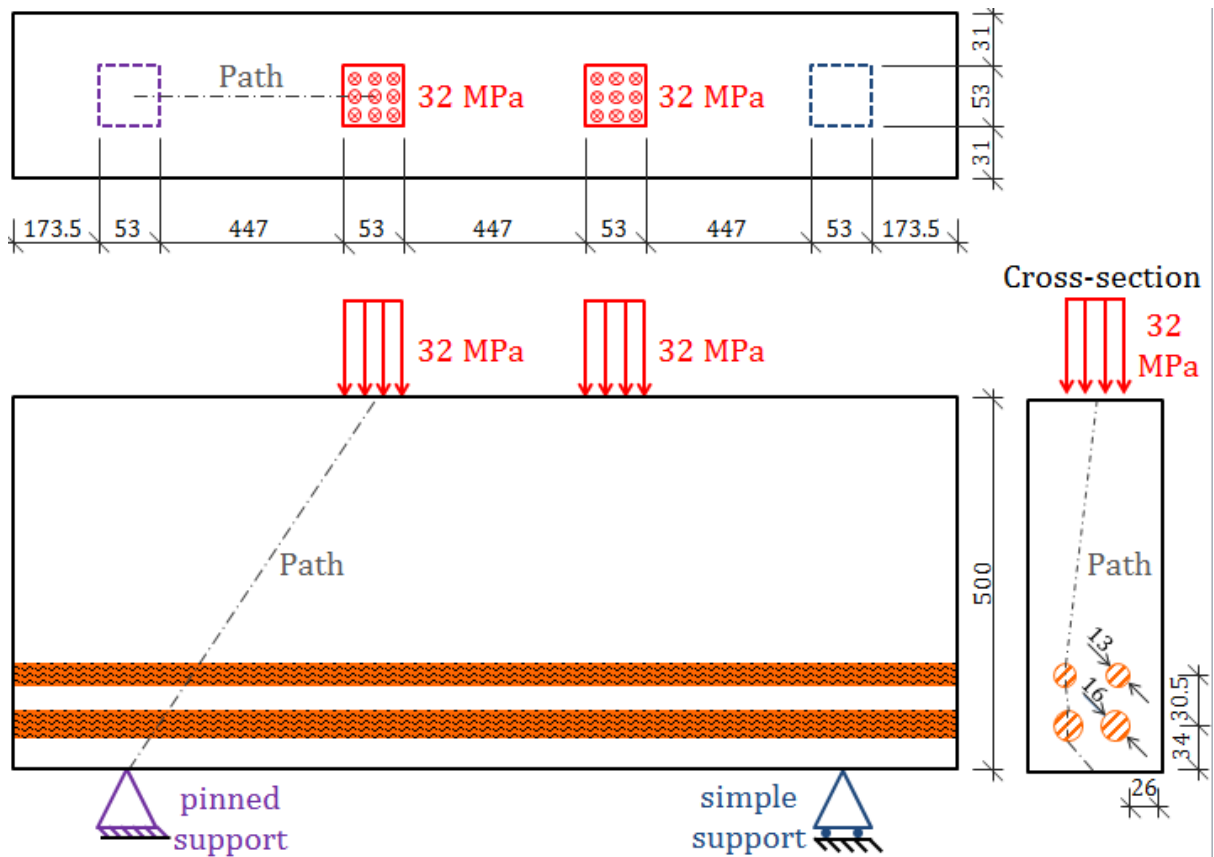
The results regarding the stress distribution in thickness direction converged greatly. Figure 44 shows that all LW analyses are in good agreement with the SOLID analysis. But once more it was not observed any advantage in increasing the interpolation order of the layerwise interpolation. Reddy (2004) has remarked that the layerwise method has a greater impact to thicker structures. In fact, the LW1 analysis in this example has proved that the linear interpolation is sufficient to achieve good results. The next numerical examples are in respect to thicker structures.

Figure 44 - Distribution of stress in ZZ direction of the first numerical example of $[0/90]_2$ 

Source: Author.

The second numerical example is a thick beam made of reinforced concrete already presented in Vilar et al. (2018). This type of element are also known as deep beams; they are heavily loaded structural members that can be found in numerous structures, such as transfer girders in buildings, cap beams in bridge bents, pile caps in foundations, and other cumbersome elements. The geometry and boundary conditions of the deep beam problem are illustrated in Figure 45.

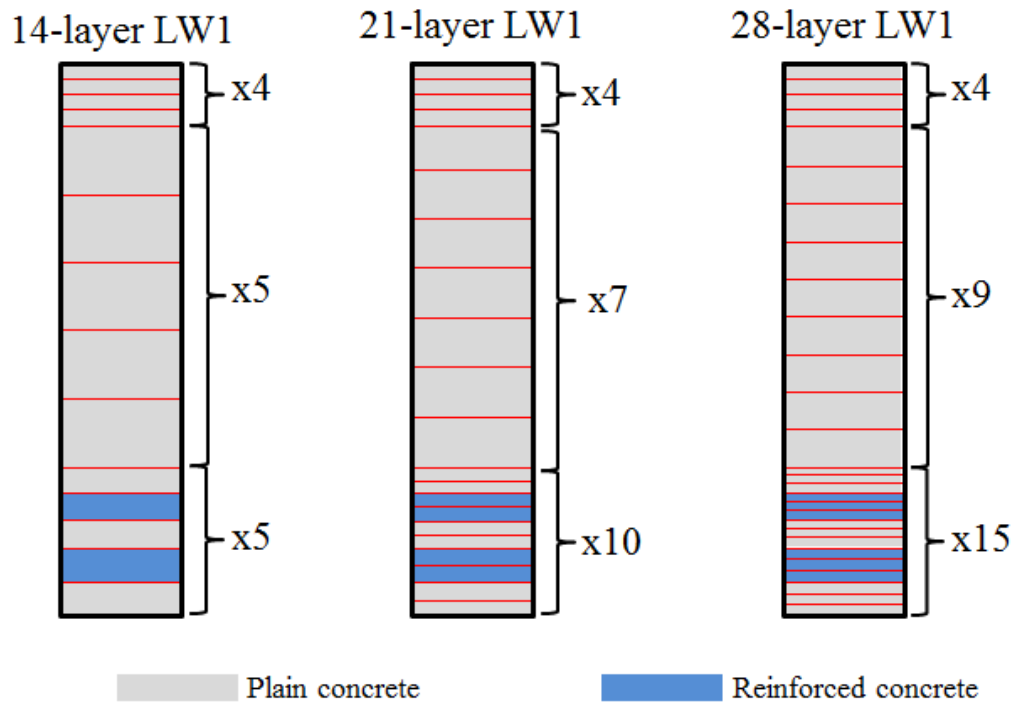
Figure 45 - Schematics of the deep beam numerical example



Source: Vilar et al. (2018).

Three different analyzes using the formulation presented here are performed. Figure 46 schematically illustrates the discretization in thickness direction to each case. Note that the number of virtual layers differs to each layerwise analysis: the cross-section of the *14-layer LWI* is discretized in 14 layers, while the *21-layer LWI* analysis is discretized in 21 layers, and the *28-layer LWI* in 28 layers. The element used in all of the layerwise analyses are the same rectangular 4-node homogeneous isoparametric element of the former numerical example. The interpolation through the thickness however is linear to all analyses. The main purpose of this numerical example is to investigate the impact of refining the cross-section in using linear interpolation through the thickness, as well as validate the formulation for thick beams.

Figure 46 - Discretization of the cross-section of each LW analysis



Modified from: Vilar et al. (2018).

The layers marked as “*plain concrete*” in Figure 46 are modeled as isotropic material, with elastic properties $E_{ii} = 24,602$ MPa, and $\nu_{ij} = 0.25$. The layers labeled as “*Reinforced concrete*” contain both concrete and steel bars. Thus, the elastic properties of these layers are homogenized according to Vilar et al (2018), as defined in Table 4.

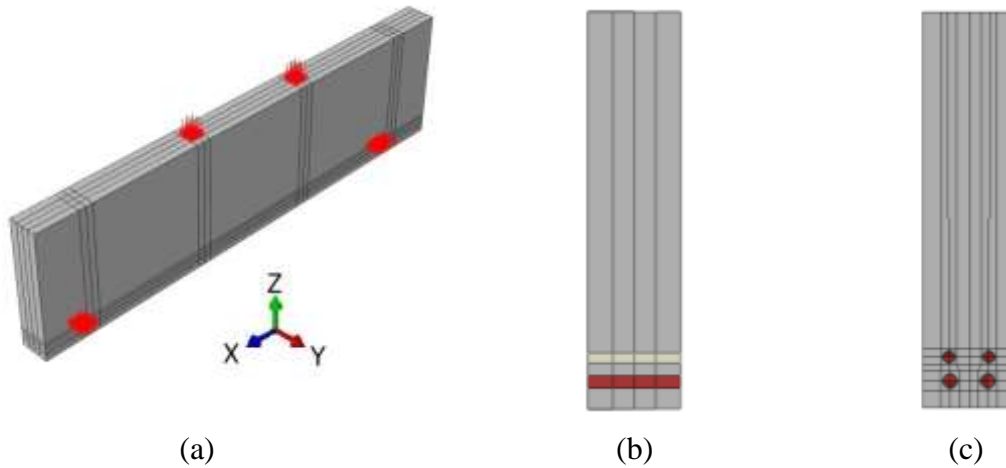
Table 4 - Elastic properties of the virtual layers of the layerwise analyses of the deep beam

	E_{11}	E_{22}	E_{33}	G_{12}	G_{13}	G_{23}	ν_{12}	ν_{13}	ν_{23}
	(MPa)	(MPa)	(MPa)	(MPa)	(MPa)	(MPa)	(-)	(-)	(-)
Homogenized layers ϕ 16mm	61,775.2	30,399.3	E_{22}	12,243.5	G_{12}	G_{12}	0.188	0.241	0.188
Homogenized layers ϕ 13mm	54,113.1	29,098.1	E_{22}	11,702.9	G_{12}	G_{12}	0.199	0.243	0.199

To validate the layerwise analyses, two distinct simulations are carried out in ABAQUSTM, schematically illustrated in Figure 47. The simulation denominated as “ABAQUSTM homogeneous” (Figure 47 b) is based on a solid formulation whose element is the 20-node brick element with parabolic interpolation in all directions (C3D20 element of ABAQUSTM software). The elastic properties in this model are the same as the layerwise analyses.

The other simulation carried out to validate the layerwise model is the “ABAQUSTM heterogeneous”, schematically illustrated in Figure 47 (c). There is no homogenized layers in this analysis. The steel bars are manually designed with a cylindrical shape whose material is modeled as isotropic with the following elastic properties: $E_{ii} = 210,000$ MPa, and $\nu_{ij} = 0.33$. The discretization of the cross-section has been already presented in Figure 46. The type of element is the same of the ABAQUSTM homogeneous with one additional feature: the formulation of the element is hybrid (C3D20H). It is assumed that the steel bars are completely enveloped by concrete and perfectly bonded to it. In addition, the Young’s modulus of the steel is considerably superior to the concrete’s. Hence the response of the steel bars is nearly incompressible, meaning a very small change in displacement results in a large changes in pressure, so that a purely displacement-based solution is too sensitive to be useful numerically (Simulia DS Corp, 2011). The formulation of the hybrid element C3D20H of ABAQUSTM eliminates this singular behavior by describing the pressure stress as an independently interpolated basic solution variable, coupled to the displacement solution through the constitutive theory and the compatibility condition.

Figure 47 - (a) Isometric view of the general geometry of the beam modeled in ABAQUS™, with boundary conditions; (b) front view of the homogeneous model; (c) front view of the heterogeneous model.



Source: Vilar et al. (2018).

The mesh of the layerwise analyses have been refined until convergence, resulting in 1,449 elements with 1,536 nodes. The number of virtual layers, however, differs in each analysis, resulting in more degrees of freedom in the analyses with more virtual layers. Table 5 displays the quantity of layers and DoFs in each analysis and also of ABAQUS™ simulations.

Table 5 - Discretization of each analysis

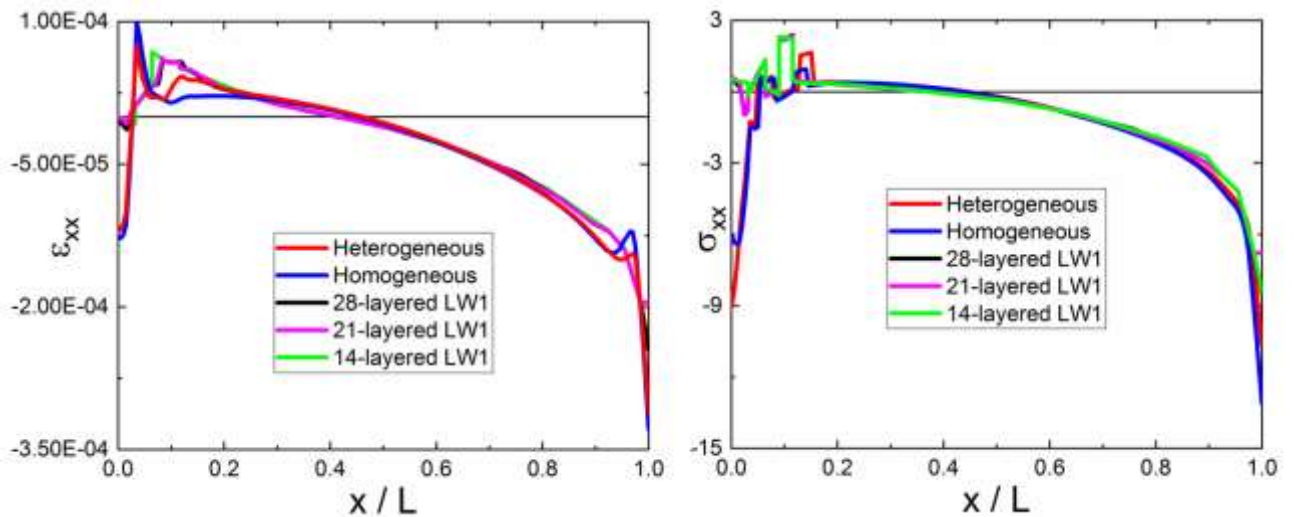
	Number of layers	DoFs
LW1	14	69,120
LW2	21	101,376
LW3	28	133,632
ABAQUS™ homogeneous	-	1,003,860
ABAQUS™ heterogeneous	-	3,376,914

To compare the results of all analyses, the distribution of stresses and strains are taken through the path defined in Figure 45. The reference is located at the pinned support (at the

pinned support $x = 0$ and at the applied pressure $x = L$). Regarding the analysis *ABAQUSTM heterogeneous*, the path crosses the center of the steel reinforcements.

Figure 48 shows the behavior of the stress and strain distributions in longitudinal direction (XX direction). The perturbations near the bottom end is due to abrupt change of the elastic properties. Observe that the layer with the steel bars are under tensile stress, which is in accordance to the concept of the reinforced concrete material, because the reinforcement is responsible to bear the tensile stress while the concrete is usually under compressive stresses.

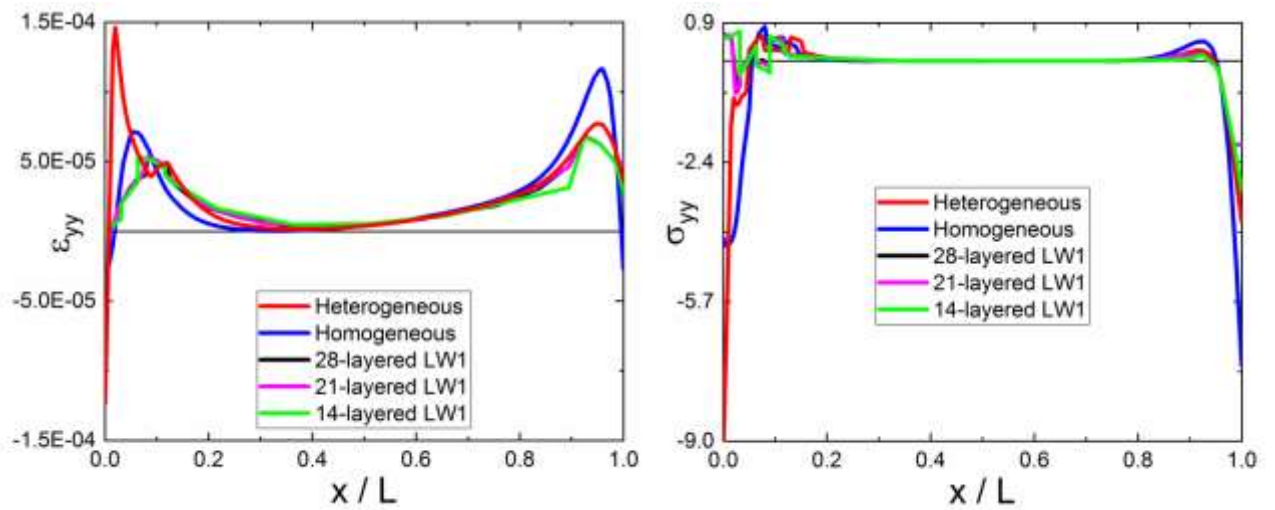
Figure 48 - a) normal strain in XX direction; b) normal stress in XX direction



Source: Vilar et al. (2018).

Figure 49 is the out-of-plane component of the strain/stress tensors, which are approximately zero all over the domain of the path but not near the boundary conditions.

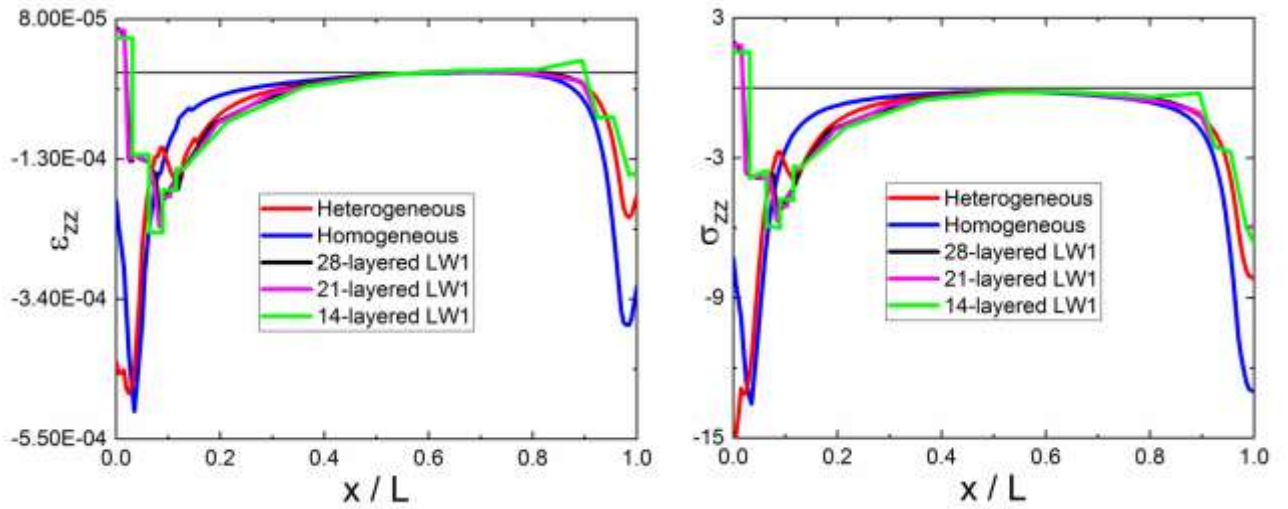
Figure 49 - a) normal strain in YY direction; b) normal stress in YY direction



Source: Vilar et al. (2018).

Figure 50 is the strain/stress in the height direction (ZZ direction). All curves converge over the middle area of the path, but not the strains. Furthermore, both layerwise and ABAQUSTM analyses capture the phenomenon of the discontinuity of the stress field at the interface between concrete and reinforcements. The discontinuity is more visible in the layerwise curves, because since the approximation of the displacement field is linear, the discontinuity on the interfaces of stresses and strains is a vertical leap. Conversely, due the fact that the trial solutions of ABAQUSTM simulations are approximated by a second-order polynomial, the strain/stress exhibit a kink on the interfaces of the materials.

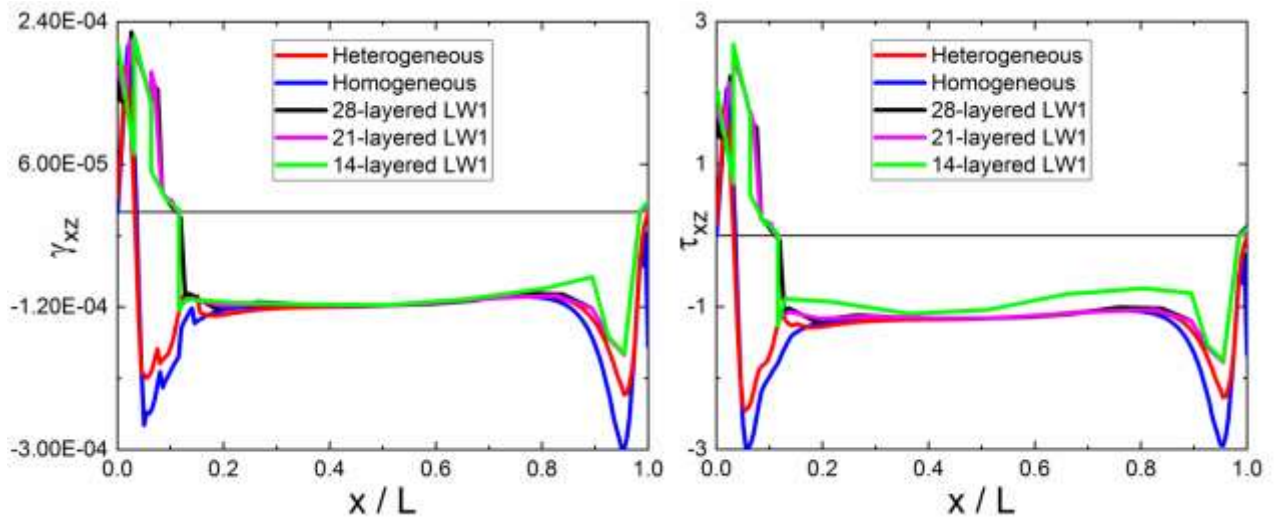
Figure 50 - a) normal strain in ZZ direction; b) normal stress in ZZ direction



Source: Vilar et al. (2018)

Figure 51 shows the behavior of the strain and shear stress in XZ direction. At the boundaries the results are different but show the same trend. At the bottom and top surfaces both shear and strain in XZ direction converge to zero, meaning all curves meet the natural boundary condition of free shear strain/stress at both ends.

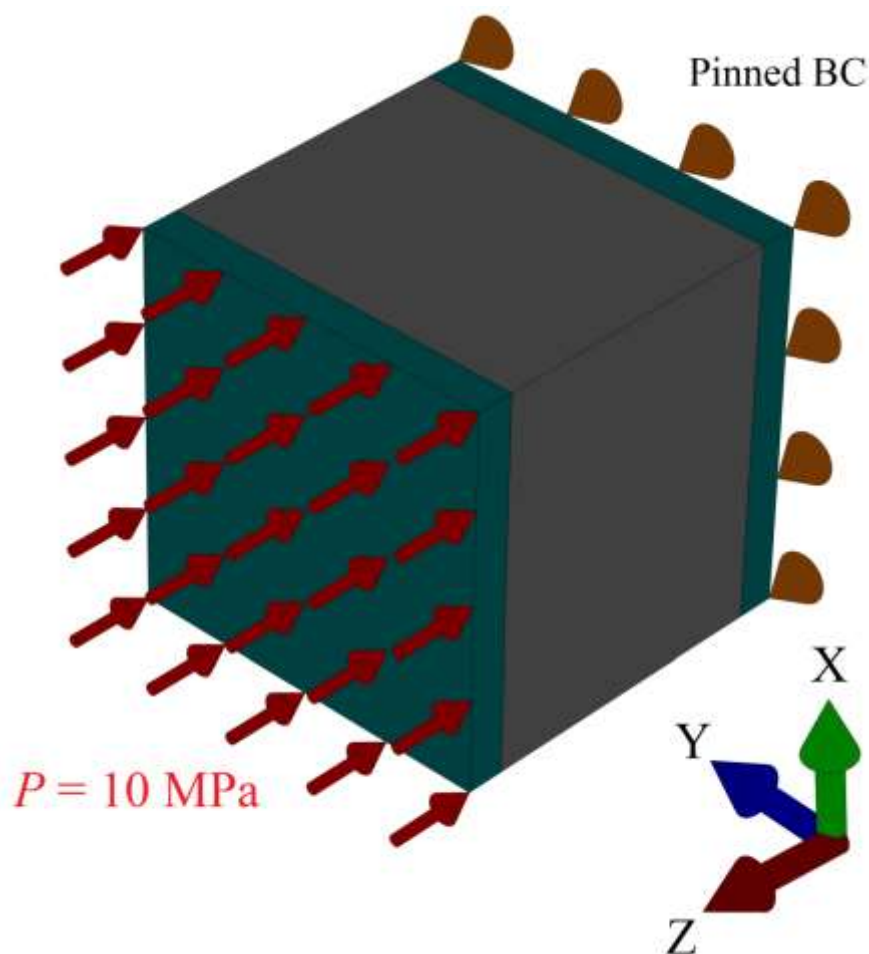
Figure 51 - a) shear strain in xz direction; b) shear stress in xx direction.



Source: Vilar et al. (2018)

The third numerical example is a three-layered composite sandwich solid under compressive pressure over the top layer with magnitude of 10 MPa, and simply supported on the bottom layer. Figure 52 illustrates the geometry and boundary conditions of the sandwich example. The skins of the composite have 10mm of thickness while the core has 80mm, and the in-plane dimensions are 100mm in both directions.

Figure 52 - Schematics of the composite sandwich numerical example



Source: Author.

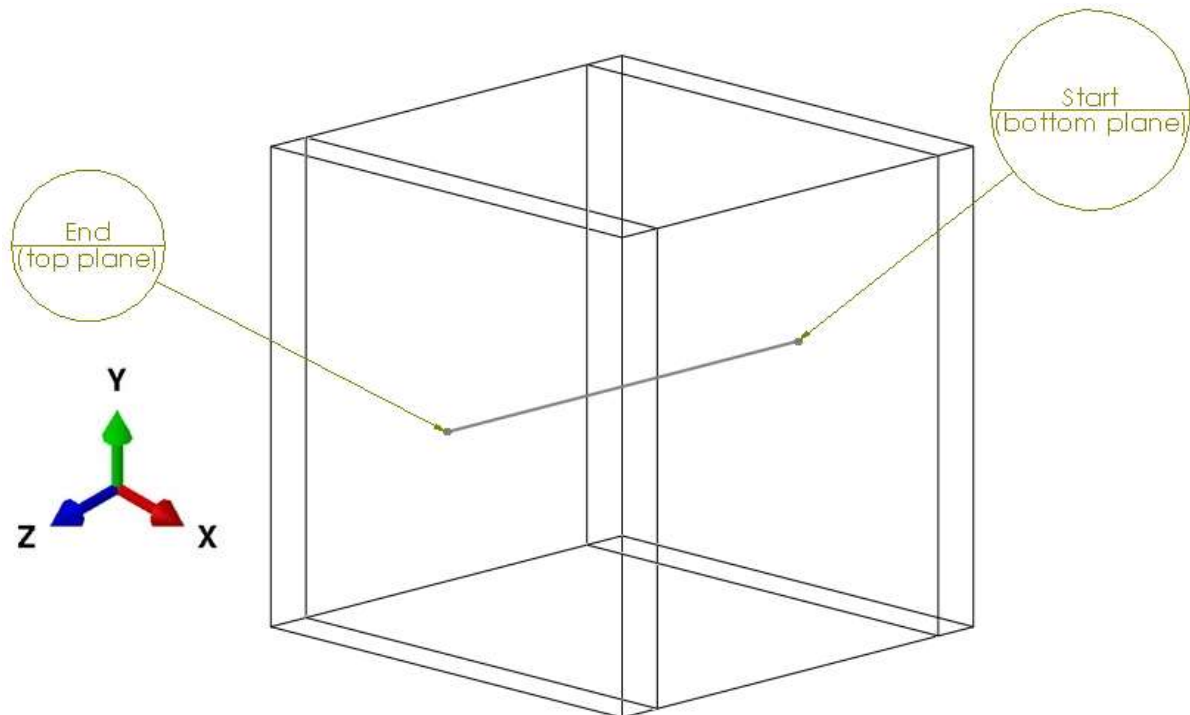
The elastic properties of the two skins and the core are defined in Table 6, note that the skins are orthotropic while the core is isotropic, and the orientation of the laminate is $[0]_3$, thus the fiber of the skins are parallel to the X axis.

Table 6 - Elastic properties of the skins and the core of the sandwich composite

	E_{11}	E_{22}	E_{33}	G_{12}	G_{13}	G_{23}	ν_{12}	ν_{13}	ν_{23}
	(MPa)	(MPa)	(MPa)	(MPa)	(MPa)	(MPa)	(-)	(-)	(-)
Skins	127,000	10,000	10,000	5,400	5,400	3,050	0.34	0.34	0.306
Core	53	53	53	25.6	25.6	25.6	0.35	0.35	0.35

The analyses of the first numerical example (the thin 4-layered composite plate) are also carried out in this sandwich composite example, including the SOLID analysis of ABAQUSTM to validate. To compare stresses, the path taken is a straight line aligned to the thickness direction, and passing through the center of the XY plane, as displayed in Figure 53.

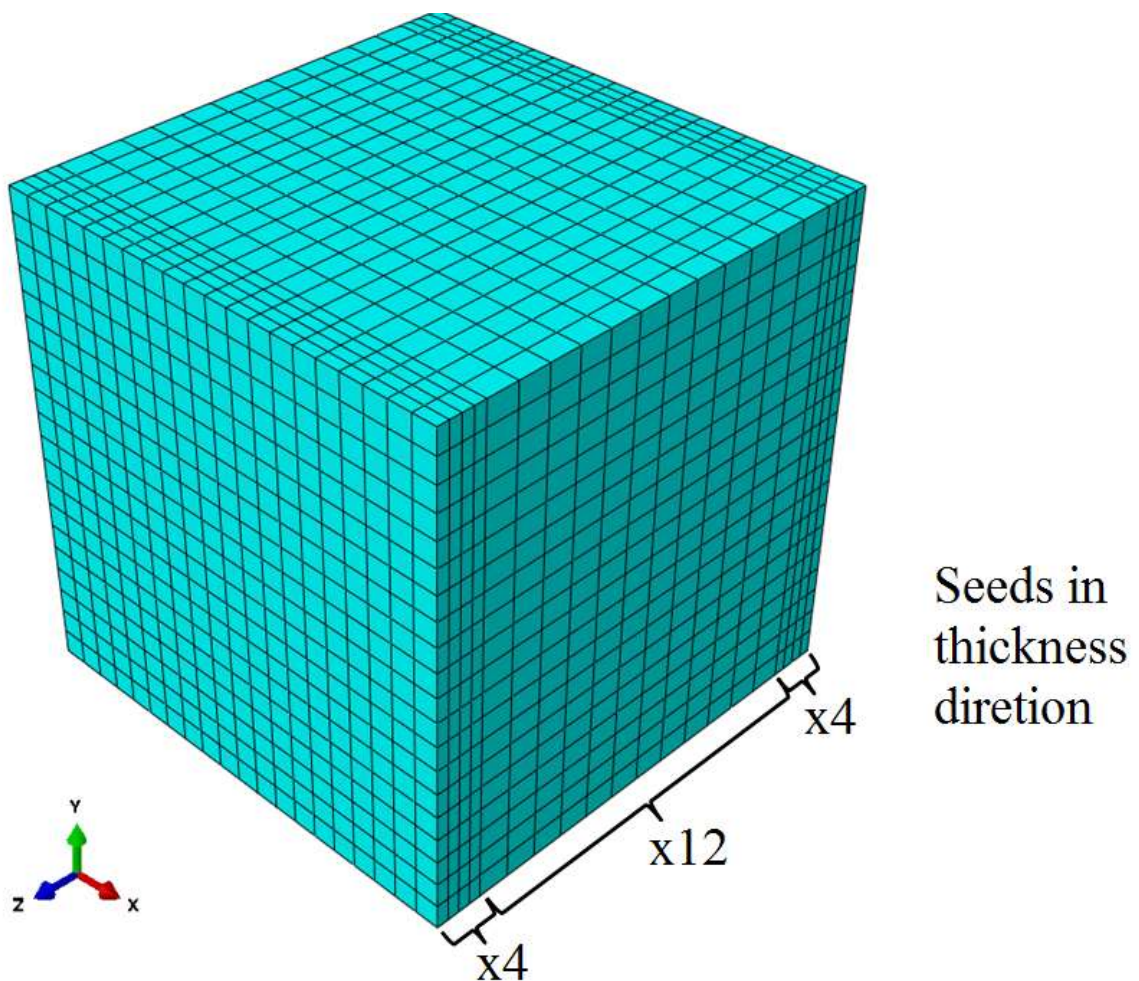
Figure 53 - Path taken to compare stresses of the sandwich composite case



Source: Author.

The elements of the mesh in the LW analyses are all quadrilaterals, with only one virtual ply discretized to each lamina. The mesh of the SOLID analysis of ABAQUS™ has also quadrilateral in-plane geometry, and seeds in the mesh have been created throughout the thickness, resulting in four seeds to the skins and twelve to the core, as demonstrated in Figure 54.

Figure 54 - Mesh discretization of the composite sandwich numerical example with the seeds created in the thickness direction

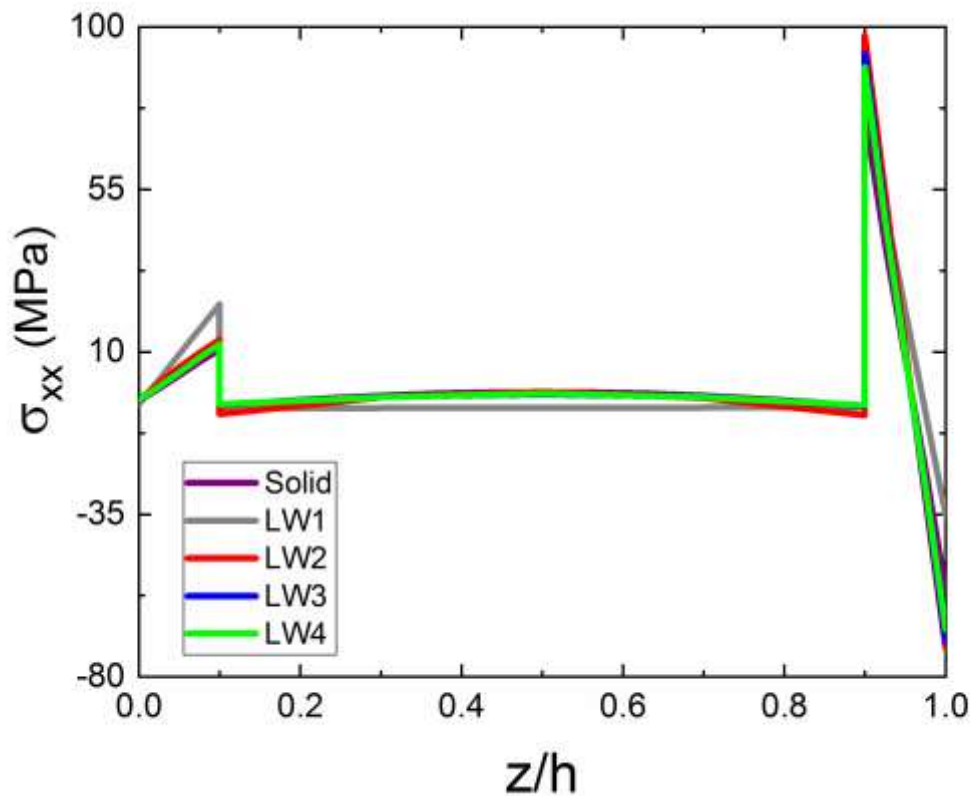


Source: Author.

Figure 55 is the distribution of the normal stress in XX direction. Note that the skins are in a more severe state of stress, fact explained due to have more rigid elastic properties.

The skin closer to the external load is under higher stress. Also, observe the discontinuity of the stresses at the core/skin interfaces.

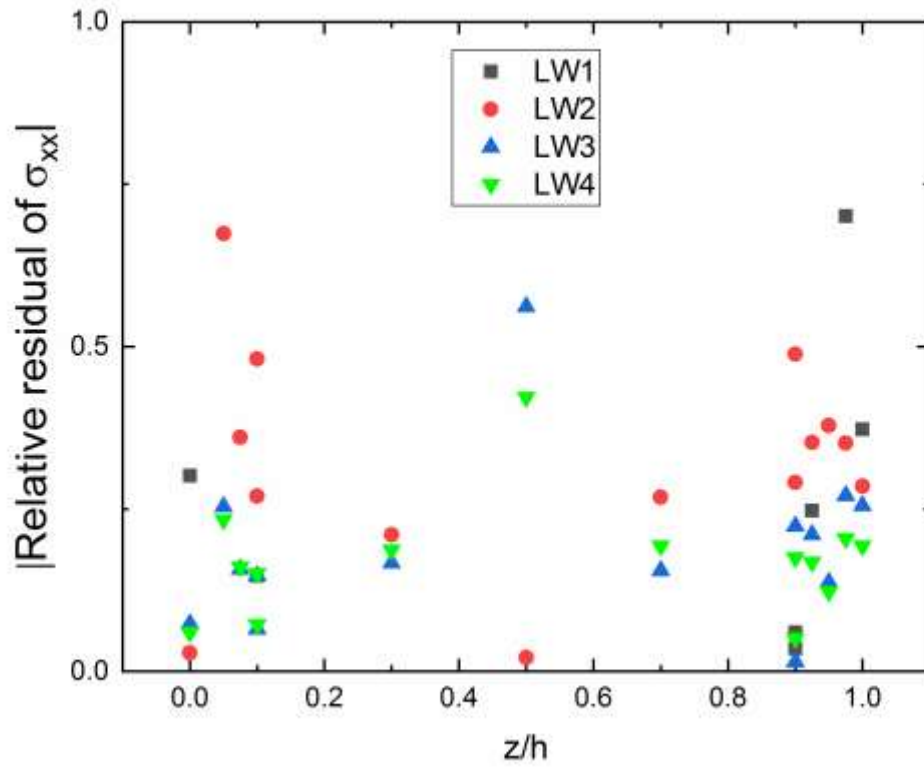
Figure 55 - Normal stress distribution in the XX direction of the sandwich composite case



Source: Author.

The results of the distribution of normal stresses in XX direction are closer to the SOLID analysis of ABAQUSTM for higher degrees of the layerwise interpolation. This statement is confirmed by the dispersion graphic of Figure 56, which is the absolute values of the relative residual in relation to the SOLID analysis in XX direction. This graphic shows that the LW4 is practically more accurate than the other analyses, but there is not much difference from the outcome of the LW3. The LW1 analysis has demonstrated the highest deviation to the SOLID analysis; the absolute relative residuals are greater than the graphic limits, thus this conclusion may not be clear by only examining Figure 56.

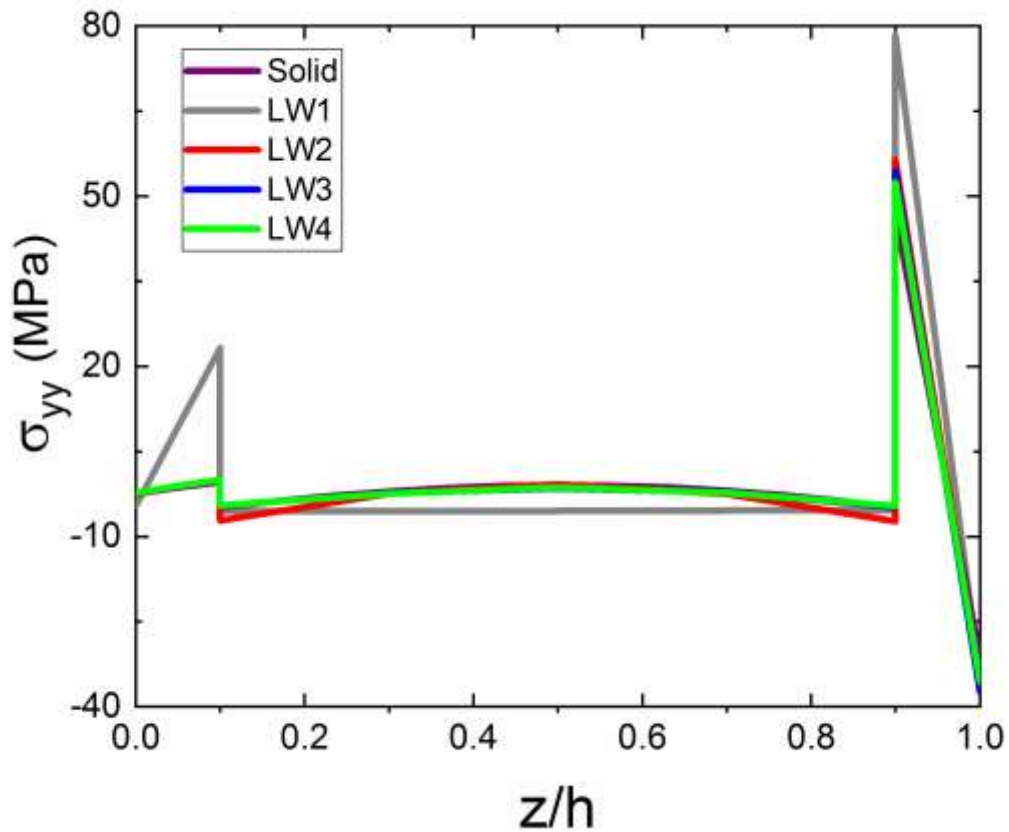
Figure 56 - Absolute value of the relative residual of the layerwise analyses in relation to the solid-like analysis carried out in ABAQUS™ in XX direction



Source: Author.

Figure 57 is the distribution of normal stress in YY direction, which has the same trend as in XX direction with lower magnitude of the stresses, fact explained that the fiber of the skins are oriented in the XX direction, thus the whole laminate is more rigid in this direction. The LW1 analysis has been more imprecise in this direction

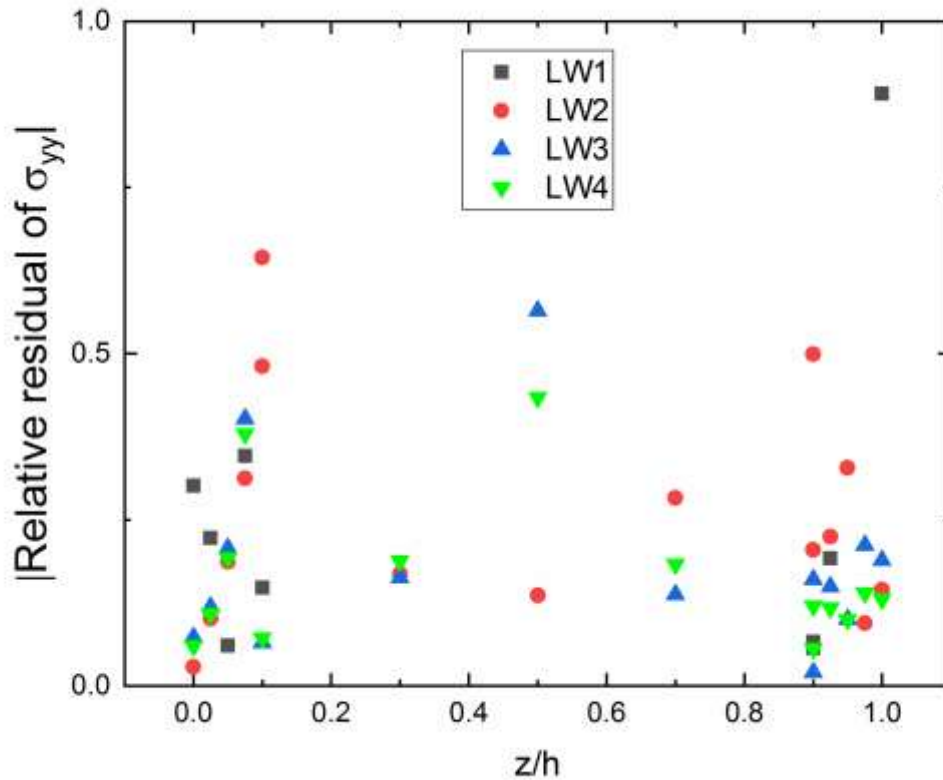
Figure 57 - Normal stress distribution in the YY direction of the sandwich composite case



Source: Author.

Figure 58 shows the absolute relative residual of the LW analyses in relation to the SOLID of ABAQUSTM in the YY direction. As expected, the LW4 has the better results, followed by LW3, LW2 and LW1 respectively. In general, the outcome of the LW analyses have been deviated in relation to the SOLID more in the YY direction than the XX direction.

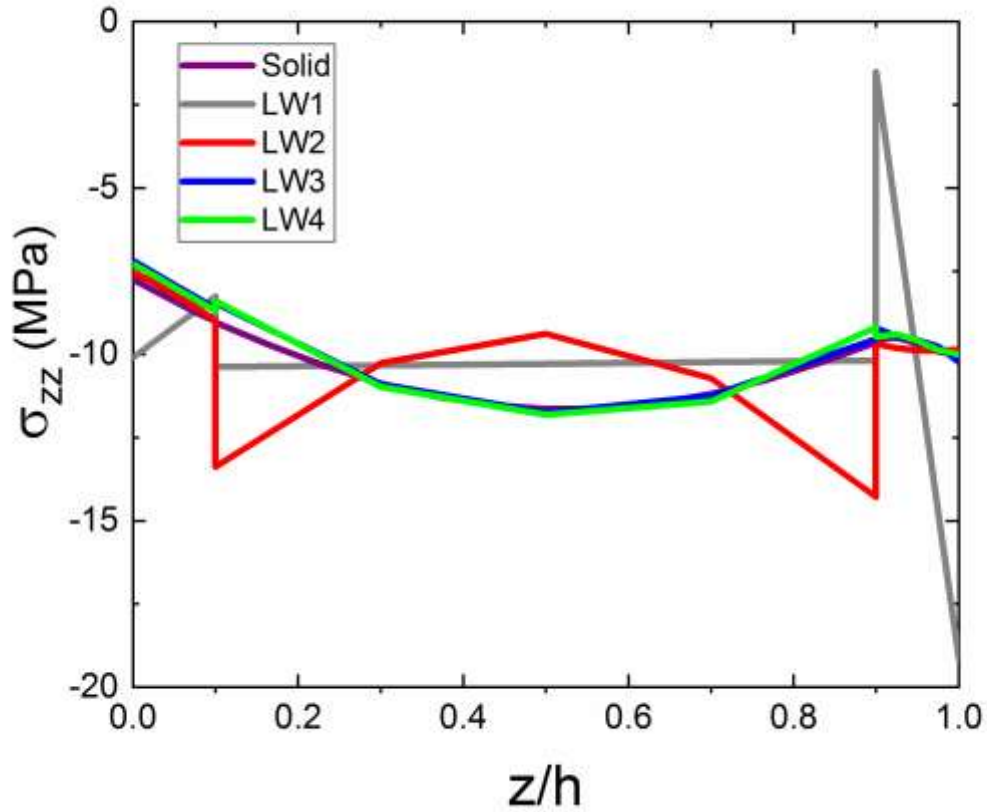
Figure 58 - Absolute value of the relative residual of the layerwise analyses in relation to the solid-like analysis carried out in ABAQUSTM in YY direction



Source: Author.

Figure 59 is the distribution of normal stress in ZZ direction. The trend of distribution of the normal out of plane stress is different from the in-plane components. The cubic interpolation (LW3) is sufficient to achieve the same result of the SOLID analysis done in ABAQUSTM. The parabolic and linear interpolations (LW2 and LW1 respectively) have shown discontinuity at the interfaces, whereas in LW3 and LW4 the out of plane stress is continuous as in the SOLID analysis. The linear interpolation has shown poor results to this case; the discontinuity at the skin/core interface near the top plane is too high, and the interpolation in the core domain (in the interval [0.1; 0.9]) pointed out a constant stress distribution, which differs from the SOLID and LW3 and LW4.

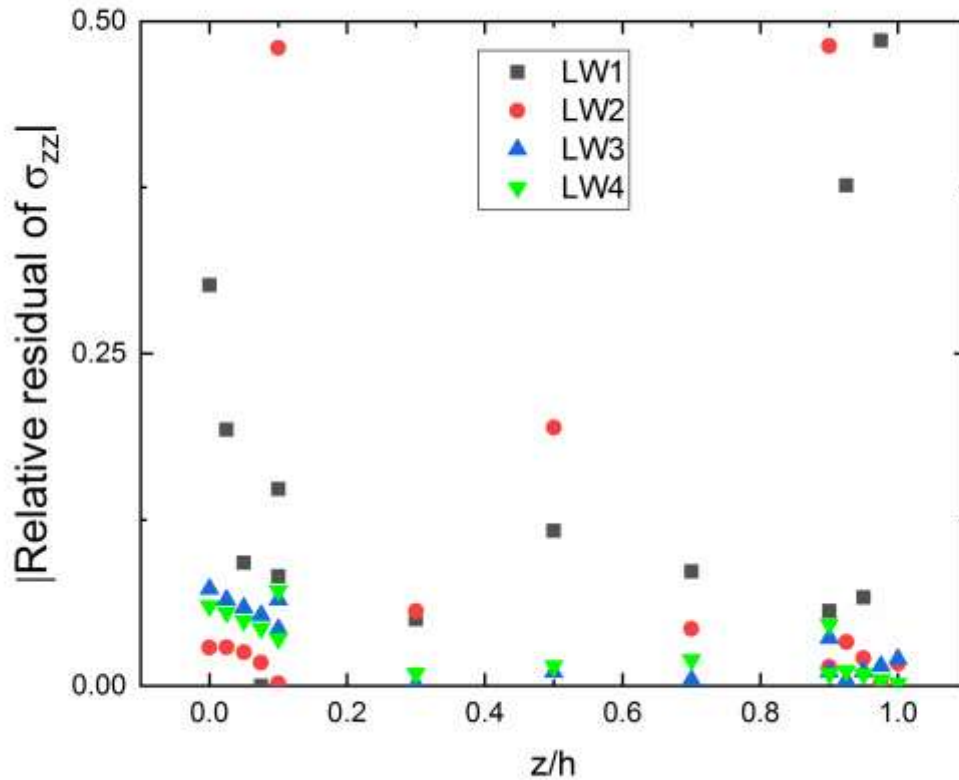
Figure 59 - Normal stress distribution in the ZZ direction of the sandwich composite case



Source: Author.

Figure 60 shows the absolute relative residual of the LW analyses in relation to the SOLID of ABAQUS™ in ZZ direction. In general, the precision of the analyses have shown greater results in this direction; the magnitude of the graphic relative residual had been halved for better visualization (the limit of the ordinate is 0.5 instead of 1.0 of Figure 56 and Figure 58). The LW4 has shown the best results; although the LW2 has exhibited the best accuracy near the bottom boundary condition. The linear interpolation has presented the less accurate outcome.

Figure 60 - Absolute value of the relative residual of the layerwise analyses in relation to the solid-like analysis carried out in ABAQUS™ in ZZ direction



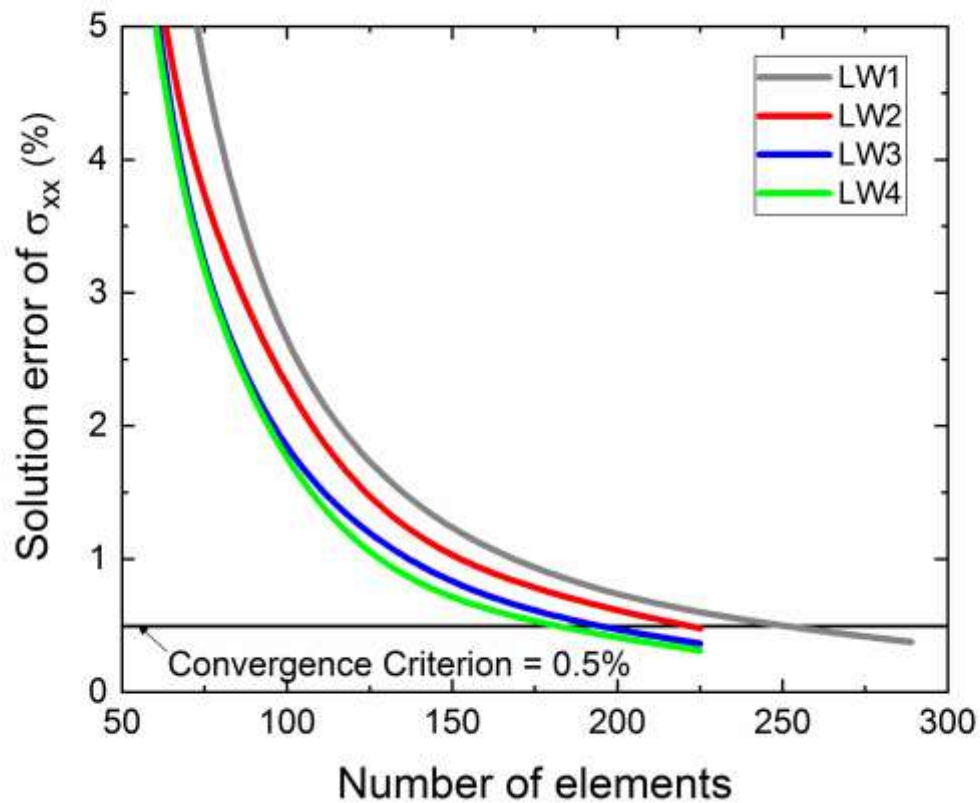
Source: Author.

There are multiple types of convergence analyses. According to Bathe (1996), solution errors arise when the mesh is refined until the outcome slightly varies. In the next figures, the convergence of the results in each direction of the stresses are analysed. To proceed with the convergence analysis, the mesh is incremented by a fixed value of elements and the outcome of each analysis is compared to the outcome of the previous analysis. This convergence analysis is stopped until the relative residue is inferior to 0.5%. The location chosen to investigate the stresses convergence is situated at the intersection of the top plane of the laminate and the path of Figure 53 (or $z/h = 1$).

Figure 61 shows the convergence analysis in the XX direction. The rate of convergence is practically the same in this direction, and around 200 elements, the relative

residue is reached to LW2, LW3 and LW4, whereas the linear analysis requires roughly 250 elements.

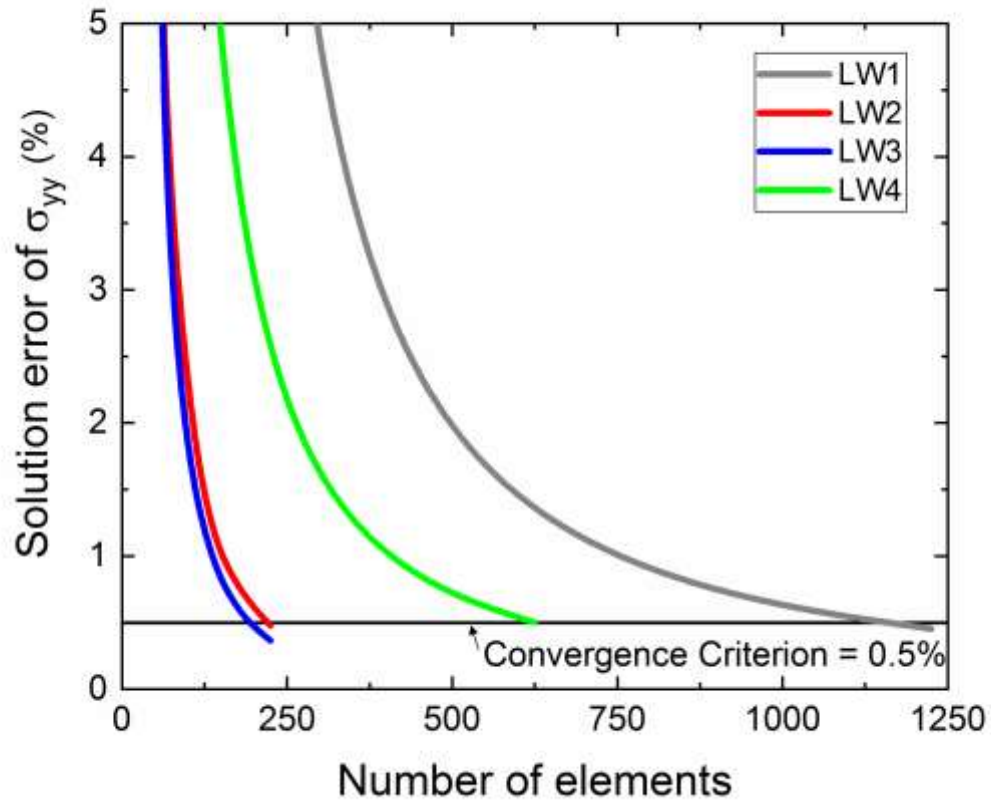
Figure 61 - Convergence analysis based on the solution error in XX direction



Source: Author.

Figure 62 shows that the convergence in YY direction is considerably slower than in XX direction. An interesting fact is that the convergence of the quadratic and linear analyses are faster than the LW4. The convergence criterion has been satisfied in 250 elements in the LW2 and LW3, while it was required about 600 elements to the LW4 analysis, and 1200 elements to the linear interpolation.

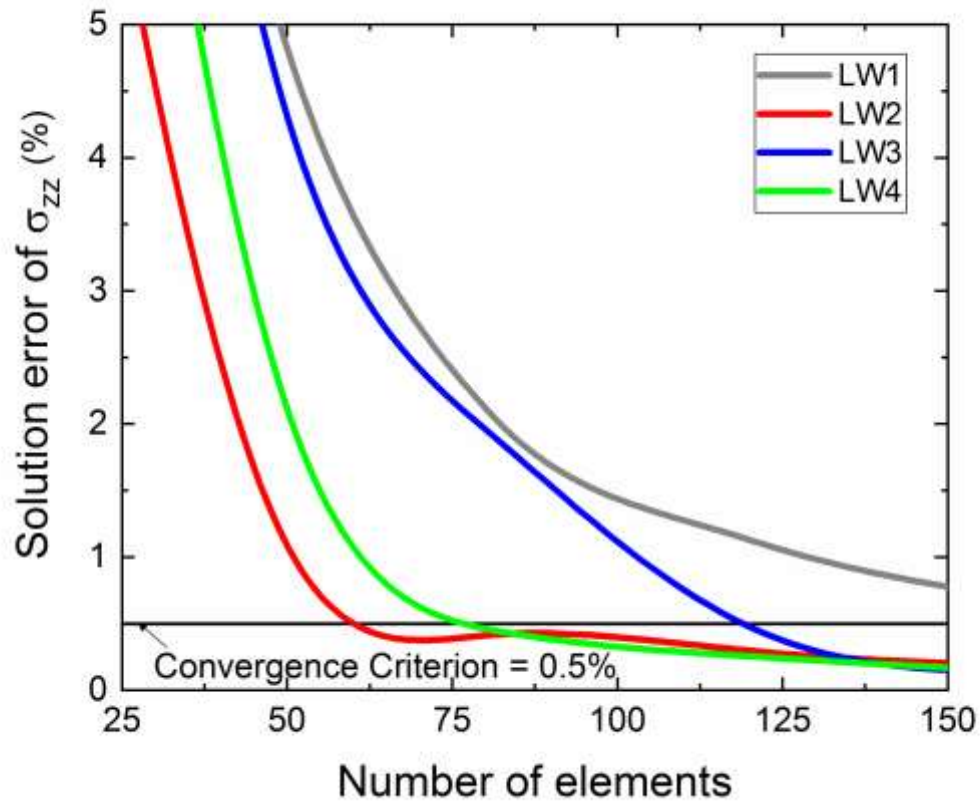
Figure 62 - Convergence analysis based on the solution error in YY direction



Source: Author

Figure 63 shows the convergence analysis in the ZZ direction. The fastest convergence occurred to the quadratic interpolation, in which the convergence criterion has been achieved with approximately 60 elements. Next, the LW4 analyses has fulfilled the criterion with 75 elements, followed by the cubic analysis, which has reached the criterion with around 115 elements. The linear interpolation has been slower the other analyses, the convergence has been reached after a refinement of 200 elements.

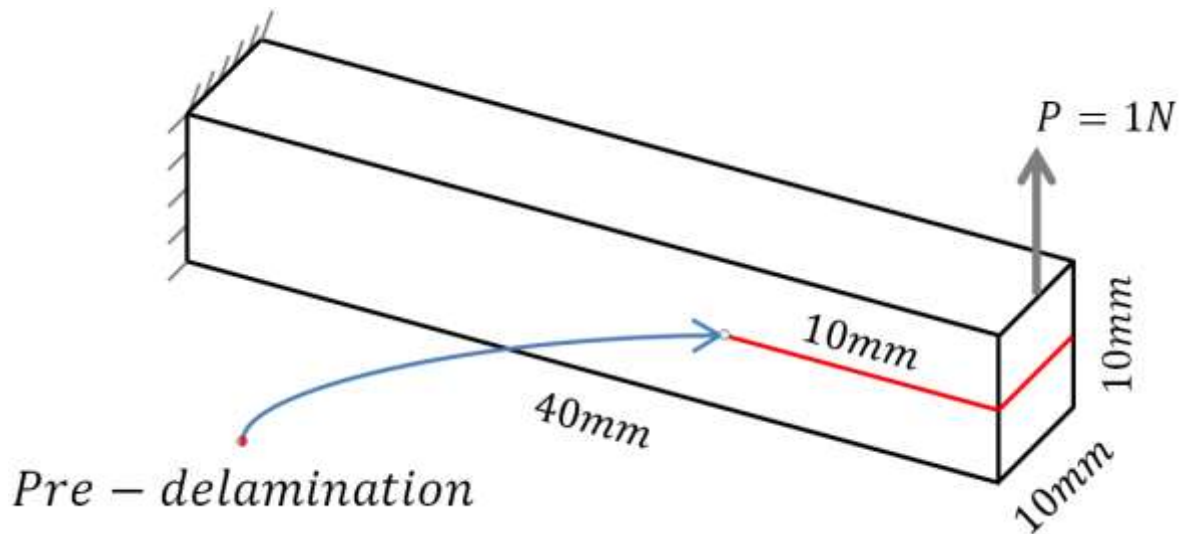
Figure 63 - Convergence analysis based on the solution error in ZZ direction



Source: Author.

The fourth numerical example is a composite beam with a pre-delaminated zone, whose boundary conditions and geometry are shown in Figure 64. Three different stacking sequences are considered for this case: $[0]_8$, $[0/90/0/90]_S$ and $[90/0/90/0]_S$. The elastic properties are the same of the first numerical example.

Figure 64 - Boundary conditions and geometry of the fourth numerical example



Source: Author.

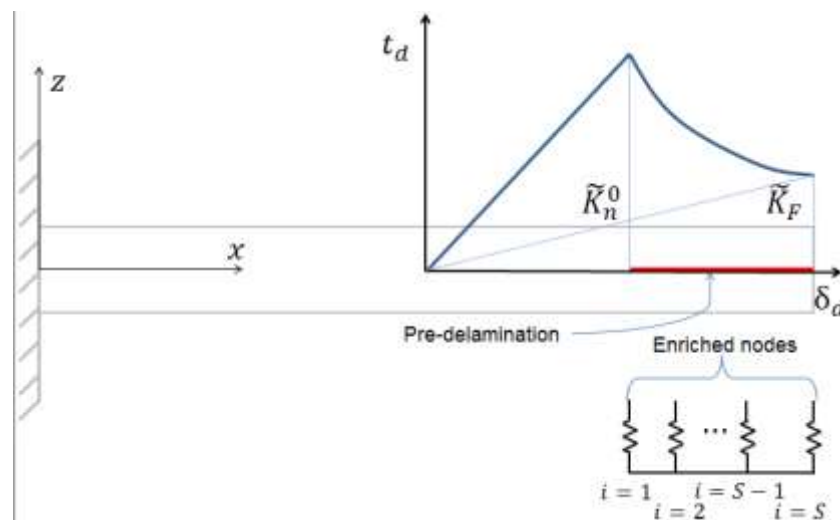
The numerical example of Figure 64 has been solved through the extended layerwise finite element method. To approach this problem, Li et al. (2015) proposed strong enrichments to cracked elements using the Heaviside function, plus weak enrichments at each interface between laminas using the signed distance function and crack tip enrichments. The number of virtual layers was 8 (1 virtual layer for each ply). To validate the model proposed, Li et al. (2015) carried out similar analyses on MSC. Partran.

The delaminated area in Li et al. (2015) remains the same, thus, there is no progressive failure nor damage propagation in their work. In consequence, if the load P is released the composite beam return to its initial state. The same case presented by Li et al. (2015) is solved here with a similar approach. The main difference is the absence of the weak and crack tips enrichments. The strong enrichments are applied to the pre-delaminated zone only.

To solve the problem of Figure 64 with the formulation introduced in this dissertation, it is required to model the constitutive relation of the cohesive elements of the delaminated area of the composite beam. However, instead of subdividing the load in several steps, solving the non-linear system and calculating the damage variable D_d of equation (26), like in traditional CZM procedure, the problem here is approached differently. The stiffness of each cohesive element is pre-determined here according to an exponential distribution presented in Figure 65. The procedure to apply a traction-separation law without performing progressive failure is similar

to usual CZM approach. In other words, the methodology used to solve this case does not calculate the damage variable; the stiffness of each cohesive element is pre-defined according to the dummy stiffness and the exponential distribution of equation (57). The reason for choosing this approach for this problem is because Li et al. (2015) have not proceeded with progressive failure, and also, the aim of this problem is not to model progressive delamination, but to show that the formulation proposed here has the potential to perform structural analyzes in a pre-delaminated structure. To apply progressive failure in this numerical example is required is to model the traction-separation law and to approach the problem as non-linear.

Figure 65 - Traction separation law of the cohesive zone of the second numerical example



Source: Author.

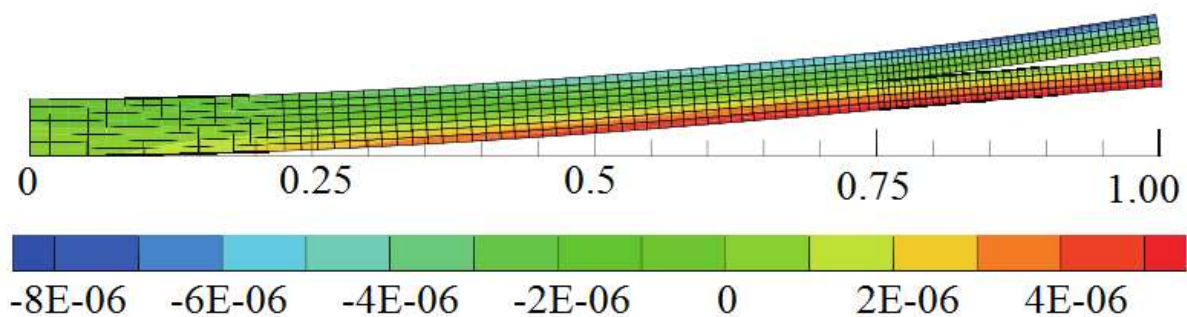
The degradation of the stiffness is represented in equation (57), where S is the number of strong enrichments. Note that for node $i = 1$, the stiffness of the cohesive element is the dummy stiffness \tilde{K}_n^0 . Analogously, the cohesive stiffness of the node at the free edge is \tilde{K}_F , and the cohesive stiffness of any intermediate node is calculated according to equation (57).

$$\tilde{K}_i = \tilde{K}_n^0 - (\tilde{K}_n^0 - \tilde{K}_F) \left(\frac{i}{S/2} \right)^2 \quad (57)$$

The dummy stiffness \tilde{K}_n^0 and final the stiffness at the tip \tilde{K}_F are numerically determined. Therefore, the trial and error method was applied to determine these numerical parameters. The results of the case presented is greatly sensible to the dummy stiffness \tilde{K}_n^0 , and its value depends on the number of enriched nodes. The α parameter of the enriched function of equation (32) is initially set to $\alpha = 100$.

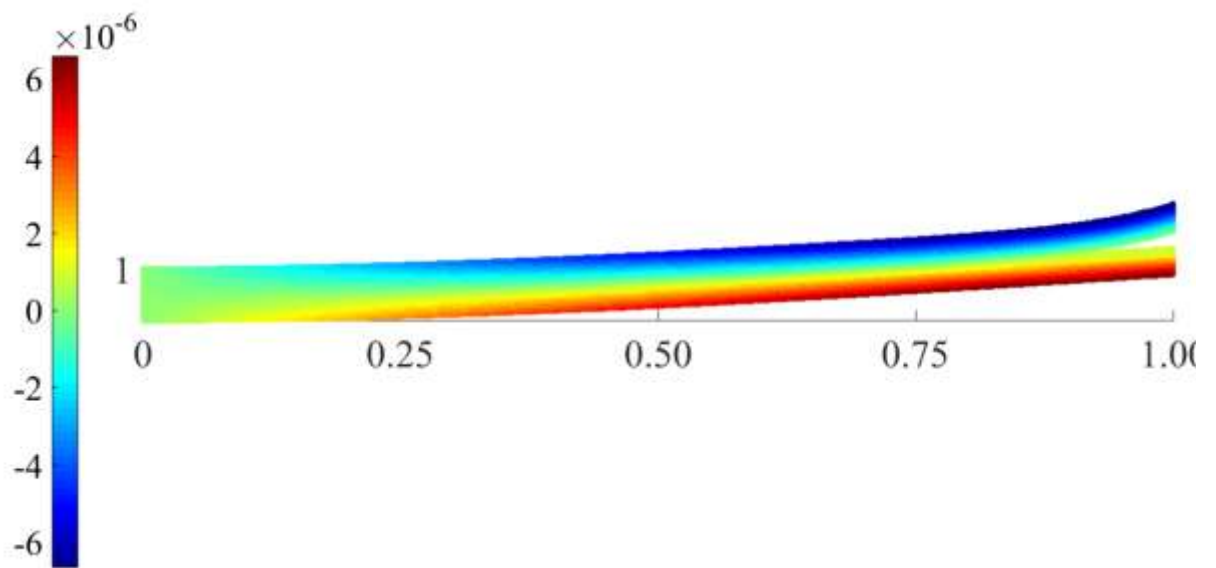
The deformed shape with the gradient of displacement on longitudinal and thickness directions are shown in Figure 66 and Figure 67 respectively. The stacking sequence considered in these figures is the $[0/90]_4$ laminate, but all others laminates show practically the same shape, with different magnitudes of displacement.

Figure 66 - Deformed shape with the gradient of displacement on longitudinal direction of $[0/90/0/90]_s$ laminate: a) bibliography; b) method proposed



Source: Li et al. (2015)

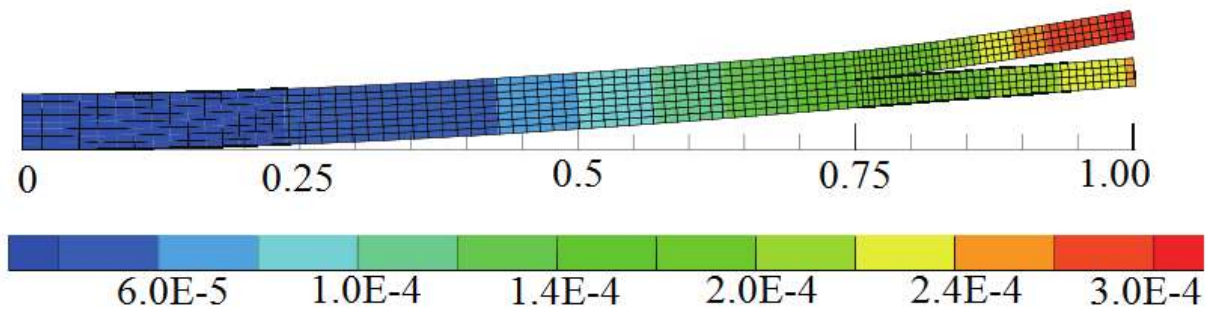
a)



b)

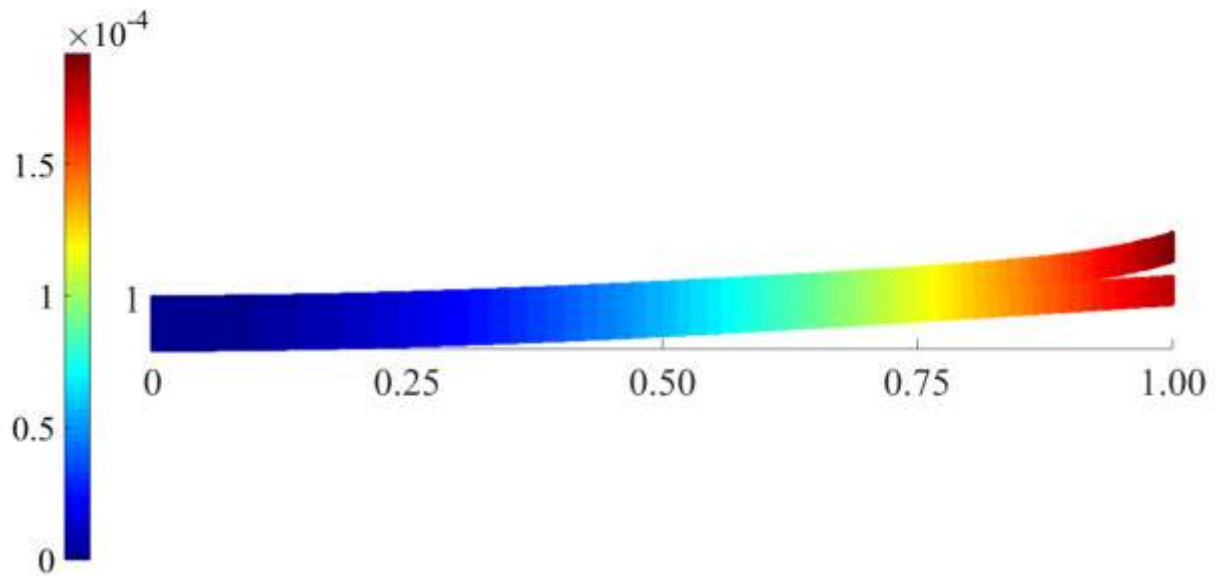
Source: Author.

Figure 67 - Deformed shape with the gradient of displacement on thickness direction of $[0/90/0/90]_s$ laminate: a) bibliography; b) method proposed



a)

Source: Li et al. (2015).



Source: Author.

b)

Table 7 - Crack tip displacements of bibliography and the proposed method of the second example

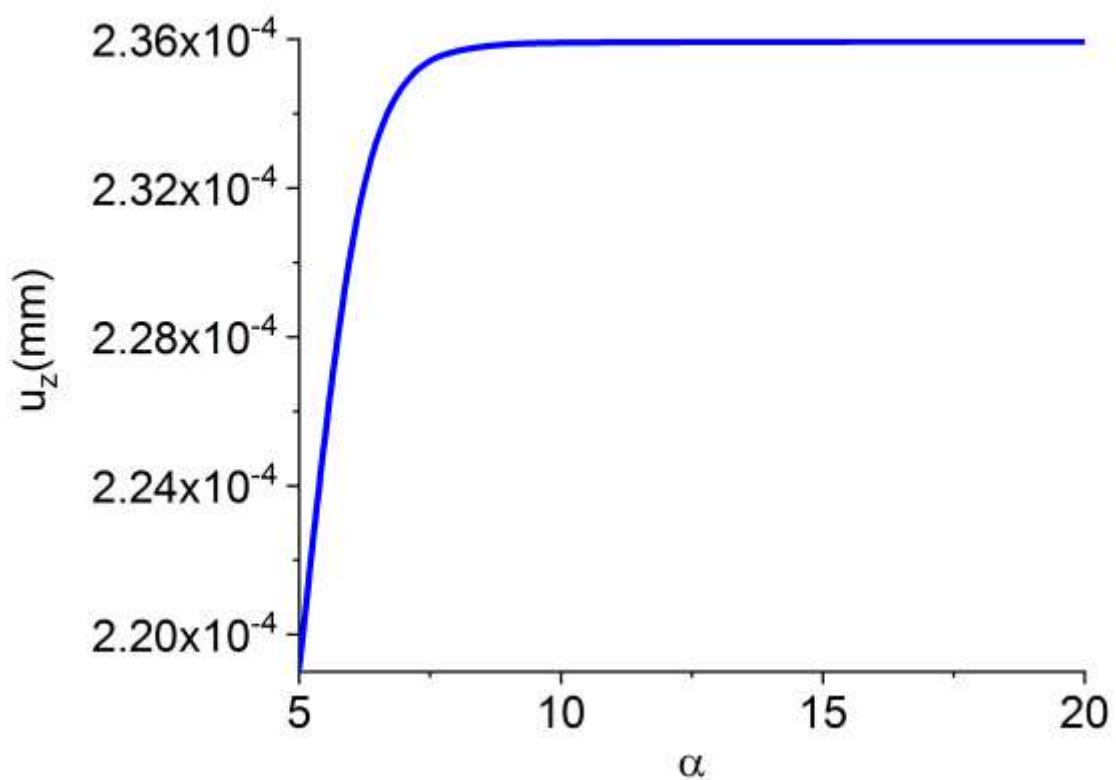
	$u_x(mm)$		$u_z(mm)$	
	Li et al. (2015) (x 10 ⁵)	XLFEM proposed (x 10 ⁵)	Li et al. (2015) (x 10 ⁴)	XLFEM proposed (x 10 ⁴)
[0] ₈	8.2855	0.66067	2.0831	1.9280
[0/90/0/90] _s	1.2272	0.93472	3.1674	3.1015
[90/0/90/0] _s	2.3130	1.8792	5.6199	5.5892

The results of the crack tip displacements in the thickness direction u_z , shown in Table 7, are close to those calculated by Li et al. (2015). Although, the displacement in longitudinal direction u_x is different in both methods. This fact is actually expected, because the formulation of Li et al. (2015) accounts the stress intensity factor at the crack tip via weak enrichments, which causes the stress field to be more severe at the crack tip, affecting the strain field and displacements in the longitudinal direction. Since fracture mechanics

phenomena are not accounted in the formulation developed here, it is expected that the displacement in longitudinal direction is reduced.

The numerical parameter α of the hyperbolic tangent function of equation (32) is further investigated. The influence of the α in the displacement field of the $[0]_8$ laminate is demonstrated in Figure 68. Observe that there is no significant variation of the solution for different values of α ; the magnitude of the displacement remains the same order. After reaching $\alpha = 10$, the solution barely varies. It is tested higher values of the numerical parameter, such as $\alpha = 1000$, but the results are roughly the same.

Figure 68 - Influence of the numerical parameter α in the displacement field



Source: Author.

6 CONCLUSIONS AND FUTURE WORKS

This masters thesis focuses in the development of a numerical model potentially capable to simulate delamination in composite structures by combining three powerful techniques: the XFEM to model the discontinuity; the Cohesive Zone Method to idealize the behaviour of the delaminated zone; and the layerwise theory. There are not numerous investigations concerning all these theories mentioned.

The primary objective of this master's thesis has been successfully achieved. The formulation developed here is potentially capable of simulating discontinuity in composite laminates. Four numerical examples are presented in this master's thesis: a four-layer thin composite plate laminate; a deep beam made of reinforced concrete; a three-layer composite sandwich with a geometry of a cube; and a eight-layer cantilevered beam with a zone pre-delaminated.

The first numerical example is a four-layered composite laminate with one end fixed and pressure applied to the upper surface. Two different stacking sequence are considered, $[0]_4$ and $[0/90]_2$. To validate this case, an analysis based in a solid-element with parabolic interpolation in all directions is carried out in ABAQUSTM. The results of the displacement and stress field converged. The outcome of the in-plane components of the stress tensor is almost the same in all analyses. Regarding the out-of-plane normal stress, the SOLID and LW analyses achieved same results. The out-of-plane shear stresses are the components that diverged the most. It is observed that the results of the $[0]_4$ plate are more accurate than the $[0/90]_2$, which is expected since more anisotropy results in more deviation of outcomes. An interesting conclusion regarding this first numerical example is the fact that enhancing the order of the polynomial approximation in thickness direction has not shown better results. This can be explained by the low ratio between thickness and in-plane dimensions, plus the constant pressure applied.

In the deep beam numerical example, both models carried out in ABAQUSTM presented similar results. The heterogeneous and homogenized analyses carried out in ABAQUSTM were close to each other. The layerwise analyses were precise; all three

layerwise analyses generated similar curves. The analyses whose cross-section are more refined shown better results, but the difference is small. In fact, there is no need to discretize too many layers using a linear interpolation. Close to the boundary conditions the layerwise and ABAQUSTM formulations slightly diverged. It is important to remark that the analysis performed in this example considered the reinforced concrete in its linear phase.

The third numerical problem is a three layered sandwich laminate with in plane dimensions equal to the thickness dimension. The layerwise analyses carried out are compared to a solid-like analysis done in ABAQUSTM, and it was concluded that enhancing the polynomial order of the interpolation through the thickness resulted in more accurate results, and the convergence of stresses have been faster. Therefore, it is recommended to increase the layerwise order for analyses of solid structures.

The fourth problem is an eight-layer cantilevered composite beam with a discontinuity simulating a pre-delaminated, typical to mode I fracture. Three different stacking sequences are considered in this problem: $[0]_8$, $[0/90]_4$ and $[90/0]_4$. Likewise the simulation carried out via XFEM by Li et al. (2015), the delamination in this problem does not grow. To approach this problem, the stiffness of the cohesive elements are pre-defined according to an arbitrary exponential function. The purpose of this analysis is to show the potential to approach delamination problems using the formulation proposed in this master's thesis. The deformed shape of the analysis done here and by Li et al. (2015) are similar. The displacement in thickness direction is the same; although, in the longitudinal direction the displacement diverges in each analysis. Since there is no crack tip enrichment to account fracture mechanics phenomena in the model developed here, the displacement in longitudinal direction is influenced only by Poisson's ratio. Hence, the state of stress near the crack tip influences the magnitude of the displacement in longitudinal direction, resulting in lower values than calculated by Li et al. (2015). Furthermore, the stress field is not compared to the bibliography for the same reason.

The main advantage of the numerical model developed in this master's thesis is the flexibility to model discontinuity. The layerwise displacement theory provides an accurate displacement and stress fields over the whole domain of the laminate, and the XFEM effectively models the delamination. It is observed that implementing strong enrichments in the absence of weak enrichments leads to an unrealistic outcome. Thus, the Cohesive Zone Method is proposed to model the constitutive relation of the delaminated zone. As a matter of

fact, using CZM instead of pure XFEM have both advantages and disadvantages. If weak enrichments are considered, the XFEM alone successfully simulates delamination in composite laminates, as it has been already proven by Li et al. (2015) and Li (2016). However, the computational cost rises considerably since more degrees of freedom are introduced.

Likewise all XFEM and CZM approaches available in literature, the formulation presented here relies in numerical parameters which are not simple to determine. As Pascoe et al. (2013) pointed out, the methods for modeling delamination in composite media so far are not based on the physics of the problem but on the observed shape of the delamination growth curve, whose parameters are defined by curve fitting. Therefore, it is recommended to investigate further the physical processes involved in delamination growth and the macroscopic behavior.

With respect to the work presented in this master's thesis further research is recommended in the following aspects:

- a) develop formulations that account physical processes interacted with progressive failure, and dispense purely numerical parameters;
- b) increment both weak and crack tip enrichments to the formulation developed here. Even though Li et al. (2015) and Li (2016) proposed similar formulation, it does not account progressive failure;
- c) implement in-plane strong enrichments to the formulation proposed;
- d) investigate further numerical integrations more adequate to non-linear displacement fields of XFEM's.

7 REFERENCES

Asadpoure A, Mohammadi S, Vafai A. Crack analysis in orthotropic media using the extended finite element method. *Thin Wall. Struct.* 2006; 44(9): 1031-1038.

Asadpoure A, Mohammadi S, Vafai A. Modeling crack in orthotropic media using a coupled finite element and partition of unity methods. *Finite Elem. Anal Des.* 2006; 42(13): 1165-1175.

Barbero EJ, Reddy JN. Modeling of delamination in composite laminates using a layer-wise plate theory. *Int. J. Solids Strut.* 1991; 28(3): 373-388.

Barenblatt G. The formation of equilibrium cracks during brittle fracture. General ideas and hypotheses. Axially-symmetric cracks. *J. Appl. Math. Mech.* 1959; 23(3): 622-636.

Barouni AK, Saravanos DA. A layerwise semi-analytical method for modeling guided wave propagation in laminated composite infinite plates with induced surface excitation. *Wave Motion.* 2017; 68: 56-77.

Bathe KJ. *Finite element procedures*. 1st ed. London, England: Prentice Hall, 1996.

Belytschko T, Black T. Elastic crack growth in finite elements with minimal remeshing. *Int. J. Numer. Meth. Eng.*, 1999; 45(5): 601-620.

Botello S, Oñate E, Canet JM. A layer-wise triangle for analysis of laminated composite plates and shells. *Comput. Struct.* 1999; 70(6): 635-646.

Brouzoulis J, Fagerström M. Modelling of multiple delaminations in shells using xfem. 19Th International Conference on Composite Materials; Jul 28 - Aug 2. Montreal, Canada. 2013: 1-9.

Camacho GT, Ortiz M. Computational modelling of impact damage in brittle materials. *Int. J. Solids. Struct.* 1996; 33(20-22): 2899-2938.

Camanho P, Davila CG, de Moura MF. Numerical simulation of mixed-mode progressive delamination in composite materials. *J. Compos. Mater.* 2003; 37(16): 1415-1438.

- Campilho RDSG, Banea MD, Neto JABP, Da Silva LFM. Modelling adhesive joints with cohesive zone models: Effect of the cohesive law shape of the adhesive layer. *Int. J. Adhes. Adhes.* 2013; 44: 48-56.
- Carloni C, Piva A, Viola E. An alternative complex variable formulation for an inclined crack in an orthotropic medium. *Eng. Fract. Mech.* 2003; 70(15): 2033-2058.
- Chen WF, Saleeb AF. *Constitutive equations for engineering materials: Volume 1: Elasticity and modeling.* 2nd ed. Amsterdam, Netherlands: Elsevier; 1994.
- Cho M, Parmerter RR. An efficient higher order plate theory for laminated composites. *Compos. Struct.* 1992; 20(2): 113-123.
- Daniel IM, Ishai O. *Engineering mechanics of composite materials.* 2nd ed. New York, NY. Oxford University Press; 1994.
- Demasi L. ∞^6 Mixed plate theories based on the generalized unified formulation: Part I: Governing equations. *Compos. Struct.* 2009a; 87(1): 1-11.
- Demasi L. ∞^6 Mixed plate theories based on the generalized unified formulation: Part II: Layerwise theories. *Compos. Struct.* 2009b; 87(2): 12-22.
- Dolbow J, Moës N, Belytschko T. An extended finite element method for modeling crack growth with frictional contact. *Comput. Meth. Appl. M.* 2001; 190(51-52): 6825-6846.
- Simulia DS Corp. *Abaqus 6.11 Theory manual.* ABAQUS, Inc. and Dassault Systèmes. 2011.
- Fries TP, Belytschko T.. The intrinsic xfem: a method for arbitrary discontinuities without additional unknowns. *Int. J. Numer. Meth. Eng.* 2006; 68(13): 1358-1385.
- Grogan DM, Brádaigh CMÓ, Leen SB. A combined xfem and cohesive zone model for composite laminate microcracking and permeability. *Compos. Struct.* 2015 ;120: 246-261.
- Herakovich CT. *Mechanics of fibrous composites.* 1st ed. New York, NY. John Wiley & Sons; 1998.
- Hutchinson JW, Evans AG. *Mechanics of materials: top-down approaches to fracture.* *Acta. Mater.* 2000; 48(1): 125-135.

Huynh DBP, Belytschko T. The extended finite element method for fracture in composite materials. *Int. J. Numer. Meth. Eng.* 2009; 77(2): 214-239.

Kam TY, Jan TB. First-ply failure analysis of laminated composite plates based on the layerwise linear displacement theory. *Compos. Struct.* 1996; 32(1): 583-591.

Kenane M, Benzeggagh ML. Mixed-mode delamination fracture toughness of unidirectional glass/epoxy composites under fatigue loading. *Compos. Sci. Technol.* 1997; 3538(97): 597-605.

Li DH, Liu Y. Extended layerwise method of laminated composite shells. *Compos. Struct.* 2015 Oct; 136: 313-344.

Li DH, Liu Y, Zhang X. An extended layerwise method for composite laminated beams with multiple delaminations and matrix cracks. *Int. J. Numer. Meth. Eng.* 2014 Oct; 101(6): 407-434.

Liu D, Li X. An overall view of laminate theories based on displacement. *J. Mater. Sci.* 1996 Oct; 30(14): 1539-1561.

Lo KH, Christensen RM, Wu EM. A high-order theory of plate deformation: Part 2: Laminated plates. *J. Appl. Mech.* 1977 Dec; 44(4): 669-676.

Megson THG. *Aircraft structures for engineering students*. 3rd ed. Burlington, MA. Butterworth Heinemann; 1999.

Melenk JM, Babuška I. The partition of unity finite element method: Basic theory and applications. Austin, TX. 1996 Jan; 96(1): 1-32.

Mindlin RD. Influence of rotatory inertia and shear on flexural motions of isotropic, elastic plates. *J. Appl. Mech.* 1951; 18: 31-38.

Moës N, Belytschko T. Extended finite element method for cohesive crack growth. *Eng. Fract. Mech.* 2002; 69(7): 813-833.

Moës N, Dolbow J, Belytschko T. A finite element method for crack growth without remeshing. *Int. J. Numer. Meth. Eng.* 1999; 46(1): 131-150.

Mohammadi S. Extended finite element method: For fracture analysis of structures. 1st ed. Oxford, England. Blackwell Publishing; 2008.

Mohammadi S, Asadpoure A. A novel approach to analyse a crack with the xfem in composite media. 2nd Asia-Pacific Int. J. Numer. Meth. Eng; 2006 Nov 14-16. Hefei, China.

Muñoz JJ, Galvanetto U, Robinson P. On the numerical simulation of fatigue driven delamination with interface elements. Int. J. Fatigue. 2006; 28(10 SPEC. ISS.): 1136-1146.

Needleman A. A continuum model for void nucleation by inclusion debonding. J. Appl. Mech. 1987; 54(3): 525-531.

Needleman A. An analysis of decohesion along an imperfect interface. Int. J. Fracture. 1990; 42(1): 21-40.

Nguyen O, Repetto EA, ORTIZ M, Radovitzky RA. A cohesive model of fatigue crack growth. INT J FRACTURE. 2001; 110: 351-369.

Oñate E. Structural Analysis with the finite element method - linear statics :Volume 2 beams, plates and shells. 1st ed. Barcelona, Spain. CIMNE; 2013.

Oñate E, Zienkiewicz OC, Suarez B, Taylor RL. A general methodology for deriving shear constrained reissner-mindlin plate elements. Int. J. Numer. Meth. Eng. 1992; 33(2): 345-367.

Pagano NJ. Exact solutions for composite laminates in cylindrical bending. J. Compos. Mater. 1969 Jul; 3(3): 398-411.

Pascoe JA, Alderliesten RC, Benedictus R. Methods for the prediction of fatigue delamination growth in composites and adhesive bonds - A critical review. Eng. Fract. Mech. 2013; 112-113: 72-96.

Pora J. Composite Materials in the Airbus A380. Blagnac, France. 2001.

Reddy JN. A generalization of two-dimensional theories of laminated composite plates. Commun. Appl Numer. M. 1987; 3(3): 173-180.

Reddy JN. On refined computational models of composite laminates. Int. J. Numer. Meth. Eng. 1989. 27(2); 361-382.

Reddy JN. *Mechanics of laminated composite plates and shells: Theory and analysis*. 2nd ed. Boca Raton, FL. CRC Press; 2004.

Remmers JJC, Wells GN, De Borst. A solid-like shell element allowing for arbitrary delaminations. *Int. J. Numer. Meth.* 2003; 58(13): 2013-2040.

Remmers JJC. *Discontinuities in Materials and Structures: A Unifying Computational Approach* [thesis]. Delft: Delft University of Technology, Faculty of Aerospace Engineering; 2006.

Remmers JJC, Wells GN, De Borst. A solid-like shell element allowing for arbitrary delaminations. *Int. J. Numer. Meth.* 2003; 58(13): 2013-2040.

Ribeiro ML, Tita V, Vandepitte D. A new damage model for composite laminates. *Compos. Struct.* 2012 Jan; 94(2): 635-642.

Robbins DH, Reddy JN. Modelling of thick composites using a layerwise laminate theory. *Int. J. Numer. Meth. Eng.* 1993; 36(4): 655-677.

Roe KL, Siegmund T. An irreversible cohesive zone model for interface fatigue crack growth simulation. *Eng. Fract. Mech.* 2003; 70(2): 209-232.

Shu X. An improved simple higher-order theory for laminated composite plates. *Comput. Struct.* 1994; 50(2): 231-236.

Tessler A, Di Sciuva M, Gherlone M. A refined zigzag beam theory for composite and sandwich beams. *J. Compos. Mater.* 2009; 43(9): 1051-1081.

Timoshenko SP. *Strength of materials: Part 1: Elementary theory and problems*. 2nd ed. New York, NY. D. Van Nostrand Co.; 1930.

Traversa AT. *Simulation of delamination in composites under quasi-static and fatigue loading using cohesive zone models* [thesis]. Girona: Universitat de Girona, Dept. D'Enginyeria Mecànica i de la Construcció Industrial; 2006.

Vilar MMS, Sartorato M, Santana HB, Leite MR. Finite elements numerical solution to deep beams based on layerwise displacement field. *J. Braz. Soc. Mech. Sci.* 2018;

Wells GN, Sluys LJ. A new method for modelling cohesive cracks using finite elements. *Int. J. Numer. Meth. Eng.* 2001; 50(12): 2667-2682.

Wu EM, Reuter RCJ. Crack extension in fiberglass reinforced plastics. Illinois. US Bureau of naval weapons. 1965, 275: 1-32.

Yang B, Mall S, Ravi-Chandar K. A cohesive zone model for fatigue crack growth in quasibrittle materials. *Int. J. Solids Struct.* 2001; 38(22-23): 3927-3944.

Zhang YX, Yang CH. Recent developments in finite element analysis for laminated composite plates. *Compos. Struct.* 2009 Feb; 88(1): 147-157.

Zhu TL. A reliability-based safety factor for aircraft composite structures. *Comput. Struct.* 1992; 48(4): 745-748.